EDEPENDENCE OF PHYSICAL AND MECHANICAL PROPERTIES ON POLYMER ARCHITECTURE FOR MODEL POLYMER NETWORKS

A Thesis
Presented to
The Academic Faculty

by

Ruilan Guo

In Partial Fulfillment
of the Requirements for the Degree
Doctor of Philosophy in the
School of Polymer, Textile and Fiber Engineering

Georgia Institute of Technology
April 2008

DEPENDENCE OF PHYSICAL AND MECHANICAL PROPERTIES ON POLYMER ARCHITECTURE FOR MODEL POLYMER NETWORKS

Approved by:

Dr. Karl I. Jacob, Advisor
School of Polymer, Textile & Fiber Engineering
Georgia Institute of Technology

Dr. Rina Tannenbaum
School of Materials Science & Engineering
Georgia Institute of Technology

Dr. Anselm C. Griffin
School of Polymer, Textile & Fiber Engineering
Georgia Institute of Technology

Dr. C. P. Wong
School of Materials Science & Engineering
Georgia Institute of Technology

Dr. Yonathan S. Thio
School of Polymer, Textile & Fiber Engineering
Georgia Institute of Technology

Dr. William J. Koros
School of Chemical & Biomolecular Engineering
Georgia Institute of Technology

Date Approved: January 23, 2008

To my parents, without whom none of this would have been even possible

&

To my sisters, who always believe in me

ACKNOWLEDGEMENTS

It is a pleasure to thank the many people who made this thesis possible.

I am deeply indebted to my advisor, Prof. Karl I. Jacob, for his constant guidance, support, allowance of freedom during the entire course of this work. I would like to thank him for his trust in my abilities and his continuous efforts to bring the best out of me. The improvements that he has brought in me over the years will help me for the rest of my career. His professional and personable attitude has guided me in a variety of ways and has made my stay at Georgia Institute of Technology a very rewarding and memorable experience.

I am grateful to Prof. Anselm Griffin, Prof. Rina Tannenbaum, Prof. William Koros, Prof. C. P. Wong, Prof. Yonathan Thio, for serving as my thesis reading committee and their part in guiding and supporting this work.

I am grateful to Dr. P. Thiyagarajan, Dr. David Bohnsack and Mr. Dennis Wozniak (IPNS, Argonne National Laboratory) for providing SANS facilities and help with the experiments and insightful discussions. Thanks also extend to Prof. David W. Gidley and his group at University of Michigan for Positron Annihilation Lifetime Spectroscopy (PALS) measurements.

I wish to thank my group members for their great help and cooperation and fellow graduate students for providing a stimulating and fun environment in which to learn and grow. Thanks also extend to all the staff and faculty of School of Polymer, Textile & Fiber Engineering for their assistance and help in many different ways.

Last, but most importantly, I wish to express my deepest appreciation to my family. I am eternally indebted to my parents, Chunhua Guo and Jinjin Zhang, for their wholehearted and endless support over the years. I would also like to thank my sisters for their understanding, patience and encouragement when it was most required. To them I dedicate this thesis.

CONTENTS

LIST OF TABLES

Page

LIST OF FIGURES

Page

LIST OF SYMBOLS AND ABBREVIATIONS

AIBN	azobisisobutyronitril
CROP	cationic ring-opening polymerization
DLS	dynamic light scattering
DP	degree of polymerization
DR	draw ratio
DSC	differential scanning calorimetry
FAB-MS	fast-atom bombardment mass spectroscopy
FPD	freezing point depression
FTIR	Fourier transform infra red
GPC	gel permeation chromatography
GTB	gel tensile blob
IGC	inverse gas chromatography
IRD	Infrared dichroism
MALDI-TOF	matrix-assisted laser desorption/ionization time of flight
MC	Monte Carlo
MD	molecular dynamics
NMR	nuclear magnetic resonance
o-Ps	ortho-positronium
PALS	positron annihilation lifetime spectroscopy
PDI	polydispersity index
PDMS	polydimethylsiloxane
PEO	polyethylene oxide
PPO	polyphenylene oxide

p-Ps	para-positronium
PS-DVB	polystyrene-divinylbenzene
PTFE	polytetrafluoroethylene
PTHF	polytetrahydrofuran
PTMP	pentaerythritol tetrakis (3-mercaptopropionate)
PTMSP	polytrimethylsilylpropyne
PVTMS	polyvinyltrimethylsilane
RIS	rotational isomeric state
SANS	small angle neutron scattering
SAXS	small angel X-ray scattering
SNOM	scanning near-field optical microscopy
TEMPO	2, 2, 6, 6-tetramethylpyperidine-1-oxyl
Tf_2O	trifluoromethanesulfonic anhydride
THF	tetrahydrofuran
WAXD	wide angle X-ray diffraction

SUMMARY

The primary purpose of this research is to establish the architecture-property relationship of polymer networks by studying the thermal and mechanical responses of a series of topologically different model PTHF networks. The research involves two main parts: preparation of various architectures and characterization of properties.

Three types of network architectures were considered in this work: 1) networks with same crosslink distribution characteristic (inhomogeneities) but different average crosslink density (M_c); 2) networks with equal M_c but different inhomogeneities; 3) networks with highly-crosslinked clusters of various sizes and size distribution. In the effort to prepare model PTHF networks with determinate topology, firstly telechelic PTHF precursors of narrow molecular weight distribution were synthesized through living cationic ring-opening polymerization and functional end-capping. The telechelic structure, M_n and M_n distribution of precursors were determined through FTIR, NMR, GPC, Raman, FAB MS, MALDI and chemical titration. In the second step, unimodal, bimodal and clustered PTHF networks were prepared by end-linking telechelic PTHF precursors and/or multifunctional clusters through thiol-ene reaction. The completion of thiol-ene end-linking reactions was confirmed by Raman and sol fraction measurements.

Thermal characteristics, i.e., glass transition temperature T_g, melting temperature T_m, heat of fusion, of model PTHF networks were investigated as function of crosslink density and inhomogeneities through DSC. Increasing the crosslink density increases T_g and lowers T_m and the enthalpy of fusion due to the crosslink junction confinement and the reduced flexibility of chain segments. However, the inhomogeneities have little effect on T_g. Meanwhile the inhomogeneities increase T_m due to more long segments incorporated in crosslinking and decrease the crystallinity probably due to more defects introduced by the very short chains and large clusters. Another interesting thermal

property involves the detection of freezing point depression (FPD) of small molecule solvent confined in model PTHF networks. The crosslinked elastomeric matrix, upon equilibrium swelling, is comparable to a 3-D network with the size of the meshes depending on the crosslink density. Higher the crosslink density gives smaller mesh size. As a result, the magnitude of FPD decreases with increasing the inter-crosslink segment length, reflecting large gel solvent crystals formed in large meshes. FPD also shows dependence on the inhomogeneous distribution in crosslink density given the same average intercrosslink chain length. The relationships between the pore size and FPD were obtained, providing a good reflection of the existing architecture facts in the networks.

Mechanical responses of model PTHF networks to uniaxial strains were studied through SANS at molecular level. The spatial inhomogeneities in crosslink distribution gave rise to the "*abnormal* butterfly patterns" on 2D isointensity contour plots, which became more pronounced as elongation ratio λ increases. Radii of gyration of inter-crosslink chains were calculated based on the scattering intensity profile at directions parallel and perpendicular to the stretching axis. The dependence of these quantities on λ was compared to the predictions of three rubber elasticity models: affine deformation model, phantom network model, and junction affine model. Experimental results could not be interpreted by any single theoretical model without taking into consideration junction fluctuations and the network topologies. While polymer chains in unimodal network deform phantomlike, deformation behaviors of long chains in bimodal and clustered networks have characteristics more like junction affine or affine deformation due to higher degree of inhomogeneities. Short chains in bimodal networks assume more deformation than long chains especially at high strains due to the limited extensibility. However, in clustered networks long chains assume large portion of deformation rather than the clusters which deform as a highly-crosslinked tough entity. There was negligible effect of cluster size observed on the elongation behavior of long chains.

Besides the extensive experimental efforts, MD simulations were carried out on linear model polymers subjected to thermal change and uniaxial stretching. The evolution of free volume size distribution was investigated using a domain-decomposition MD program coupled with hard sphere probe method and Voronoi tessellation method. The total free volume fraction increased slightly with an increase in temperature and a broader free volume size distribution was observed. In contrast, uniaxial stretching resulted in smaller mean size of free volume voids and narrower size distribution. Moreover, extra large and elliptical voids were formed at chain ends upon stretching. Under the combined effect of orientation and temperature, the size distribution of free volume cavities showed its dependence on the temperature at low strain levels, while this dependence diminishes with increasing strain and finally the free volume distribution becomes relatively independent of the temperature at high strain levels.

In summary, the research allows predictive design of polymer networks of precisely controlled architectures and highlights the importance of nanoscale architectures on macroscopic properties that could provide additional understanding of underlying polymer physics.

CHAPTER 1

INTRODUCTION

Study of architecture-property relationship has been attracting scientific interest throughout the development of materials science and engineering. Development of a fundamental knowledge of the interaction between the morphological architecture at various spatial and temporal scales that give rise to various polymer material properties provides a number of valuable tools to engineering materials with specific morphology and properties.

Modern synthetic chemical methods afford access to an unlimited number of architectural variations that begin with simple linear blocks and progress through a dizzying array of cyclic, graft, “comb”, “star” geometries, dentrimers and networks, etc. Great efforts have been put into understanding the impact of various architectures on the macroscopic properties of polymeric materials. For all polymer materials, heterogeneities or inhomogeneities are inherent structural species. Such heterogeneities are directly related to the packing nature of polymer materials, which in turn determines mechanical and physical properties of macromolecular systems. Things become more complicated when three-dimensional crosslinked networks are incorporated. Traditional crosslinking processes, like sulfur vulcanization, irradiation, peroxide thermolysis, are basically random processes. They can not provide any precise control over, or accurate knowledge of, the internal microscopic structure of the networks formed. The crosslinks in such networks are formed in an uncontrolled manner due to the existence of many dangling (pendant) chains, loops, trapped entanglements, etc. Consequently, the length of the

linear chain elements (elastic chains) fluctuates around its average value and it is not experimentally accessible. For this reason, it has been exceedingly difficult to obtain reliable structure-property relationship for elastomeric materials. For example, randomly crosslinked networks have been widely used to establish whether the theories of rubber elasticity and of equilibrium swelling are valid. But those theories are based on a number of structure hypotheses which are different from the topological structure of random crosslinking networks. Therefore, for the purpose of greater understanding of the physical principles involved in the crosslinking polymer as well as the verification of existing theories of rubber elasticity, the high level of research activity in this important area is directed at studies on "tailor-made" networks or "ideal" model networks. Such networks are prepared based on well-defined chemical reactions in which networks are formed in a controlled manner. The resultant networks would have the same average chain length and length distribution as the precursors from which they are prepared. An important example would be hydroxyl-terminated polydimethylsiloxane (PDMS) endlinked with tetrahoxysilane in a tin-catalyzed condensation reaction. Some others include polystyrene, polyurethane networks and polyacrylamide gels.

The effect of inhomogeneity in terms of chain length distribution between junctions has not been studied extensively. The distribution of intercrosslink molecular weight within an elastomer has been suspected to have probably greater effect on the elastomeric properties than M_c itself. Several studies have been carried out to study the mechanical properties of endlinking model polymer networks. It was found out that model networks frequently have unusually good ultimate properties compared with networks prepared using customary techniques like irradiation due to the fact that such

networks have very few dangling end irregularities and well-defined intercrosslink chain length distribution like bimodal distribution. Although some attempts have been taken on studying the elastomeric properties of model polymer networks, the relationship between inhomogeneities and properties has not been studied in a systematical way.

Firstly, independent physical techniques that can give direct characterization of inhomogeneities are not available. How the degree of inhomogeneity in networks is classified is not clear. Detailed knowledge about the dependence of some physical properties like glass transition, crystallization, melting behavior on the inhomogeneities is not accessible.

Secondly, it was shown recently that bimodal network has significantly higher reduced force than unimodal network given the similar average intercrosslink chain length. This is thought to be due to the limited extensibility of very short chains arising from the difference in the local orientation between short and long chains during deformation. However, few efforts have been conducted towards understanding the effects of inhomogeneities on the segmental orientation during the deformation processes. One method to study local orientation of chain molecule is to selectively label it with deuterium and then study it with small angle neutron scattering to obtain the unknown neutron scattering form factor.

Thirdly, following the second consideration, if such local orientation is significant, it may also cause the crystallization rate to be different for networks with different degree of inhomogeneity during the stress-induced crystallization. This is also an area where very limited information is available about the inhomogeneity effect on SIC. Therefore it

is of fundamental interest to follow the SIC behavior of model networks with various degrees of inhomogeneities using techniques like synchrotron XRD.

Fourthly, it is generally believed that high crosslinked density in rubbers results in high macrodensity, high stiffness and low penetrant absorption due to low free volume. However, several studies on epoxy networks showed the opposite observation, which was ascribed to the poor packing of the molecules in the highly crosslinked samples. Thus in many real cases, total free volume fraction alone is always insufficient to explain the important features of polymers. For example, specimens of the same density (same free volume faction) may exhibit very different properties depending on their prior thermal history. Moreover, reduction in the total volume (hence in free volume fraction) by physical aging and by application of pressure give rise to changes in the mechanical properties in the opposite sense – embrittlement in the former and enhance ductility in the latter case. All these illustrate that for polymers at given temperature and pressure, the knowledge of its total free volume does not guarantee the prediction of its future behavior. A possible solution is to invoke the overall total free volume along with the idea of the size distribution of free volume and its change with temperature and/or stress. Since no studies have been made on the free volume and free volume distribution in model polymer systems, it is worthwhile to undertake a comprehensive characterization of free volume and free volume distribution with the aim of obtaining a clearer understanding of the structure-property correlations in these model polymers.

Especially, “clustered” networks are new and unique network structures in this work, which introduce a new inhomogeneity level. Clusters are reactive, densely crosslinked short-chain networks similar to microgels. They are embedded in and

crosslinked with long chain polymer matrix to form the clustered networks. The descriptive information regarding the inhomogeneities, such as cluster size and size distribution are not available in literature. Moreover the studies on the physical and mechanical properties of clustered networks have not been reported yet.

Based on above considerations, the research is directed towards answering those questions and obtaining the fundamental understanding of the nano-scale architecture effects on macroscopic physical and mechanical properties of crosslinked polymeric materials through both experimental and computational approaches. To fulfill the objectives, the research work was decomposed into two main categories of specific tasks:

1. **Architecture design and synthesis:**

- Polytetrahydrofuran (PTHF) was chosen in this study due to following advantages: 1) telechelic PTHF precursors can be obtained by "living" polymerization, which gives narrow molecular weight distribution; 2) deuterium labeled THF is readily available; 3) PTHF is capable of undergoing stress-induced crystallization at room temperature, which is in a favorable range for these experiments.
- "Living" cationic ring-opening polymerization of THF and accurate characterization of telechelic structure and molecular weight: narrowly dispersed α, ω diallyl-PTHF within the molecular weight range, M_n = 600 – 1,000 (short chains) and M_n = 2,000 – 20,000 (middle and long chains). Deuterated PTHF precursors were also prepared in the same manner.
- Designed and synthesized model networks with various crosslink density and different inhomogeneity levels through thiol-ene endlinking process. By varying the fraction of short and middle or long chains, networks with well-defined but different degrees of

inhomogeneities in crosslink distribution were obtained, i.e., unimodal, bimodal and clustered networks. Selectively deuterium-labeled PTHF networks were also prepared in the same manner.

2. Properties characterization:

Physical and mechanical properties of model PTHF networks were characterized as functions of crosslink density (average intercrosslink molecular weight, M_c) and inhomogeneities in crosslink distribution. The property-architecture relationship was investigated on three batches of networks: networks with same inhomogeneity but different average crosslink density; networks with same mean crosslink density but different inhomogeneity in crosslink distribution; and networks with various cluster sizes and size distribution.

- Thermal characteristics (glass transition temperature, melting temperature, heat of fusion) were systematically investigated using DSC.
- Physical characterization of inhomogeneities in networks by investigating the abnormal freezing point depression of small molecule solvent confined in nano-scale meshes formed by intercrosslink chains in swollen networks.
- Studied the segmental orientation of chains in selectively labeled model networks under uniaxial stretching through small angle neutron scattering (SANS). Explored the molecular deformation mechanisms for these model networks.

As known, it is always very difficult and expensive to obtain information at atomic level through experimental approach. However, computational approach like molecular dynamics (MD) technique provides an alternative way to achieve this goal, in which the effect of external influence on the configuration and hence the microstructure

of a polymer can be studied, rather readily and perhaps with less ambiguity. As an important part, we applied MD simulations using the united atom model to quantitatively study the effect of temperature and molecular orientation on free volume distribution in linear model polymer system. We believe this information can help predict the properties such as gas transportation and dyeability.

The dissertation is accordingly organized in a manner to provide the reader with sufficient knowledge of the study presented. The following is a brief outline of the thesis.

- **Chapter 2** reviews and discusses the related work in the area of focus regarding model polymer networks and free volume distribution in polymeric materials.
- **Chapter 3** provides the details of the design, preparation and characterization of model PTHF networks. It includes the synthesis of telechelic PTHF precursors and thiol-ene endlinking processes for preparing networks.
- **Chapter 4** shows the detailed results of thermal characteristics of model PTHF networks. Glass transition temperature, melting point and heat of fusion are investigated as functions of crosslink density and inhomogeneities using DSC.
- **Chapter 5** deals with the abnormal phenomena of freezing point depression (FPD) of organic solvent confined in nanoscale network meshes. FPD and solvent crystal size are characterized as function of crosslink density and inhomogeneities in networks.
- **Chapter 6** is devoted to study the architectural effects on the molecular deformation behavior in model PTHF networks under uniaxial stretching through selective deuterium labeling and Small Angle Neutron Scattering (SANS).

- **Chapter 7** presents the molecular dynamics (MD) approach to follow the evolution of free volume and free volume size distribution of linear polymeric material subjected to external time-dependent changes, i.e., temperature and stretching.
- **Chapter 8** concludes the thesis. It summarizes the thesis, emphasizes the main results, and proposes further developments and recommendations based on present work.

CHAPTER 2

LITERATURE REVIEW

2.1. Model Polymer Networks Based on Endlinking

One of the most striking properties of flexible polymer chains is the rubber-like elasticity they exhibit when crosslinked into a network structure. The elasticity of the network is considered to originate from the entropy of the chains. The elastic free energy of an elastomer is usually considered as the sum of the contributions of individual chains. Thus, the most important parameter in predicting the network properties is the molecular weight between crosslinks, i.e. M_c. However, the effect of M_c and M_c distribution on rubber elasticity has not been studied very much. The difficulty comes from the fact that traditional crosslinking techniques like sulfur vulcanization, peroxide thermolysis, and radiation, are random and uncontrolled processes, which makes the network structure too complex to be elucidated. However, new synthetic approaches have been successfully designed to prepare "model" or "ideal" polymer networks with controllable structure and topology by endlinking process [1-4]. The resultant polymer network is a model network in which the chains between the crosslink sites have the same average length and distribution of lengths as the pre-polymer chains from which they are prepared.

2.1.1. Model Polymer Networks and General Approaches of Preparation

The preparation of model polymer networks usually involves two steps. In the first step, linear polymer precursors are prepared and end-capped with reactive end groups like vinyl or hydroxyl group. The α, ω -telechelic polymers are characterized

precisely in their molecular weight. In the second step, crosslinks are formed upon the addition of a multifunctional crosslinker. Instead of randomly joining chain segments, model polymer networks are formed by end-linking functionally terminated precursor chains with precisely controlled molecular weight using multifunctional end-linking agent. Thus molecular weight and molecular weight distribution between crosslinks are the same as those of the starting chains, and crosslinks have the functionality of the end-linking agent. Networks thus prepared are "ideal" and of known structure. In fact, there are variety of model networks can be prepared using new techniques to closely control the locations of crosslinks in a network structure. Typical topologies of model polymer networks are unimodal, bimodal and multimodal, which corresponds to mono-dispersed, dual-dispersed and multi-dispersed chain length distribution between crosslink sites, respectively. A schematic sketch of model polymer networks is shown in Figure 2-1.

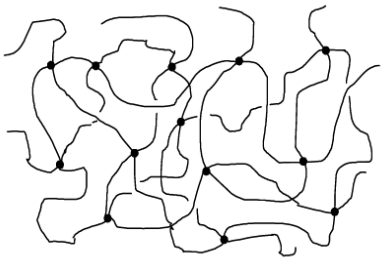

(a)

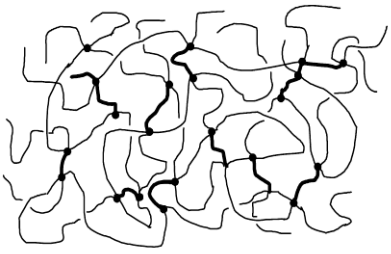

(b)

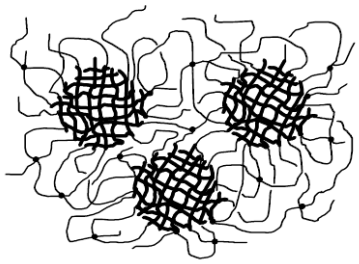

(c)

Figure 2-1 Sketch of typical model polymer networks: (a) unimodal, (b) bimodal and (c) clustered topology. Bold lines indicate short chains

Due to their known structures, model polymer networks are now the preferred materials for quantitative studies of rubber elasticity. Model polymer networks have been prepared from polydimethylsiloxane (PDMS), polyethylene oxide (PEO), polyurethane (PU), polytetrahydrofuran (PTHF), and PS-DVB. Herein model PDMS elastomer is the most popular in the studies of molecular theories of rubber elasticity [5, 6].

Synthesis of PDMS Model Networks

The high flexibility of PDMS chains [-$Si(CH_3)_2O$-] and their T_g (-113ºC) allow one to consider it as a liquid polymer at room temperatures. It is thus possible to study the elastic behavior of PDMS at room temperatures even in the absence of diluents. PDMS with controllable molecular weight and PDI are readily available with either hydroxyl or vinyl end groups. Generally the endlinking of PDMS involve hydroxyl-terminated chains by a condensation reaction, in which the hydroxyl groups are reacted with the alkoxy groups in a multifunctional organosilicate, such as tetraethlorthosilicate (TEOS), which are relatively free of complicating side reactions. This idea can be extended to various modalities (unimodal, bimodal, trimodal and multimodal etc.) by varying the ratio of short and long chains. The hydroxyl-alkoxy end-linking reaction for preparing model PDMS elastomer is shown in Figure 2-2.

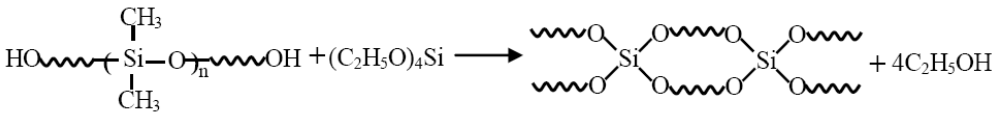

Figure 2-2 End-linking reaction of hydroxyl-terminated PDMS

PDMS model networks can also be prepared alternatively through the addition reaction between vinyl end groups of PDMS precursor and the active hydrogen atoms on silicon in an oligomeric poly (methylhydrogen siloxane) as shown in Figure 2-3 [7].

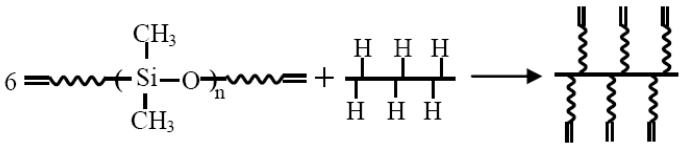

Figure 2-3 End-linking reaction of vinyl-terminated PDMS

However, PDMS networks are not suitable for studying the inhomogeneity effects on strain-induced crystallization due to their low crystallization temperatures (~ -40°C) [7]. Thus people turned to polymer networks with relatively higher melting point like PEO (T_m ~ 65°C) and PTHF (T_m ~ 40°C).

Synthesis of PEO Model Networks

PEO [-$(CH_2)_2$O-] is a better material for strain induced crystallization study since it has a higher melting point and crystallizes readily and it is available over a wide range in molecular weight [8]. PEO model networks have been synthesized by multiple couplings of the hydroxyl groups of the precursor with a trifunctional isocyanate. These endlinking processes are usually performed in the presence of an organic solvent to allow mobility of the chains and accessibility to the functional isocyanates to obtain high conversions. The concentration has been chosen high enough to decrease the probability of the formation of loops. Triisocyanates (-NCO), usually a commercial aliphatic

triisocyanate (Desmodur N75), has been used to end-link the hydroxyl terminated PEO precursors [8]. The endlinking reactions occur between -OH and -NCO groups of stoichiometric equivalence ([NCO]/[OH] = 1) and with dioxane as the organic solvent. To get a satisfactory reproducibility in the network formation process, the presence of trace amounts of water has to be removed since the isocyanates are very sensitive to protonic species. Thus the PEO samples have to be freeze-dried before use. The reactions proceed to near completion, and the resulting networks are elastomeric either at elevated temperatures or when swollen with a diluent [9]. Hydroxyl terminated PEO precursors are also able to react with aromatic triisocyanates, like Desmodur L [10]. The resultant networks are identical in many properties with those crosslinked from Desmodur N75. However, the networks prepared with aromatic Desmodur L exhibit a yellowish color, whereas those synthesized with aliphatic Desmodur N75 are colorless, especially when they are swollen to equilibrium in water.

Similarly, polyurethane networks (PU) based on PEO have been prepared by the end-linking of either hydroxyl-terminated linear chains with triisocyanates [11] or hydroxyl-terminated three-arm star polymers with diisocyanates [12, 13]. Crosslinking density is controlled by the molecular weight of precursor telechelic polymer as well as by molar ratios of -OH and -NCO groups, similarly to the study of epoxy networks.

Synthesis of PTHF Model Networks

Although the homopolymer PTHF [-$(CH_2)_4$O-] itself has limited commercial utility, networks prepared by crosslinking it could yield highly useful elastomer properties, like urethane [14]. PTHF precursors are prepared via a cationic ring opening mechanism, in which the propagating species is an oxonium ion that is ring-opened by

nucleophilic attack of the additional THF monomer. Since pure PTHF has no saturation and thus cannot be crosslinked using conventional sulfur-cure process, functional groups need to be attached at the living chain ends to facilitate end-linking reactions to form the model networks. Precursor PTHF could be either hydroxyl terminated or vinyl terminated depending on the types of end-capping reactions at living chain ends. In a typical case, telechelic PTHF polymers are synthesized by cationic ring opening polymerization (CROP) of THF with trifluoromethanesulfonic anhydride (Tf_2O) as initiator, followed by end-capping reactions endowing functional groups at chain ends [15]. For hydroxyl terminated PTHF system, tetrafunctional model networks were prepared by hydrolysis-condensation reaction with (3-isocyanatopropyl) triethoxysilane [$(C_2H_5O)_3Si(CH_2)_3NCO$] as end-capping agent using Sn-octoate (tin-2-ethyl hexanoate) as a catalyst. The crosslinking processes between –NCO groups and –OH groups were reported to be highly selective as followed by Infrared Spectroscopy [16]. For vinyl terminated PTHF system, there are two addition reactions possible to be used as crosslinking reactions. One is silane-vinyl addition reaction and another is thiol-ene addition reaction [15, 17]. Considering the possible rearrangement of allyl functional groups in silane-vinyl addition reaction, thiol-ene reaction is suitable for preparing the model PTHF networks with only an insignificant amount of side reactions. Thus diallyl-PTHF can be endlinked using pentaerythritol tetrakis(3-mercaptopropionate) (PTMP) as a crosslinking agent used to form a endlinked PTHF model networks and the reaction is initiated with a heat-activated free radical generator, like AIBN.

Synthesis of PS Model Networks

Besides elastomers like PDMS, PEO and PTHF, polystyrene - divinylbenzene (DVB) model networks have been prepared by "living" polymerization followed by the end-linking processes. The polystyrene precursors have been prepared by either living anionic polymerization [18] or living free radical polymerization [19-21]. The living anionic polymerization begins with an anion initiator and carbanions are the active site due to electrons transfer occurring to the double bond of the monomer. The bifunctional living PS is obtained by reaction of calculated proportions of monomer and bifunctional initiators such as di-sodium-a-methyl styrene tetramer or sodium-naphtylide. Methods of controlling the free radical polymerization of styrene are based on some reversible reactions between the growing polymer radicals and "control" agents, leading to an exchange between "active" and "dormant" species. As a result, controlled reactions lead to the formation of well-defined α, ω-difunctional polystyrene precursors. Then model PS network is formed in which each precursor polymer chain is connected to two different poly(DVB) nodules; they thus become the elastically effective network chains. However, PS networks synthesized by the sequential anionic polymerization of styrene and DVB cannot be considered strictly as ideal networks due to the reasons that: 1) considerable amount of dangling or pendent chains and loops are not evitable; 2) the average functionality of the branch points remains unknown. Nevertheless, these PS model networks have been successfully used to test the equilibrium swelling theories.

2.1.2. Inhomogeneities (or heterogeneities) in Polymer Networks

Inhomogeneities are inherently present in polymer networks and gels which arise from either the crosslinking processes or phase behaviors during network fabrication.

Inhomogeneities are non-uniform spatial distributions of crosslink sites in networks, which is non-relaxing frozen concentration fluctuation. An obvious consequence of inhomogeneities in crosslinks is that upon stretching the local strain is not uniformly distributed, resulting in mechanical properties deviated from theoretical predictions. Inhomogeneities in polymer networks have been widely studied through a number of modern scattering techniques like light scattering (LS), small angle X-ray scattering (SAXS), small angle neutron scattering (SANS), proton low-field NMR spectroscopy, and near field optical spectroscopy. All the studies clearly indicate that polymer networks and gels have a certain long-range spatial heterogeneity which does not exist in polymer solutions of the same polymer concentration.

Physical Characterization

The very first work in the investigation of inhomogeneities in polymer networks and gels can be attributed to Stein [22] and Bueche [23] using static light scattering (SLS). An important finding regarding inhomogeneities of polymer networks is the excess scattering of light. In comparison to the scattering results for the solutions of linear chains of equal polymer concentration, the swollen networks scattered more light, which indicated that inhomogeneities were introduced from crosslinking processes. Therefore Stein [24] proposed that the total scattered intensity from a swollen network (in terms of Rayleigh factor, R_t) was contributed from three parts: density fluctuation, R_d, concentration fluctuations, R_c, and excess scattering, R_e, arising from inhomogeneities:

$$R_t = R_d + R_c + R_e$$

The density fluctuation term can be estimated from the refractive index and the bulk compressibility while the concentration fluctuations can be calculated for an ideal

network using a Flory-Rehner type equation for its equilibrium swelling. The excess scattering due to inhomogeneities may be detected from resulting refractive index fluctuations in the swollen state and was derived as:

$$R = k_n \frac{9}{25} \frac{(n_1 - n_2)^2 \phi_2^2 < (\Delta M_c)^2 >}{\overline{M_c^2}} \int_0^\infty j(r)(\sin hr / hr) r^2 dr$$

where $k_n = 16\pi^3 n^2 / \lambda_0^4$

λ_0– the wavelength of light in vacuum

n – the refractive index of dilute (1) and polymer (2)

$h = 4\pi \sin(\theta/2) / \lambda_0$

$j(r) = (< (\Delta M_c)_i (\Delta M_c)_j >) / < (\Delta M_c)^2 >$

r – the distance between a pair of volume elements i and j

As shown above, from excess scattering detection, $<(\Delta M_c)^2>$, the mean-squared fluctuation in inter-crosslink molecular weight could be estimated. Quantitative SLS measurements were performed on bimodal PDMS networks swollen in toluene and benzene [25]. Scattering measurements were performed on series of bimodal PDMS networks with varying ratio of short chains (M_n = 770) and long ones (M_n = 22,500). The bimodal network of 50 mol% short chains showed the largest excess scattering and the unimodal network of pure short chains had the least excess scattering, while the excess scattering of other bimodal networks were in between. In addition, unimodal network of long chains had larger excess scattering compared with the one of short chains, which suggested that entanglements in the long chain unimodal networks might contribute to the excess scattering since long chains entangle more severely than short ones.

Dynamic light scattering (DLS) techniques were also employed to investigate the inhomogeneities in bimodal PDMS networks by Oikawa [26]. The cooperative diffusion coefficient D_{coop} and the normalized variance were determined. It was found that D_{coop} was proportional to polymer weight concentration to the power of 0.88, which was larger than the theoretical exponent compared with the unimodal networks suggesting a spatially and compositionally heterogeneous structure of bimodal PDMS networks.

Small angle X-ray scattering (SAXS) method has also been used to investigate the inhomogeneities in polymer networks. Unlike light scattering, in which refractive index fluctuation results in the excess scattering, in SAXS, the fluctuation of electron density would give the information of inhomogeneities [8, 27]. In the study of model PDMS networks using SAXS, Urayama et al [27] found that for unimodal networks the scattering profiles were primarily depended on the extent of how much the PDMS chains were entangled in the uncrosslinked state. For bimodal networks, the correlation lengths did not strongly depend on the composition of short chains, and were close to the one for short-chain unimodal networks. The correlation length for the unimodal networks of long chains was larger than the unimodal networks of short chains and it was considerably reduced by adding short chains. Thus they proposed that the elementary meshes in the networks of long chains were governed by trapped entanglements. In the study of bimodal epoxies [28], a pronounced scattering maximum was observed and it could be interpreted in terms of correlation holes. Bimodal networks exhibited scattering maxima at significantly lower scattering vector than any single amine networks. This shift in peak position indicates the existences of longer correlation distances in bimodal networks.

Investigations on the conformation and inhomogeneities of model network and gels have been performed using small-angle neutron scattering (SANS). Wu et al [17] found that the mixture of the uncured long and short PDMS chains approached that of an ideal solution, while a dramatic increase in intensity occurred in the small q (scattering vector) region as cure proceeded due to excess scattering. It suggested that segregation occurred during crosslinking resulting in the heterogeneities in networks. Shibayama et al [29] did SANS study on series of unimodal PTHF networks. The results showed that unimodal network of longest chain length had the largest excess scattering indicating that unimodal networks with longer inter-crosslink chain length were more heterogeneous than the ones having shorter chain length. The scattering patterns of model gels as a function of the swelling ratio and stretching ratio was investigated by Bastide et al [30, 31]. The gel signals were compared to those of solutions of linear chains of the same concentration. It was shown that in both swollen and stretching state, the signals for gels were much stronger than the equivalent solutions of linear chains at small angles, which was attributed to the heterogeneities in the gels. More importantly, an unusual scattering pattern, so called "butterfly pattern", was observed. It was characterized by an increase of intensity in the direction parallel to the stretching and to iso-intensity curves. It was suggested that the structure of gels was a three-dimensional net built up from "basic objects" (like star molecules) with a rather large size distribution. These objects were heterogeneously distributed in space resulting in strong excess scattering at small angles. Beltzung et al [32, 33] did SANS on PDMS melts, solutions, and dry and swollen PDMS networks. The results showed that the chain dimensions were not changed by the cross-linking process. The radius of gyration of an elastic chain in the unswollen network and

that of the corresponding "free" chain in the melt are identical and the Gaussian character of the network chains has been confirmed.

Recently, Saalwachter [34, 35] introduced a strategy based on proton multiple-quantum (MQ) NMR spectroscopy to study the swelling heterogeneities in model PDMS networks. The MQ NMR method is sensitive to chain order parameter distributions and therefore heterogeneities in the extent of fast motional averaging of individual network strands subject to topological constraints can be probed. It was found that the chain order parameter distribution became broader upon swelling accompanied by a nonaffine change of this distribution, indicating a heterogeneous swelling process related to the motions on length scales larger than the averaged strand length. And it was stated that topologically frozen inhomogeneities should be present already in the dry state and became visible upon swelling. However, as to the spatial extension of the observed inhomogeneities, the diffusion results did not yield conclusive information on their length scale.

Although the inhomogeneities of the polymer networks have been mainly studied by various scattering techniques, few direct real-space observations have been reported. A newly developed technique, scanning near-field optical microscopy (SNOM), was employed by Yamamoto et al [36] to investigate the structural inhomogeneity of the PMMA networks. Unlike conventional optical microscopy, SNOM can provide optical images and spectroscopic information in a local area with a spatial resolution of several tens of nanometers. In their study, the optically transparent PMMA networks were labeled with fluorescent dyes and the spatial distribution of the chain segments and cross-links were directly visualized in real space. PMMA network was found to have an inhomogeneous structure in a scale of submicrons. The fluorescence decay through the

near-field excitation showed that the local segment density was ten times higher than the ensemble average density of the network. The local segment density had little correlation with the structure in a submicron scale observed by SNOM. Based on these findings they proposed that the PMMA network has a hierarchical structure.

Theoretical Characterization

Besides extensive experimental studies, theoretical investigations have also been carried out to explore the inhomogeneities in polymer networks. A basic attempt to study the inhomogeneities in swollen networks theoretically is due to Bastide et al [31, 37], who analogized the crosslinking process with a percolation phenomenon, suggesting that the crosslinking process imposed “frozen blobs” of crosslinked material. The network mixture was a random distribution of crosslinks on a lattice formed by the inter-chain contact points in the solution. When two junctions are located on neighboring lattice sites, a “frozen blob” is formed. These more crosslinked clusters are supposed to be less deformed than less crosslinked regions when swelling. The so-called SANS "butterfly patterns" were also predicted and an expression for the scattering was derived essentially as a Lorentzian modified by a crossover function, which were proved in their later SANS experiments [31]. Sukumaran et al [38] fitted the neutron scattering behavior of equilibrium-swollen PDMS networks with Gel Tensile Blob (GTB) model using the unified function. The schematic of the extended tensile structure following the GTB model (top) and the predicted scattering pattern (bottom) exhibiting several power law scattering regimes are shown in Figure 2-4.

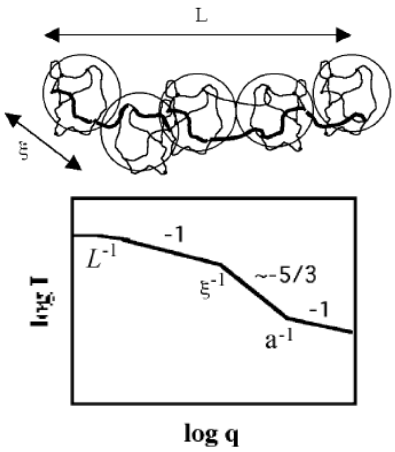

Figure 2-4 Schematic of the extended tensile structure following GTB model (top) and predicted scattering pattern (bottom), where ξ is the tensile-blob size, L is the extended length, and a is the persistence length.

As shown, equilibrium-swollen networks consistently displayed a linear scattering regime at low wave vector, q, followed by a good-solvent-like scaling regime at high q in agreement with the predictions of the GTB model. Swollen networks displayed a base structural size, the GTB size, ξ, that was found to be independent of the molecular weight between crosslinks, consistent with the predictions of the model.

Vilgis [39] studied the effects of inhomogeneities on rubber elasticity through statistical mechanics approach. It was assumed that there was a fluctuation of crosslink density $n(r)$ for the mean value of the crosslink number $N_c^{\,0}$, and $n(r)$ was a Gaussian variable. Based on the assumptions the average free energy was derived as:

$$F = \frac{1}{2} N_c^0 kT \left(\sum_i \lambda_i^2 - \log\left\{ \frac{6N_c^0}{lL} \right\} + 1 + \frac{3}{2} \frac{\Delta}{N_c^0} \right)$$

where λ_i – the Cartesian stretching ratio

l – the length of the Kuhn segment

L – the local contour length of the network chains

Δ – the measurement of the strength of the network disorder

The expression showed that there was only marginal change in the free energy with considering the fluctuation of crosslinks and also the modulus and the deformation dependence of the free energy were not altered. This observation suggested that the macroscopic quantity, free energy, was not sensitive to the microscopic details like weak inhomogeneities. It was however predicted that the inhomogeneities should show strong effect on the neutron scattering form factor $S(k)$. A correction in the exponent of $S(k)$ was found and the fluctuation of the cross-link density introduced a new wave vector and new deformation dependence. However it was not proved by the experimental data.

Sommer et al [40] employed the large scale Monte Carlo simulations using the bond-fluctuation model to predict the topological structure and swelling of bimodal polymer networks. The formation of clusters of short chains was observed during the end-linking process, which was considered to be due to the induced composition instability. The internal network structures were also followed during isotropic and athermal swelling. The results showed that the deformation of individual strands was much lower than the external deformation when it was close to swelling equilibrium. Even the long chains displayed subaffine behavior. The profound subaffine deformation was found to be in the range of several 10,000 monomers. Only if the substructures reached a size of much more than 100,000 monomers was affine behavior recovered.

2.1.3. Segmental Orientation in Uniaxial Stretched Model Polymer Networks

Many of the properties of polymers are directly related to their morphology and topology. One important aspect of morphology is the orientation of the molecules during deformation. Orientation is desirable in order to maximize polymers in desired directions. However, polymer deformation differs at various levels of morphology. Various parts of

molecules or different molecules in a blend may orient differently. A non-isotropic orientation distribution often leads to a pronounced anisotropy of the macroscopic mechanical properties. Segmental orientation of polymer chains can be studied by the various techniques such as birefringence, IR dichroism (IRD), Raman polarization, X-ray (SAXS & WAXD) and small angle neutron scattering (SANS).

The segmental orientation can be followed using IRD as long as the bands associated with different parts of molecules can be distinctly differentiated. For orientated samples, the spectra differ depending on the direction of the plane of polarization relative to the molecular orientation. This effect is conveniently expressed by the dichoric ratio, $D = A_{\parallel}/A_{\perp}$, which is used to determine the average orientation of the polymer chains, P_2:

$$P_2 = \frac{3 < \cos^2 \theta > -1}{2} = \frac{D-1}{D+2} \cdot \frac{D_0 + 2}{D_0 - 1}$$

where θ is the angle between the chain axis and the stretching direction and $D_0 = 2cot^2\alpha$ is the intrinsic dichoric ratio with α representing the angle between the transition moment vector and the chain axis. Stein et al [41] studied the segmental orientation in bimodal PTHF networks using IRD method. It was found that P_2 became greater with decreasing inter-crosslink molecular weight for the unimodal networks, in consistent with the prediction of Kuhn and Grün's rubber elasticity theory. As for the bimodal networks, P_2 for the long chain species was almost equal to the P_2 for the short chains, suggesting a non-affine deformation of chain segments at molecular level. However, Erman et al [2, 42] found that Kuhn expression considerably overestimated the segmental orientation in unimodal PDMS networks. While for the bimodal ones, short ones oriented less than the corresponding chains in the unimodal ones. The orientations of the short and long chains in bimodal networks were approximately equal to each other.

A major category of techniques in characterizing segmental orientation is the scattering techniques, like light scattering, X-ray scattering and diffraction and neutron scattering. The principles of scattering by light, X-rays, and neutrons are the same, being related to the interactions of radiation with matter. The scattering by light, X-rays, and neutrons depends, respectively, on the differences in the refractive index (or dielectric constant), the electron density, and the scattering length. The orientation of morphology entities of larger size, such as spherulites, is usually studied using LS. To study the mesoscale and nanoscale structural changes during deformation, synchrotron SAXS and WAXD are definitely one of the most powerful characterization techniques. SANS is a powerful tool to investigate the conformation of specific macromolecular chains. These techniques have been proved to be effective in characterizing the chain orientations and are complimentary to each other. However segmental orientations in polymer networks are quite limited from scattering techniques, especially for model polymer networks.

Structural developments in natural rubbers [43] and synthetic rubbers [44] during uniaxial deformation were revealed by synchrotron X-ray diffraction. In vulcanized natural rubber samples, higher crosslinking density resulted in smaller orientational fluctuations of crystallites and the lattice constants of the natural rubber crystal changed almost linearly with nominal stress. For synthetic rubbers, the majority of the molecules (50-75% in mass) remained in the unoriented amorphous state even at large strains due to the heterogeneity of network topology. The heterogeneity also led to a microfibrillar crystalline structure between the nearby vulcanization points at high strains, which in turn are responsible for the mechanical properties of rubber at large deformation.

SANS is a powerful technique to characterize the deformation of elastic chains that results from a macroscopic deformation of the system. Deuteration of polymer chains allows a visualization of the deuterated polymer in an undeuterated matrix. During deformation, the chain radii of gyration become anisotropic as may be followed by neutron scattering. The microscopic deformation of elastic chains in polymer networks is provided through analysis of the structure factor, $S(q)$, of a single chain under strain, which is a perfect descriptor to discriminate between current theories of rubber elasticity. Study of uniaxially stretched PDMS networks using SANS was reported by Beltzung et al [32]. A range of behavior was observed at the level of the elastic chain, but in no case was the deformation of the elementary network chains affine with the macroscopic deformation. The experimental results were compared with those expected on the basis of the classical theories of rubber elasticity, and cannot be interpreted within the framework of a unique model. An interpretation of the chain behavior, taking into account a rearrangement of cross-link positions upon deformation, was thus proposed. Menge et al [45] studied the uniaxially stretched butadiene rubbers by SANS as well as mechanical measurements. The effect of topological constraints on the microscopic deformation of the butadiene network chains could be well described within a tube model and proposed nonaffine deformation dependence gave a good description of the statistical mechanics of rubber elastic networks even at large deformation and for polydispersed networks.

2.2. Free Volume and Free Volume Distribution in Polymers

Polymer free volume has been investigated widely due to its importance in understanding and predicting the macroscopic properties of various materials. Although the exact concept of free volume is under debate, it has long been used to relate

mechanical and rheological properties, such as viscosity [46, 47], as well as to explain and interpret many phenomena such as glass transition [48-50], physical aging [51, 52] and transport behavior in polymeric systems[53, 54]. At early stage, free volume was merely regarded as a theoretical concept that could explain many aspects of polymer behavior but could not be determined directly. A stride in quantitative application of the free volume approach has been made thanks to an appearance of physical methods for estimation of mean free volume size and size distribution in polymers. To date, various physical techniques, as well as quantitative molecular models, have been developed and proposed in evaluating polymer free volume and its distribution, which have shown great success in predicting polymer behavior. It is therefore the objective of this section to review useful definitions and theories of free volume and free volume distribution in polymers and to explore in particular how far the concept of free volume and free volume distribution can be related to the applications currently being developed in polymeric materials.

Free volume in polymer is a measure of the internal unoccupied space available in a system for the movement of the polymer chain or other penetrant molecules, which imparts flexibility to the polymer. However, the exact concept of free volume is not uniformly defined.

2.2.1. Definitions of Free Volume

The development of free volume concept can be traced back to 1930s, as first introduced by Kincaid and Eyring [55] for liquids of small molecules. It was stated that molecular motion in the bulk state depends on the presence of holes, or places where there are vacancies or voids. Although only small molecules were considered in their

research, a similar model can be constructed for the motion of polyatomic chains, the main difference being that more than one "hole" was required in the same location as cooperative motions are required. These holes, collectively, are called "free volume", which is envisaged as the excess space, unoccupied by molecules, and is dynamically shared by the molecules in their thermal motion. It is usually defined as the difference between the total volume and the "occupied" or "core" volume of the molecules. The latter is often defined differently by different workers, which renders the confusions in defining free volume. A notable contribution concerning the classification of various free volume definitions was ascribed to Bondi [56], in which three types of definitions referred to free volume were suggested as summarized below.

1. Empty volume:

$$V_{emp} = V_T - V_{vdw} \qquad \text{Eq. 1}$$

where V_T is the macroscopic volume at temperature T and V_{vdw} is the van der Waals volume that occupied by the molecule, which is impenetrable for other molecules with thermal energies at ordinary temperatures. With the knowledge of bond lengths, bond angles, contact distances (i.e., intermolecular van der Waals radii, r_w), and shape characteristics of atoms, V_{vdw} can be calculated from these van der Waals dimensions obtained by X-ray diffraction or from gas kinetic collision cross sections. Thus according to this definition, free volume is the difference between the measured total volume and the occupied volume, regardless of small molecules or polymers.

2. Expansion volume:

$$V_{exp} = V_T - V_o \qquad \text{Eq. 2}$$

where V_T is the macroscopic volume at temperature T and V_o is the volume of the molecules at 0 ºK in a closely packed crystalline state. Expansion volume must always be smaller than the empty volume in polymers since thermal motions of polyatomic molecules can not occupy or sweep all the empty space due to conformational restrictions. This definition was also accepted by Doolittle [48] to be that "free space" arises from the total thermal expansion of the liquid without change of phase. Small differences may be found if the V_o is defined or assumed differently.

3. Fluctuation volume:

$$V_{flu} = N_A V_q \qquad \text{Eq. 3}$$

where V_q is the volume swept out by the center of gravity of the molecules as a result of thermal vibration and N_A is Avogadro constant. By assuming that all of the empty volume is accessible to the thermal motions of the molecules in the liquid state, i.e., free path is small compared with the molecular diameter, Bondi showed that fluctuation volume, V_{flu}, could be related to the empty volume V_{emp} and occupied volume V_{vdw} as

$$V_{flu} = \frac{4}{3}\left(\frac{V_{emp}}{A}\right)^3 \times N_A = \frac{V_{emp}^3}{27V_{vdw}^2} \qquad \text{Eq. 4}$$

where A is the area per mole of molecules calculated from the known bond lengths and van der Waals radii. According to this classification, free volume concept used by Kincaid and Eyring is actually the fluctuation volume, which denoted the total integral of the volume swept out by the center of gravity of the molecule from its equilibrium position as a result of thermal motion. Fluctuation volume can be obtained from sound velocity measurements.

From the definitions above, one could tell that in a specific system, the values of total free volume should descend in an order of empty volume > expansion volume >

fluctuation volume. In fact, due to the different ways of definition, values of free volume may vary by an order of magnitude. So it should be very carefully and clearly indicated that which kind of definition is used when free volume concept is employed in any research. Table 2-1 (after Bondi [56]) shows the comparison of three types of free volume fraction calculated using different definitions for several polymers.

Table 2-1 Free volume fraction at T_g for some polymers

Polymer	**free volume fraction** *		
	f_{emp}	f_{exp}	f_{flu}
Polystyrene	0.375	0.127	0.0035
Poly(vinyl acetate)	0.348	0.14	0.0023
Poly(methyl methacrylate)	0.335	0.13	0.0015
Poly(n-butyl methacrylate)	0.335	0.13	0.0010
Polyisobutylene	0.320	0.125	0.0017

* free volume fraction, f = calculated free volume / total volume

Despite of various definitions of free volume, it should be noted that there is only one type of empty space between molecules. Differences arise only when theories are developed which are concerned with the way this free space enters into molecular processes. From this point of view the same basic geometry may be treated in very different ways to accommodate the need to interpret a particular phenomenon.

2.2.2. Experimental Characterization of Polymer Free Volume

At very first stage of study only total free volume fraction can be determined from techniques like density measurement; however, it is soon realized that it is not enough to well understand the properties by total free volume alone. For example, specimens of the

same density (i.e., the same free volume faction) may exhibit very different properties depending on prior thermal history. Moreover, reduction in the total volume (hence in free volume fraction) by physical aging and by applying pressure give rise to changes in the mechanical properties in the opposite way - embrittlement in the former and enhance ductility in the latter case. All these illustrate that the knowledge of total free volume alone does not guarantee the prediction of its future behavior. Therefore techniques that enable the evaluation of both the total free volume and the distribution of free volume are desirable. In this section some characterization techniques are summarized and results concerning the advantages and limitations of these techniques are emphasized.

Density Measurement

Density measurement intrinsically gives the expansion volume according to the definition, $V_{exp} = V_T - V_o$. The expansion volume can be defined unambiguously if a definite value of the volume at 0 ºK, V_o, can be postulated. This closest packing volume V_o can be readily estimated for small molecules from density data by extrapolating from density data at higher temperatures to 0 ºK. However V_o for polymers is more difficult to be determined due to the reason that polymers become glasses at low temperature, which make extrapolation to 0 ºK unobtainable. The first attempt of applying this method to polymer-like system is ascribed to Doolittle [46-48] using dilatometry. As shown, the densities at 0 ºK of the family of *n*-paraffin hydrocarbons could be reasonably extrapolated from the specific volumes measured, which permitted the calculation of reliable values of free space from density data. Although *n*-paraffins are not real polymers and there is no certainty that they could be applied to polymers, the comparison with the limited results obtained directly with polymers suggests that they might give

reasonable results [57]. Bondi [58] applied the method to polymers by assuming that V_o is the same as that of the crystal at 0 ºK. He employed the available data on crystal densities together with their coefficients of expansion to provide extrapolated value of V_o. However, the values of the expansion volume obtained in this way did not agree with the free volumes derived from viscosity data by the well known WLF treatment which can generally lead to a fractional free volume at T_g of about 0.025, while it is around 0.13 according to Bondi's extrapolation.

Later an alternative approach [59] was developed based on the suggestion that V_o is given by the condition at which the internal pressure falls to zero, i.e., when

$$T\alpha / \beta - P_{(\text{external pressure})} = 0$$

where α and β are the coefficients of thermal expansion and isothermal compressibility. Some systematic pressure-volume-temperature data have been obtained for atactic polystyrene. The internal pressure was plotted as a function of the specific volume and it was seen that the isotherms between 100 and 250 ºC could be easily extrapolated to the "intrinsic volume" V_o of 0.852 cm^3/g, which allowed to estimate the free volume fraction.

The limitation of density measurement in estimating free volume is quite obvious in that it can only provide the information of total fraction of free volume. Information about the distribution, the shape and location of these free spaces can not be obtained. In addition, it is hard to follow the evolution of free volume when system is subjected to external changes like stretching.

Positron Annihilation Lifetime Spectroscopy (PALS)

PALS is so far the most popular technique utilized in determining the polymer free volume size and size distribution. Although data of PALS on polymers have been

published for over 40 years, it is only since late 1980s that the importance of PALS in polymer free volume evaluation was appreciated, as first by Kobayashi and co-works [60-62]. During the past decade PALS has developed to be the most popular method for studying sub-nanometer size holes in polymers.

The positron, e^+, is the anti-particle of the electron, e^-, which annihilates as a result of collision with an electron to generate photons of a specific energy. Positrons are generated by the decay of certain unstable isotopes; one of the most commonly used being which $^{22}_{11}\mathrm{Na}$ decays to $^{22}_{10}\mathrm{Ne}$ with the simultaneous emission of e^+ and a γ-ray. The positrons emitted have a distribution of energies between zero and 540 keV, with a maximum at around 200 keV.

When a positron is implanted into a condensed matter such as polymer, the positron can annihilate as a free positron with an electron or form a metastable state, called positronium (Ps), together with an electron. According to spin configuration of positron and electron, Ps is born in two spin states as: *para*-positronium (*p*-Ps) (anti-parallel) and *ortho*-positronium (*o*-Ps) (parallel) with relative abundance of 1:3. The *p*-Ps has a very short lifetime of 125 ps in vacuum so that it annihilates by itself in the matrix before being able to interact with the surroundings. On the other hand, due to the long lifetime (140 ns) of the *o*-Ps in vacuum, the positron in the *o*-Ps can pick up an electron from its surroundings and be annihilated with it so that its lifetime is shortened to several nanoseconds depending on the electron density at the annihilation site. This process is called pick-off annihilation. Therefore, three components of the positron lifetime can usually be recognized in polymers except PTFE: two short lifetimes, τ_1 and τ_2 are assigned to the self-annihilation of the *p*-Ps and free positron annihilation, respectively;

the long one, τ_3, is due to the pick-off annihilation of the *o*-Ps. Due to the small size of *o*-Ps (1.06Å), PALS is rather sensitive to small holes and can detect molecular motion in a time of 10^{-10} s and longer. Numerous PALS studies of glassy and rubbery polymers showed that positron lifetime distribution includes a single long-lived *o*-Ps component with lifetime in the range of 1.5~3.5 ns [63]. While for some highly permeable, high free volume polymers, a much longer lifetime, τ_4 was observed to be up to 14 ns [64]. It has been known that *o*-Ps lifetime is proportional to the size of the cavity where it is trapped. The positron lifetime increases when positron is trapped in larger size defects or voids due to the locally reduced electron density of the defects or voids. Thus the intensity of this long lifetime component is directly related to the defect concentration. Therefore *o*-Ps annihilation rate and yield give a direct measure of the voids in the materials.

Several models were proposed to correlate the *o*-Ps lifetime τ_i and the size of free volume void *R*. Among those, a semi-empirical model by Nakanishi and Jean [65, 66] appears to be the most successful to determine the absolute mean size of free volume:

$$\tau_i = \frac{1}{2[1-(R/R_0)+\frac{1}{2\pi}\sin(2\pi R/R_o)]}$$

where $\tau_i = \tau_3$ or τ_4 is the *o*-Ps lifetime (ns), *R* is the free volume cavity radius (Å) and R_o = R + 1.656Å (effective electron layer thickness with which a positronium interacts in an infinitely deep potential well). However, it should be noted that this model is based on equivalent spherical free volume voids. In reality a better approximation like cylindrical shape should be considered, which corresponds to the bundle morphology that develops between the chains. It was shown that assuming the presence of cylindrical holes the PALS data will be weighted towards smaller dimensions [67]. In addition to the absolute

mean size of free volume, information on the distribution of free volume can be obtained from PALS spectrum by fitting it to a continuous distribution of intensities as a function of mean lifetime using a computer code called CONTIN [68]. Using a numerical Laplace inversion method by CONTIN, raw PALS spectrum can be resolved into intensity distribution curve according to different positron lifetime. Typical raw PALS spectrum and convoluted 3-component PALS spectrum for polymer are shown in Figure 2-5.

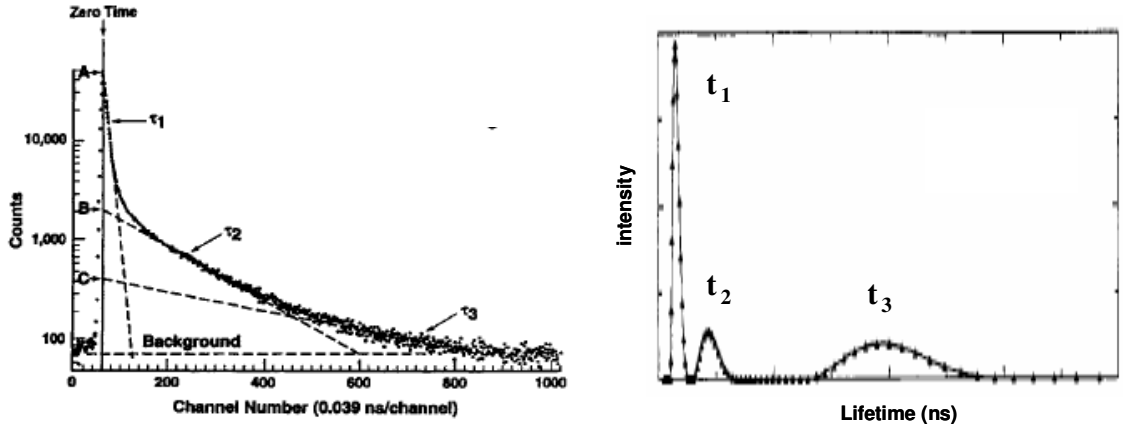

Figure 2-5 Typical raw (upper) and resolved (lower) PALS spectrum of polymer

Numerous investigations of PALS in free volume and free volume distribution have been carried out on commercial thermoplastic polymers (PE, PP, PMMA, PS, PVAc …), engineering polymeric materials (PET, polycarbonate, Nylon, polyimides …), membranes (PVTMS, PTMSP), epoxy and so on. The evolution of free volume and its distribution in polymers has also been studied under various conditions including tacticity, various molecular weight and molecular weight distribution, stretching, temperature and pressure change, plasticizer effect, physical aging and so on. Some typical results obtained from PALS are tabulated in Table 2-2.

Table 2-2 Summary of *o*-Ps lifetime and corresponding calculated void size of some polymers determined from PALS

Polymer			Positron Lifetime τ_{Ps} (ns)	Mean Void Size (Å^3) [a]
PE	Draw Ratio[69]	1.0	2.34	131
		2.5	2.33	128
		5.5	2.27	122
		12.0	2.15	108
	LDPE[70]		2.68	~ 135
	HDPE[71]		~ 1.4 (crystalline phase)	~ 46
			~ 2.7 (amorphous phase)	~ 168
PP[72]	syndiotacticity	76.5%	2.17 ± 0.03	~ 113
		98.0%	2.19 ± 0.03	~ 115
PS	atactic[73]	25 ºC	2.040 ± 0.009	~ 100
		90 ºC	2.052 ± 0.008	~ 102
		130 ºC	2.106 ± 0.009	~ 108
	syndiotacticity[74]	55%	2.11 ± 0.01	~ 108
		70%	2.07 ± 0.02	~ 104
PMMA	10 ºC ~ 150 ºC[75]		1.84 ~ 2.54	82 ~ 150
	304 K[76]		~ 1.96	~ 93
PVAc	-30 ºC ~ 35 ºC[62]		1.77 ~ 1.96	76 ~ 93
	hydration wt% [77]	6.5%	1.34	41
		15%	1.65	66
		30%	1.96	93
		60%	1.92	90
PAN[78]	room temperature	25ºC	1.916	89
PVC[79]	plastisizer%	0%	1.785 ± 0.126	~ 77
		15%	1.946 ± 0.04	~ 91
		35%	2.249 ± 0.022	~ 121
Nylon 6[80]	25 ºC ~ 220 ºC		1.69 ~ 2.37	70 ~128
	humidity	0% ~ 32%	1.693 ~ 1.595	70 ~ 62
		45% ~ 100%	1.610 ~ 1.942	63 ~ 92
PET[81]	30 ºK ~ 300 ºK		1.42 ~ 1.69	47 ~ 69
Nafion[82] (perfluorosulfonated PTFE)	hydration wt%	dry	2.86 ± 0.01	~ 186
		21%	2.73 ± 0.01	~ 178
		27%	2.69 ± 0.01	~ 168
		35%	2.59 ± 0.01	~ 156
	EtOH swollen		3.06 ± 0.01	~ 208
Polysulfone[83]	260 K ~ 370 K		121 ~ 1.75	32 ~ 74
Polycarbonate	260 K ~ 370 K[83]		1.06 ~ 1.37	22 ~ 43
	strain%[84]	0 ~ 7%	2.0 ~ 2.05	97 ~ 102
Polyethersulfone[83]	260 K ~ 370 K		1.17 ~ 1.55	30 ~ 58
cis-PBd[85]	50 K ~ 260 K		1.04 ~ 2.60	21 ~ 157
	T_g = 167 K		~ 1.36	43
PEEK[86]	independent of crystallinity		~ 1.8	~ 79
Polyimides[87]	PI4 [b]		3.7 ± 0.01	~ 282
	BAAF [b]		3.23 ± 0.017	~ 227
	PAI [b]		2.82 ± 0.103	~ 180
PDMS[88]	T_g = 165 K, T_m = 235 K		~ 1.8, ~ 3.4	~ 79, ~ 246
Epoxy[89] [c]	pressure (25 ºC)	0 kbar	1.632 ± 0.011	~ 64
		1.8 kbar	1.255 ± 0.008	~ 35
		4.9 kbar	0.871 ± 0.011	~ 12

	14.0 kbar	0.588 ± 0.02	~ 2
PPO [d]	room temperature [e]	τ_3 = 1.38, τ_4 = 4.10 [90]	v_3 = 44, v_4 = 333
PTMSP [d]		τ_3 = 2.47 [90] (2.68 [91]) τ_4 = 6.67 [90] (10.9 [91])	v_3 = 143 (165) v_4 = 678 (1317)
PVTMS [d]		τ_3 = 2.88 [90] (2.41 [91]) τ_4 = 4.90 [90] (4.20 [91])	v_3 = 187 (137) v_4 = 434 (344)

[a] Calculated from semi-empirical equation assuming spherical shape of voids

[b] PI4 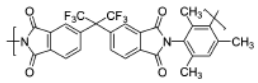 BAAF 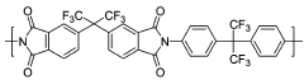 PAI 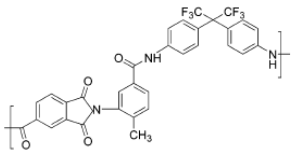

[c] Based on DGEBA/DDH/DAB

[d] High free volume polymers: PTMSP - polytrimethylsilylpropyne; PVTMS – polyvinyltrimethylsilane; PPO – polyphenylene oxide

[e] Long lifetime component τ_4 was observed for ultra-high free volume polymers

Although PALS is so far the most popular technique to evaluate free volume and free volume distribution in polymers, some limitations should be reminded. First, the total free volume cannot be estimated with this method. It is always difficult to resolve the discrete lifetime components unambiguously when two of the lifetimes differ by less than a factor of 2 [68]. It is also important to realize that PALS is a dynamic method of measurement with a time scale of 10^{-9} s. Molecular vibrations with a frequency higher than 10^9 Hz will therefore contribute to the occupied volume. In addition, it was pointed out by Yu et al [92] that positronium has a threshold for detecting free volume holes; i.e., it can probe only holes larger than a size corresponding to the minimum for *o*-Ps localization. It was also found that since *o*-Ps does not remain in a single hole during its lifetime (the chance for a Ps atom to remain in one particular hole for its entire lifetime is on the order of 1%), each positronium atom will sample a number of holes of different sizes before annihilating with an electron. Therefore the lifetime of *o*-Ps only reflects an average over the distribution of free volume hole sizes in polymer materials rather than a direct measure of the hole size distribution.

X-ray Scattering

Information of free volume size in glassy polymers can also be deduced from scattering techniques, like small-angle X-ray scattering (SAXS). Since 1983, SAXS has been extensively used by Roe et al [93-95] to determine the density fluctuation and its change under various conditions and thus to obtain a measure of a free volume size distribution in glassy polymers.

The feasibility of using SAXS to detect free volume size lies in its sensitivity to the density distribution of electrons and in consequence of atoms, which yields information on changes in morphology or of the structure on a super-molecular level. Scattering of X-rays at small angles from an amorphous, single-phase, single-component material arises from the presence of spatial electron density fluctuation, which is caused by the irregular, liquid-like placement of atoms, i.e., the statistical variation of the local packing density of atoms. Such density fluctuation arises from the frozen disorder as well as the residual thermal motion in the case of glassy polymers. Within a reference volume v of arbitrary shape and size, as we move this reference volume around in the sample, the number N of electrons falling within the volume will fluctuate about the mean $\langle N \rangle$. The extent of fluctuation is expressed by the variance $\left\langle (N - \langle N \rangle)^2 \right\rangle$. The density fluctuation is defined unambiguously as

$$\psi(v) = \frac{\left\langle (N - \langle N \rangle)^2 \right\rangle}{\langle N \rangle}$$

$\psi(v)$ can be determined from the knowledge of the intensity $I(s)$ of scattered X-rays as a function of scattering angle s ($s = 2\sin\theta/\lambda$). In a scattering measurement, if the atoms are regarded to occupy well-defined, finite core volume, then a non-uniform

distribution of local free volume would necessarily manifest itself as non-uniformity in the local density, i.e., density fluctuation. Thus the free volume can be deduced from the density fluctuation obtained. Roe and Curro [94] annealed polystyrene slightly below T_g while conducting SAXS measurements finding a slow reduction in density fluctuations on a size scale reported as 8000 $Å^3$. Below 80 ºC, however, the density fluctuations remained constant even though bulk specific volume continued to decrease at temperatures as low as 61.3 ºC. This small scale homogenization was attributed to a change in the distribution of local free volume, indicating that whereas the specific volume might provide a measure of the average free volume content, the density fluctuation can be interpreted to reveal the distribution of free volume. From the density fluctuation data, Roe and Song [93, 95] also estimated that the weight average size of the holes in PMMA to have a volume of 105 $Å^3$. X-ray scattering patterns of PS samples subjected to five different methods of inducing volume change were recorded by Song and Roe [96]. The change in density fluctuations over a volume range of 4 - 4000 $Å^3$ was measured. Their results showed that the large scale density fluctuation correlates fairly well with the change of specific volume, irrespective of the different methods used to induce it. On the other hand, the small scale density fluctuation, indicating the degrees of local ordering, depends very sensitively on the method of volume change employed. It was also found that the density fluctuations in unannealed PS reached maximum at a volume of about 30 $Å^3$ and decreased steadily as the volume increased. Using SAXS Tanabe et al [97] also revealed the apparent absence of structural density fluctuations in PMMA glass on a size scale larger than “several tens of angstrom”.

Fluorescence Probe Technique

Fluorescence spectroscopy is growing remarkably as an effective and non-destructive tool to study microstructure and mobility of solid polymers [98]. Application of fluorescence and photochromic molecular probe in glassy polymers was first by Gardlund [99] who successfully studied the thermal back reactions of two benzospirans in PMMA films at 300 °K. Although many studies had been made following Gardlund's work, there is no successful method of analyzing thermal back reactions with regard to local free volume in polymers. In 1971, Priest and Sifain [100] measured the photo-induced *trans-cis* photoisomerization of photochromic monoazo compounds in glassy polystyrene-n-butyl benzene. It was found that 2, 2'-azonaphthalene isomerized more in quenched PS film than in film annealed for 3 weeks, indicating the possibility of fluorescence probe technique in detecting the size of free volume voids. Later extensive work by Sung et al [101-104] and Victor et al [105, 106] further demonstrated the sensitivity of photochromism to the changes in the local free volume distribution in polymers.

Photochromism is the reversible change of a chemical between two or more species which have different absorbance spectra that can be induced in at least one direction by absorption of light. The versatility and sensitivity of fluorescence stem from the multiple aspects of the interaction of electronically excited states with their immediate environment. By monitoring the fluorescence, which is sensitive to molecular motion of the chromophore, such as rotation or conformational change, the size and size distribution of free volume voids can be determined. The assumption is that the kinetics of photo-isomerization of probes in glassy polymers requires a minimum critical size of local free

volume in the vicinity of the chromophore. Upon irradiation probes are excited to a singlet state. The excited probes return to their ground state either by emitting fluorescence or by dissipating the energy through friction or momentum transfer to the matrix, i.e., internal conversion. If sufficient free volume is available in a host matrix for the free motions of probes, the probes are more likely to return to their ground state by internal conversion. On the other hand, if the motions of probes are severely restricted or impeded due to increasing the surrounding media rigidity, viscosity or limited free space, the probes are more likely to emit photons, i.e., fluorescence. Thus, the fluorescence yield or intensity is directly related to the free volume around it. Loutfy [107] has suggested an expression describing the relationship between fluorescence intensity and free volume fraction in glass polymers:

$$\phi_f = \phi_o \, exp(\beta \frac{V_0}{V_f})$$

where V_0 is a critical volume necessary for the motion of the spectroscopically active group in the probe molecule, V_f is the free volume of the polymer, ϕ_f is the fluorescence intensity, ϕ_o is the fluorescence intensity of unhindered probes and β is a system-dependent constant. The above equation indicates that the fluorescence yield increases with decreasing free volume. As an example shown in Figure 2-6[107], the sharp increase in fluorescence intensity correspond to the increase of medium viscosity or decrease in free volume from fluid to rigid glass during polymerization.

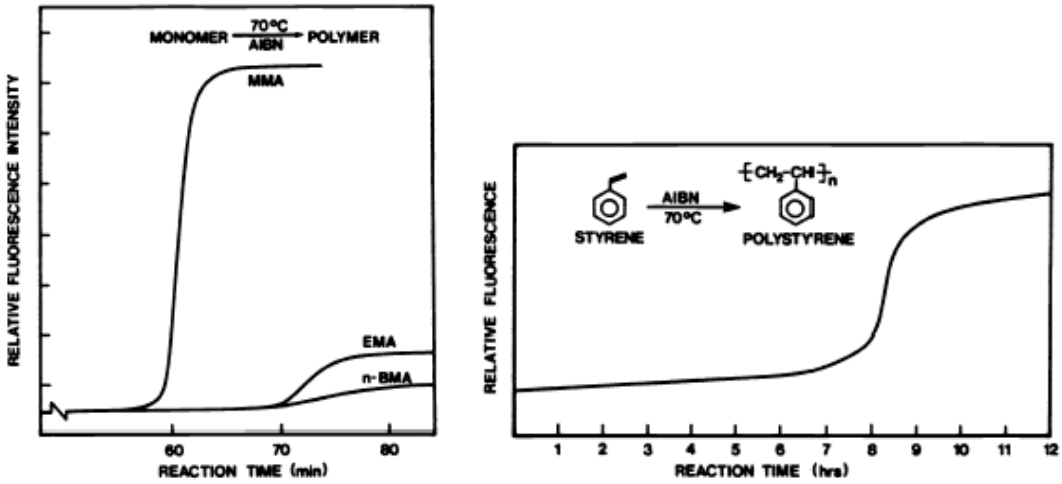

Figure 2-6 Dependence of fluorescence intensity on the polymerization of methyl methacrylate, ethyl methacrylate, n-butyl methacrylate (left) and styrene (right)

The free volume and its size distribution have also been probed by the use of photochromic labels such as *trans* ↔ *cis* photoisomerization of azobenzene chromophores [101-104, 106, 108]. The change is monitored via absorption spectra instead of emission as mentioned above. Polymer matrix containing *trans* isomer is irradiated to photo-equilibrium and the *cis* isomer fraction is determined from the spectrophotometric absorbance, which is then used to determine free volume information. It was reported that [102] photoisomerization of the azobenzene label was progressively impeded as physical aging proceeds, reflecting the disappearance of free volume above a certain size. Eight probes of different required photoisomerization volume (127 $Å^3$ ~ 571 $Å^3$) were used by Victor et al [105, 106] to probe the free volume distribution in atactic PS as a function of physical aging. The median of the local free volume in unannealed PS was found out to be 260-280 $Å^3$, with over 90% of voids larger than 100-120 $Å^3$ and practically none larger than 400 $Å^3$. The larger free volume decreased more than the smaller ones during physical aging and the greatest loss of free volume occurred in the range larger than 280 $Å^3$, but the amount of loss varied with annealing temperature.

Experimentally, fluorescent probes can be inserted as independent molecules, as well as being attached in main chain or side groups as labels. Detailed free volume distribution information in PS was obtained by incorporating the azobenzene chromophores as molecular labels at three specific sites: chain end, chain center, and the side group [101, 104]. As observed, end labels always photoisomerize the fastest. The magnitude of the reaction was the greatest for the free probe, followed by chain ends, side groups, and chain center in decreasing order, indicating the inhomogeneous free volume distribution. Similar site-specific labeling technique was used to evaluate the free volume environment in an epoxy-diamine network [103]. The sites investigated were the crosslinker, the chain end and the dangling chain. Throughout the cure process, at the crosslink sites, the fast fraction decreased sharply at the gel point, after which no photoisomerization occurred. At dangling chain, the fast fraction decreased more slowly. The average free volume size was found to be reduced from ~ 8 $Å^3$ in radius before cure to ~ 6.5 $Å^3$ in radius after cure.

Therefore, the technique of fluorescence probe or labeling allows us to study both the static and dynamic changes in free volume and free volume distribution of polymers as a function of polymerization, molecular weight, stereoregularity, crosslinking, and polymer chain relaxation etc. However, the limitation is that it is only effective in polar polymers since the fluorescence emission maxima are sensitive to media polarity.

Other Techniques

Other techniques are also used to evaluate the free volume in polymers, like gas sorption and permeation in inverse gas chromatography (IGC) and spin probe technique.

IGC is a technique for investigation of sorption thermodynamics of polymer-solute mixtures and is particularly used in polymer membranes with high permeability. It

is based on measurement of retention times of solutes in a column containing the polymer of interest, which are related to the net retention volume V_N. Using the V_N values various thermodynamic quantities can be found like enthalpy of sorption, ΔH_m and entropy of mixing, ΔS_m. As partial molar enthalpies of mixing are strong functions of molecular sizes of solutes in glassy polymers, it has been assumed that the molecular size of the solute, which corresponds to the minimum at this dependence, is close to the mean size of free volume elements in the polymer [109]. Therefore, the coordinates of ΔH_m at minimum versus solute size provide estimates of the size of free volume in polymers. The thermodynamics of sorption of various solutes in poly (vinyltrimethylsilane) (PVTMS) was studied by Yampolskii et al [109] using IGC. It was found that from propane to hexane the dimensions of solute gradually approached the average or limiting dimensions of the free volume cavities, thus the adsorption of the probe was accompanied by a progressive decrease in ΔH_m and ΔS_m. More recently, the sorption and permeation of light gases, hydrocarbons, and perfluorocarbons in two amorphous copolymers, AF1600 (65 mol% 2,2- bis(trifluoromethyl)-4,5-difluoro-1,3-dioxole (BDD) and 35 mol% tetrafluoroethylene) and AF 2400 (87 mol% BDD), were studied by Alentiev et al [110]. A bimodal size distribution of free volume was observed and the larger free volume in AF1600 had a radius of ~ 5 Å. However, due to less amount of bulky, packing-disrupting BDD, AF1600 showed a lower solubility than that AF2400, consistent with the lower free volume. In addition, IGC results for several highly permeable glassy polymers were obtained [111], which showed a consistent decreasing order of free volume size (AF2400 > poly(disilylnorbornene) > AF1600 > PVTMS) with that from PALS measurements. Similarly, Levita and Smith [112] investigated the diffusion of gases in strained PS film.

They found that diffusion coefficients for Xe and CO_2 in a strained film decreased with time at constant strain and that the diffusion coefficient for Xe decreased more rapidly than that of CO_2. They concluded that the larger Xe atoms need larger free volume through which to diffuse than CO_2 and that, during the annealing with applied strain, the larger free volume decreased in size more rapidly than smaller ones.

Spin probe technique has only been only sporadically used in relation to free volume in polymers. It is based on the correlation existing between the rotation frequency of spin probes and gas diffusion coefficients. This effect could be explained by the analogous effects of free volume on these parameters. Whether or not a spin probe can be accommodated by free volume depends sensitively on the size of the probe and is reflected in the frequency of the probe's rotation as sensed by ESR. Therefore a rough estimate of the size of free volume can be made based on spin probes of various sizes. Using a stable radical, 2,2,6,6-tetramethylpyperidine-1-oxyl (TEMPO), Yampolskii et al [113] evaluated the free volume size in copolymers of TFE and 2,2-bistrifluoromethyle-4,5-difluoro-1,3-dioxole, polyacetylenes and polynorbornenes. It was found that the rotation of the probe was facilitated in high free volume media. Polymers distinguished by ultrahigh permeability and free volume exhibited large rotational frequency. It was interpreted that for which the frequency of TEMPO rotation is higher than 0.5×10^9 s^{-1}, the size of free volume is larger than or comparable with the size of TEMPO, i.e. 100 Å.

Summary

Except dilatometry and SAXS, all techniques discussed here are probe methods although they are based on different physical principles. A list of these probe methods is summarized in Table 2-3. In these methods, the relation between the dimensions of the

probes and free volume microcavities where they reside determines their behavior in the polymers. In contrast to PALS and ^{129}Xe NMR, all other probe methods employ series of probes with varying sizes: by observing the behavior of smaller and larger probes, estimations on the free volume size can be made.

Table 2-3 Summary of probe methods for investigation of polymer free volume

Method	Probe	Probe Size	Information
Positron annihilation lifetime spectroscopy (PALS)	*o*-Ps	1.06 Å	Size and size distribution of free volume, temperature and pressure dependence
^{129}Xenon NMR	^{129}Xenon	4 Å	Size of free volume cavities and its temperature dependence
Fluorescence and photochromic probe method	Stilbene, azobenzene derivatives	120 Å ~ 600 Å	Size distribution of large free volume holes and temperature dependence
Inverse gas chromatography (IGC) and gas permeation	Light gases, hydrocarbons	> 5 Å	Temperature averaged mean size of free volume
Spin probe method	Stable free radicals	> 100 Å	Information on size of large free volume holes

Now that various probe methods have been applied for investigation of free volume in certain polymers, a question can be asked about reliability of the results of these methods. From above sections it can be noted that observations based on different methods are in reasonable agreement. As will be shown in following sections, these experimental results are also reasonably consistent with the predictions from theoretical estimation and computational modeling of the same polymers.

2.2.3. Theoretical and Computational Characterization of Polymer Free Volume

Since experimental methods are sometimes laborious and may involve some ambiguities when explaining the results in terms of free volume and its distribution, computational approaches provide an alternative way. The versatility of simulation lies in the fact that it enables variety of "measurements" to be performed to evaluate properties of polymers that conventional laboratory experiments cannot easily provide.

A theoretical determination of the free volume requires an accurate description of the atomistic structure of polymer. Several molecular modeling methodologies have been developed for obtaining a detailed structure of polymers under various conditions. Among those molecular dynamics simulation as well as Monte Carlo simulation is mostly employed, which provide with fair accuracy the configurations (position coordinates, velocity, etc) under different conditions. From the computationally generated molecular configurations the spatial free volume is then evaluated using algorithm techniques like Voronoi tessellation and hard sphere probe method. Some other models have also been developed such as the model based on kinetic theories and lattice model, which also prove to be efficient in evaluating free volume and free volume distribution in polymers.

Molecular Dynamics (MD) Simulations

MD is a method that studies the motions and the conformational space of molecular systems by integration of the classical Newtonian equations of motion given a potential energy function and its associated force fields. MD is a powerful technique in simulating behavior of polymeric materials under various conditions due to its versatility. It can provide information on the time evolution of a system as well as its time-averaged properties, thus allowing the study of many kinetic aspects of the glassy polymers.

MD simulations on *n*-alkane-like molecules have been done comprehensively by Rigby and Roe [114-116]. In a typical MD simulation, a united-atom model was adopted, in which individual *n*-alkane chains were modeled as sequences of spherical CH_2 (or CH_3) segments connected by spring-like valence bonds. The system is subject to bond potential energy restricting bond lengths and angles, *trans-gauche* torsional potential and non-bonded Lennard-Jones 6-12 potential due to neighboring chains. The model system is a cubic simulation box with periodic boundaries, filled with several hundreds of chains. The integration of the equation of motion was performed using a modified Verlet algorithm and the integration time step and the relaxation time were carefully chosen. At the end of each run of simulation duration, the system configuration was saved and used to start a second run of duration. The saved configuration output at intervals during these longer runs were then used to perform free volume analyses.

Several techniques have been developed to extract the information of free volume and free volume distribution from the trajectories of MD simulations. There are geometrical techniques like Voronoi tessellation and hard sphere probe method and non-geometrical analysis method based on energetic approach. The details of Voronoi tessellation and hard sphere method can be found in the Methodology part in Chapter 3. Based on energetic considerations, in't Veld et al [117] developed a new algorithm for obtaining cavity size in any liquid structure including polymers. The algorithm used can be summarized in following steps: 1) a liquid or glass structure is generated by MC or MD simulation; 2) remove the force field used to create the simulated structure and a new pure repulsive force field is then applied. All atoms remain fixed at their respective locations; 3) a trial repulsive particle is then randomly inserted into the repulsive force

field and a local minimum in the immediate neighborhood of the particle is determined; 4) after the minimum is determined, attractive interactions are turned on and the size of the trial particle is adjusted so that its potential becomes zero. This unique size is taken to be the diameter of a spherical cavity; 5) a check is then made to determine whether the cavity includes the initial random point of insertion (at step 3). If the initial point is inside the cavity, then the cavity is accepted. If the initial insertion point falls outside the cavity, the cavity is rejected and not counted; 6) repeat steps 3 through 5 for enough times (typically 50 different structures are sampled) to produce a representative distribution of cavity sizes. This new algorithm was applied to two isomeric polyimides of identical chemical composition, which are formed from hexafluorodianhydride and *para* and *meta* isomers of a hexafluorodiamine: poly-6FDA-6FmDA (*meta*) and poly-6FDA-6FpDA (*para*). Differences in cavity size distributions were seen in two isomeric polyimides. The average cavity size was 5.0 Å for the *meta* isomer and 5.4 Å for the *para* isomer. These results are consistent with the experimental observation that gas diffusion in the *para* isomer is faster than in the *meta* isomer even though the *para* isomer has a higher T_g.

Monte Carlo (MC) Simulation

MC simulation methods are distinguished from other simulation methods (such as MD) by being stochastic, that is nondeterministic in some manner - usually by using random numbers (or, pseudo-random numbers) - as opposed to deterministic algorithms. Starting from an arbitrary initial state of the system, a transition into another state is attempted following a certain set of transition rules. In the simplest cases, this transition corresponds to a random jump of a particle or several particles [118]. A somewhat realistic MC model of polymer liquids was developed by Vacatello et al [119] consisting

of short polymethylene chains. Advanced by Suter and coworkers [120, 121], a detailed atomistic modeling of well-relaxed amorphous polymer glass like atactic PP was developed.

The model system is a cube with periodic boundaries, filled with segments from a single "parent" chain. An initial structure is generated by using a modified Markov process, based on rotational isomeric state (RIS) theory and incorporating long-range interactions. This structure is then relaxed by potential energy minimization using analytical derivatives. Computing time is kept relatively small by stepwise minimization, employing a technique of "blowing up" the atomic radii. Then the free volume in the polymer available to penetrant molecules can be obtained from polymer microstructure. To obtain a statistical average, several different structures of the polymer are generated by simulating different configurations of the polymer chain. For these structures, the atoms of the polymer chain (the CH_3 group is considered as a "quasi" atom) are visualized as hard spheres with respective van der Waals radii. A large number of points representing the centers of the penetrant molecules are randomly chosen within the periodic box. These random points are tested for uniformity and reproducibility. From knowledge of the exact location of the atoms, whether a chosen point is located in an unoccupied volume or in an occupied position can be determined. Counters are set up for spheres of different diameters. The maximum size, d_{max}, of an inserted sphere without disturbing the polymer structure is obtained for each point in the unoccupied volume. Counters corresponding to diameters less than d_{max} are incremented by 1, implying that any hard sphere of size less than d_{max} can be inserted at that point. In this way the fractional free volume available to a penetrant molecule can be obtained. Upon MC

modeling, Shah et al [122] determined the total free volume fraction of glassy PP and PVC to be 0.31 and 0.32, respectively due to the similarity in the chemical structures. Trohalaki et al [123] estimated the free volume fraction in siloxane elastomers, PDMS and poly(methylpropylsiloxane) (PMPrS). For a given DP, PDMS had a significantly larger free volume than PMPrS due to chemical difference. The diffusion coefficients estimated from free volume were in semi-quantitative agreement with experiments.

Lattice Model

Chow [124] derived a new distribution function of free volume for amorphous polymers on the basis of a lattice model. A lattice is constructed by considering it consists of n holes and n_x polymer molecules of x monomers. The equilibrium hole number, $\langle n \rangle$, can be determined by minimizing the excess Gibbs free energy with respect to n. A statistical mechanical theory of the density fluctuations of holes has been derived and the hole volume distribution function (g) was expressed in terms of holes numbers, free volume and free volume fraction which, in turn, were uniquely defined by two structural parameters: the energy of hole formation (ε) and the lattice volume (v). This theory provided a good description of the non-Gaussian spreading observed in PALS. It was stated that the non-Gaussian distribution was a result of the large density fluctuations of holes from their equilibrium and the Gaussian distribution was recovered in the limit of small fluctuations. An epoxy resin, DGEBA/DDH/DAB, was studied based on lattice model (Figure 2-7). Results showed that increases in temperature broadened the distribution and shifted to higher free volume and increase in pressure had the opposite effect. These calculated results were in consistent with experimentally measured values.

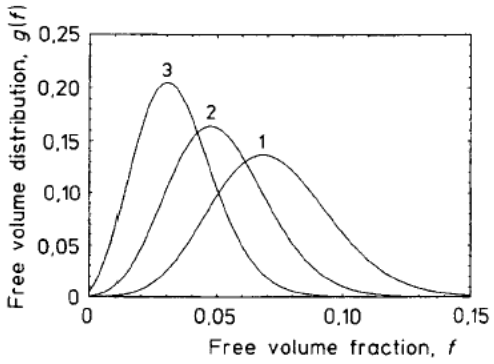

Figure 2-7 Effects of temperature and pressure on the hole distribution function $g(f)$ of an epoxy resin: 1) T=150ºC, p=0.0 kbar; 2) T =100ºC, p=0.0 kbar; 3): T=100ºC, p =1.8 kbar

Gujrati et al [125] studied the end group effects in polymers using a modified lattice model. A lattice of N sites and of coordination number q was constructed. Each polymer chain has exactly b bonds and (b+1) monomers, among which two monomers are end groups and others are middle groups. Each monomer occupies a site and the remaining sites of the lattice are occupied by voids. Then the excluded-volume effects are represented by the requirement that only one monomer can occupy a site of the lattice. The only allowed interactions are between nearest neighbor unlike species. Using the equilibrium lattice theory, the free volume v_E and v_M associated with end group and middle group were calculated respectively, which were shown to be intricate functions of interaction energy, the pressure and the molecular weight. The difference between v_E and v_M could even change sign under certain conditions. It was demonstrated that when the end group and middle group were chemically dissimilar, the middle group might have more free volume than the end group, in contrast to popular belief. When the two groups were similar, the end group would generally have more free volume than the middle group if attractive end-end and middle-middle direct interaction were not strong.

Molecular Kinetic Theory

Molecular kinetic theory has also been applied to explain the phenomenon of physical aging in polymer glasses near T_g in terms of free volume and free volume distribution [51, 126]. The theory is based on the idea that the glass relaxation is a result of the collapse of a series of free volumes having different levels of energies of hole formation. The changes in volume occurring in the glass during relaxation at constant temperature is assumed to arise from changes in the hole fraction. The free volume suggested by this model is the hole fraction that results from the minimization of the configurational Helmholtz free energy with respect to the hole fraction. To model the time-dependent volume contraction and dilatation with temperature, the equilibrium volumes at the respective temperatures, the hole fractions of free volumes, and the fluctuations in free volume were calculated according to the cell model for equation of state for polymer liquids. The kinetic theory was applied to the phenomenon of physical aging of PVC near the glass transition and the results were compared with experimental results. The favorable comparison between theory and experiment substantiated the basic physical picture of linking the equilibrium and non-equilibrium behaviors of free volumes to the distribution of hole energies, its mean value, and the reference conditions.

CHAPTER 3

PREPARATION OF CONTROLLABLE POLYMER ARCHITECTURES

3.1. Synthesis of Telechelic Polytetrahydrofuran

3.1.1. Cationic Ring-Opening Polymerization of Tetrahydrofuran

Tetrahydrofuran reacts with cationic initiators to give PTHF. Such reactions have been the subject of a number of papers since Meerwein [127] reported trialkyloxonium salt as an initiator. In this study, a cationic ring-opening polymerization (CROP) scheme was adopted, in which the propagating species is an oxonium ion that is ring-opened by nucleophilic attack of the additional THF monomer. Trifluoromethanesulfonic anhydride (triflic anhydride, or, Tf_2O) was used as the cationic initiator due to its high initiation efficiency and rate [15, 128, 129]. The vinyl end groups were introduced by end-capping the "living" chains with allyl alcohol to give the telechelic α, ω-diallyl PTHF precursors. Molecular weight was controlled by the concentration of reactants, reaction temperature and reaction time. The CROP scheme of α, ω-diallyl PTHF is shown in Figure 3-1. Deuterated telechelic PTHF oligmers were also prepared in the same manner except that the monomer is deuterated instead of the hydrogenous one.

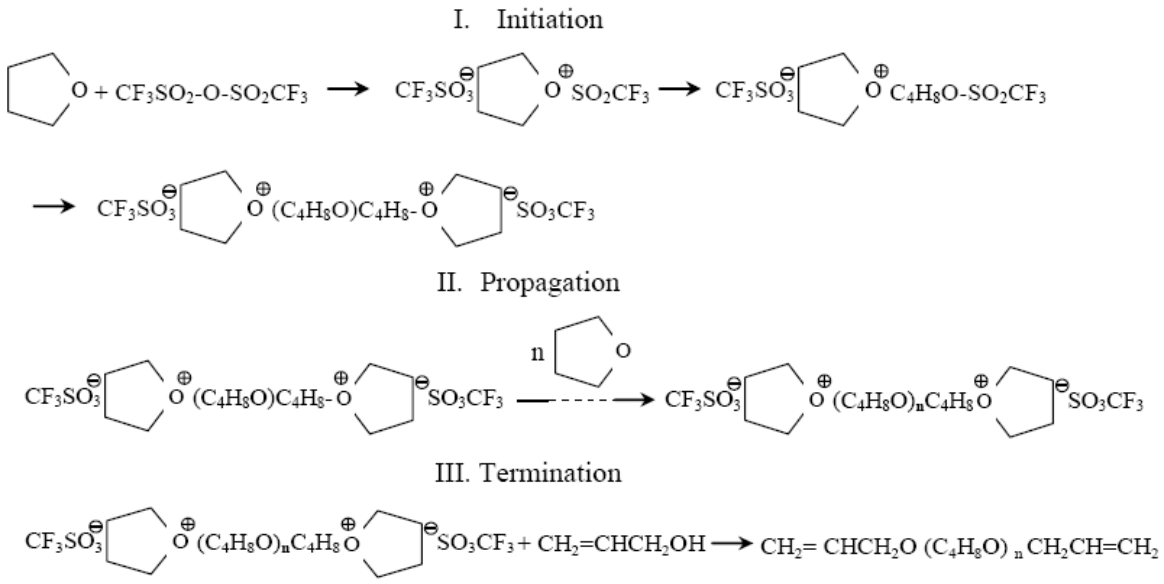

Figure 3-1 Cationic ring-opening polymerization (CROP) of THF

Experimentally, all flasks and utensils were thoroughly desiccated before use under high temperature (150°C) and N_2 purging. All reagents (except Tf_2O) and solvents were firstly treated over 3A and 4A molecular sieves for 48 hours before distillation and dehydration. THF (Sigma-Aldrich, puriss, ACS reagent, 99.5%, inhibitor free) was distilled over potassium-sodium under Ar protection until a deep blue color persisted when adding benzophenone. Dichloromethane (CH_2Cl_2, Sigma-Aldrich, ACS reagent, ≥99.5%) was distilled over calcium hydride (CaH_2) for 24 hours and then sealed under Ar protection. Ally alcohol (Sigma-Aldrich, ≥99.5%) was distilled with potassium carbonate (K_2CO_3) for 24 hours and then sealed under Ar. Trifluoromethanesulfonic anhydride (Sigma-Aldrich, ≥99%, Tf_2O) was used as received.

In a typical case, long-chain PTHF precursor was prepared as following: Tf_2O (3.3 ml, 0.0197mol) was added into 160 ml (1.97mol) of anhydrous THF in a 500 ml three-neck flask under N_2 environment. The reactant mixture was then mechanically stirred at 0°C (cold bath of salt and ice) for 1 hour. After that the living reaction was

terminated by introducing excess anhydrous allyl alcohol (35 ml) and CH_2Cl_2 (82 ml). The mixture was stirred for another 30 min before 18 ml of triethylamine was added to precipitate the acid generated during the termination reaction. The mixture continued to be stirred for about 30 min to complete the neutralization. Most of the solvents including un-reacted THF, allyl alcohol, CH_2Cl_2 and triethylamine were removed under vacuum at 35°C. The remaining mixtures of polymer and salt were then diluted in ethyl ether and thoroughly extracted with distilled water at lease three times. Then the PTHF-ether solution was desiccated over anhydrous magnesium sulfate and filtered. Finally methanol was added to precipitate the polymers at - 60°C in the slurry of dry ice. The precipitates were separated by centrifugation and then dried under vacuum at room temperature until constant weight was obtained. In this case, the yield was about 65% with M_n of ~8000 and a polydispersity of 1.20.

As for the preparation of very short chain PTHF oligomers, typically 8.3ml (0.049 mol) Tf_2O was added into 120 ml (1.48 mol) anhydrous THF at -30°C (cold bath of isopropanol and dry ice). The reaction was last for about 4 min before 35 ml allyl alcohol and 65 ml CH_2Cl_2 were added to terminate the living chains. After 30 min stirring, 30 ml triethylamine was added to neutralize the acid generated. The post treatment of the mixture is the same as in the preparation of long chain oligomers. The yield is about 15% and the molecular weight of the oligomer was of 583 with a polydispersity of 1.02.

3.1.2. Characterization of Telechelic Structure

The end-capped functionality of precursors is crucial for making a structure-determined model networks. Extensive characterizations of the telechelic structure were conducted through IR, Raman, NMR, and Mass spectroscopy.

IR is an invaluable and routine tool in organic structure determination and verification. A typical IR spectrum of PTHF precursor prepared is presented in Figure 3-2. The IR spectra of all the precursors prepared are quite similar except that some absorption peaks are weak due to low end group concentration.

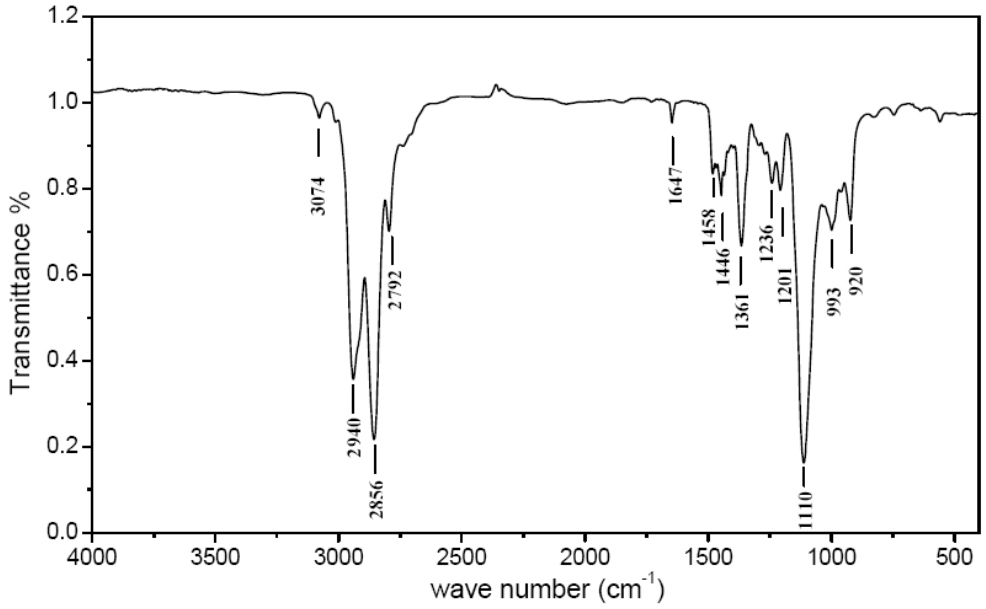

Figure 3-2 IR spectrum of α, ω-dially PTHF precursor

The assignment of the main peaks in IR spectrum is as following: the relatively weak absorption at 3074 cm^{-1} is due to the C-H stretching vibration in $=CH_2$ groups, which indicates the existence of vinyl groups; the strong absorption peaks at 2940 cm^{-1}, 2856 cm^{-1} and 2792 cm^{-1} are due to C-H stretching vibration, which are attributed to the abundant $-CH_2$ groups in backbone; the 1647 cm^{-1} absorption is due to the non-conjugated C=C stretching vibrations at allyl end groups; the absorptions in the range of 1465-1405 cm^{-1} are due to the C-H bending vibrations in CH_2 groups in the backbone; the band at 1361 cm^{-1} corresponds to the CH_2 wagging mode; the peaks in the range of 1290-1109 cm^{-1} are possibly due to the C-O-C asymmetric stretching vibrations in

backbone; the peaks at 993 cm^{-1} and 920 cm^{-1} are related to the C-H out-of-plane bending vibrations in allyl groups. In addition, there is no absorption in the range of 3550-3100 cm^{-1} indicating that the reaction was carried out under strictly anhydrous condition and no -OH end groups were formed. Therefore IR spectrum is in agreement with the designed structure - α, ω-dially PTHF:

$$CH_2=CHCH_2O\text{-}(C_4H_8O)_n\text{-}CH_2CH=CH_2$$

Raman spectroscopy (Renishaw InVia) was also used to determine the telechelic structure of PTHF precursors. A typical Raman spectrum is shown in Figure 3-3.

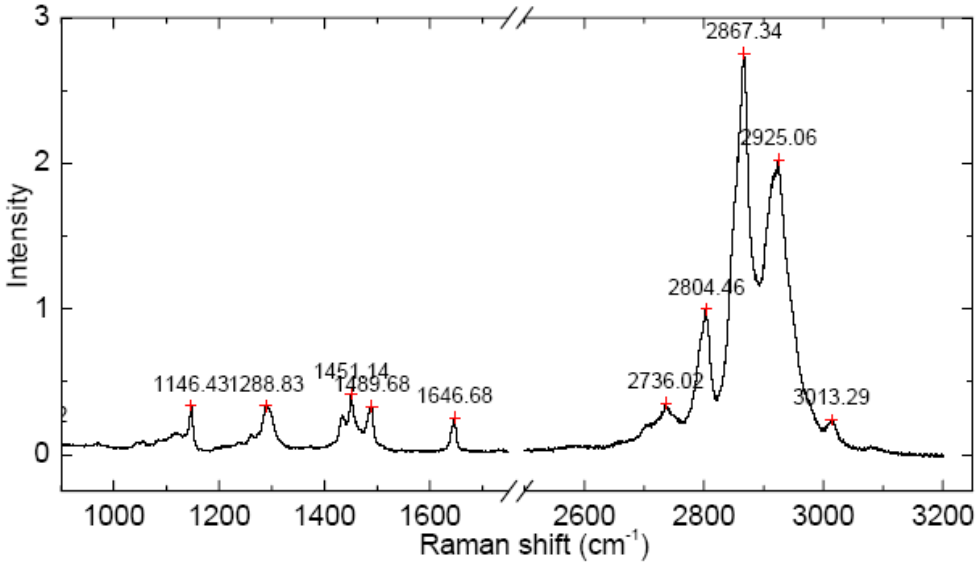

Figure 3-3 Raman spectrum of α, ω-diallyl PTHF precursor

The peak assignment in Raman spectra is quite similar to the peak assignment in IR. In detail, peaks at 1646 cm^{-1} and 3013 cm^{-1} indicate the existence of C=C; strong absorptions in the ranges of 1400 - 1500 cm^{-1} and 2800 - 2925 cm^{-1} are due to the C-H bending and stretching, respectively; 1146 cm^{-1} absorption is ascribe to C-O-C stretching and peak at 1288 cm^{-1} is due to the C-C stretching.

NMR is another complementary technique to elucidate the exact structure of chemicals. Solution ^{1}H NMR spectra of precursors were measured with a Gemini 300 NMR spectroscopy from Varian on 10 wt% solution in $CDCl_3$. The NMR spectra of precursors are quite similar except that some peaks are weak due to low end group concentration. A typical NMR spectrum of PTHF oligomer is presented in Figure 3-4.

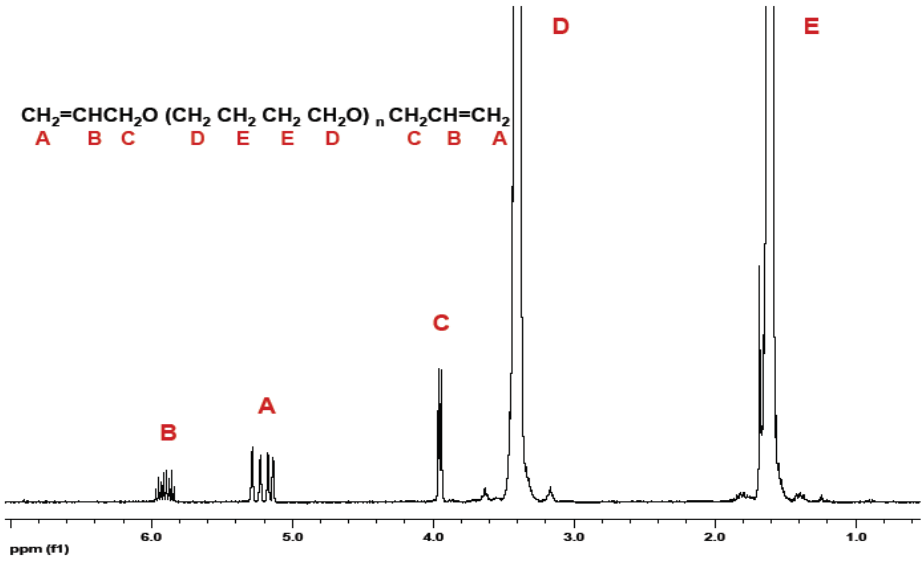

Figure 3-4 NMR spectrum of α, ω-diallyl PTHF precursor

The assignment of the NMR chemical shift peaks is as following: chemical shifts at ~5.9 ppm (A) are assigned to the protons of =CH of allyl groups; peaks at ~5.2 ppm (B) are due to the protons of $=CH_2$; and peaks at ~3.9 ppm (C) are from protons of $-CH_2-$ of end groups; peaks at ~ 3.5 ppm (D) and ~ 1.6 ppm (E) are attributed to the backbone protons. D is from the protons of CH_2. Hence A, B and C are due to the protons in the end groups while peaks D and E are from the backbone protons.

Based on the above analyses, the structure of precursor can be confirmed to be α, ω-diallyl PTHF as designed: $CH_2=CHCH_2O-(C_4H_8O)_n-CH_2CH=CH_2$.

3.1.3. Determination of Molecular Weight

A number of telechelic PTHF precursors (designated by O-1, O-2…) were synthesized through CROP at various concentration levels and reaction temperatures, which control of the molecular weight of precursors. Since M_n of precursors determines the inter-crosslink molecular weight (M_c) of the networks and thus determines the networks properties, accurate characterization of M_n of precursors is of great importance in preparing the networks of known structure. In this study, several techniques, including GPC, NMR, end group analysis, and Mass spectroscopy, were used to determine the M_n of PTHF precursors. Consolidated results of molecular weight of precursors determined through different methods are listed in Table 3-1 at the end of this section (page 65).

Gel Permeation Chromatography (GPC)

GPC was conducted in toluene (1 ml/min) on a Waters system (2690 separations module) using a differential refractive index detector and three Styragel columns at room temperature. Polystyrene was used as calibration standard. Samples were prepared as 15-30 mg/ml solutions. The retention time curves of some prepared precursor polymers are shown in Figure 3-5.

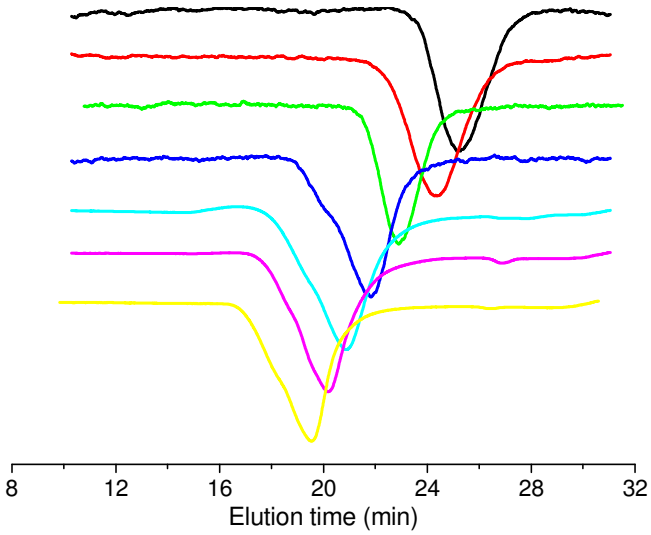

Figure 3-5 GPC elution curves of α, ω-diallyl PTHF precursor

As shown, the precursors prepared are mono-dispersed with PDI in the range of 1.02~1.50. However it is known that GPC only provides the relative values of molecular weight, not the absolute ones. In addition, it has limitation in accurately characterizing small molecules (M_n < 1,500). Thus other techniques have to be used to obtain the absolute values of M_n.

NMR

As shown in Figure 3-4 (NMR spectrum of precursor), three of the five peaks are assigned to the protons in the end groups while two strong peaks are for the protons in the backbone. Therefore the absolute value of M_n can be determined from the intensity ratio of these two groups of peaks. According to the telechelic structure and NMR peaks assignment, absolute value of M_n can be calculated according to following relationship:

$$M_n = \frac{\text{Peaks for backbone H}}{\text{Peaks for chain ends H}} \cdot \frac{10}{8} \times M_{n(\text{repeat unit})} + M_{n(\text{endgroup})}$$

$$= \frac{I_D + I_E}{I_A + I_B + I_C} \cdot \frac{10}{8} \times 72 + 98$$

Molecular weights determined from NMR were compared with the results from other techniques as summarized in Table 3-1. The comparison further proved that the structure of the oligomers is correct with what expected and the M_n measurement is consistent. In the following network preparations, M_n values obtained from NMR measurements were used due to its convenience and much less consumption of samples.

End Group Analysis

End group analysis was carried out for cross-checking the M_n results from NMR and GPC. The end group titration is based on the Hanus method [130], which is widely used to determine the unsaturation (iodine number) of organic substances like fats and oils. The basic chemistry involves direct addition of halogen elements to the double bond:

$$C=C + IBr \longrightarrow \underset{I}{\overset{|}{C}}-\underset{Br}{\overset{|}{C}}$$

Due to the existence of allyl end groups in the oligomers, Hanus method can be employed to accurately determine the absolute molecular weight of PTHF oligmers. Experimental details of the end group titration on telechelic PTHF oligmers are as following: In a typical case, ~ 0.5 g of prepolymers was dissolved in 40 ml of CCl_4 and 25 ml of Hanus solution was added to the mixture. The mixture was allowed to stand for 25 min, and then 30 ml of 15% aqueous KI solution was added to the reacted solution. The solution was vigorously shaken for a few minutes, and then 60 ml of water was

added. The resultant solution containing iodine was then titrated with a 0.1 N $Na_2S_3O_3$ solution.

It was found that the end group analysis method is quite accurate and reliable. However, it is quite time consuming and need a large amount of samples to ensure its accuracy (at lease 3 samples per batch). This method was used occasionally to crosscheck the accuracy of NMR results.

MALDI-TOF and FAB-MS

For narrowly distributed long-chain PTHF prepolymers, matrix-assisted laser desorption/ionization time of flight (MALDI-TOF) mass spectroscopy was used and for short-chain oligomers (M_n < 1,500), fast atom bombardment mass spectroscopy (FAB-MS) was used. The effective matrix of PTHF oligomers for MALDI-TOF measurements was 2, 5-Dihydroxybenzoic acid and 2-4(4-hydroxyphenylazo) benzoic acid. A typical MALDI-TOF spectrum is shown in Figure 3-6.

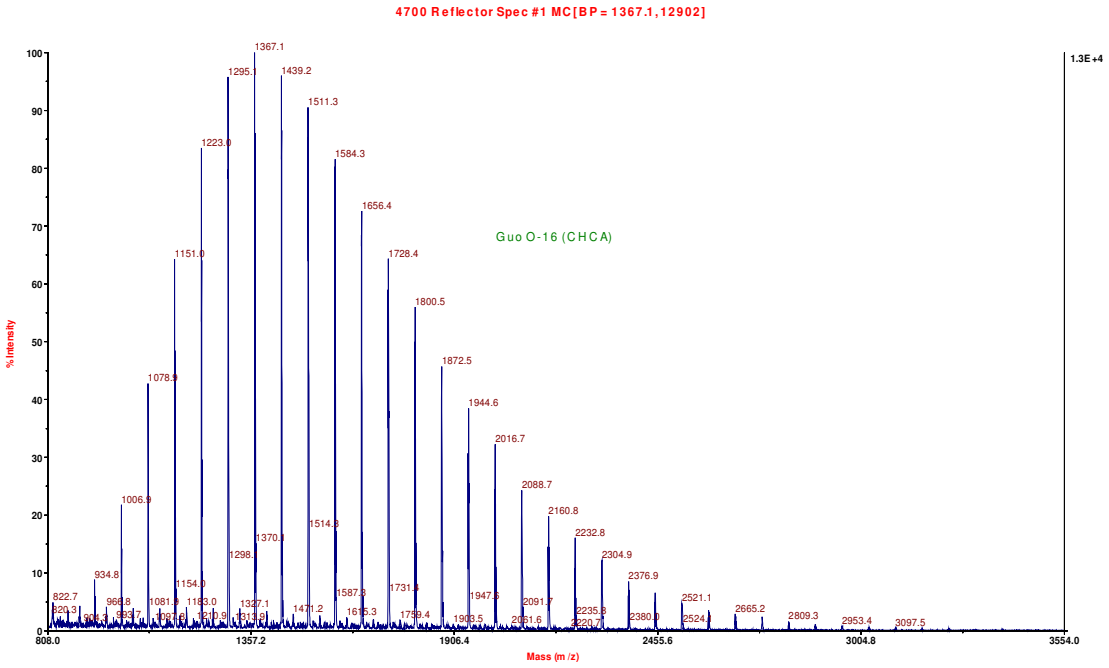

Figure 3-6 MALDI-TOF spectrum of α, ω-diallyl PTHF precursor

As shown, the interval of 72 between spikes in MALDI-TOF spectrum represents the repeat unit of $-C_4H_8O-$ and the polymer is quite mono-dispersed. From the intensities (abundance) of the spikes (N_i) and mass of the ith oligomer (M_i), M_n, M_w and PDI can be determined according to:

$$M_n = \frac{\sum N_i M_i}{\sum N_i} \qquad M_w = \frac{\sum N_i M_i^2}{\sum N_i M_i} \qquad \text{PDI} = M_w / M_n$$

For short-chain oligomers, FAB-MS turned out to be a valuable tool to determine the molecular weight and the structure. In FAB-MS, the sample is usually dissolved in a non-volatile matrix rather than being introduced directly in the pure state on a sample probe. The sample is desorbed by interaction with a beam of energetic fast atoms. This method of desorption results in relatively low energy transfer and a concomitant lack of fragmentation that characterizes more energetic (e.g. EI-MS) mass spectrometric method. Because of this lower level of fragmentation, molecular ions may be more readily observed. A typical FAB-MS spectrum of short-chain oligomer is shown in Figure 3-7.

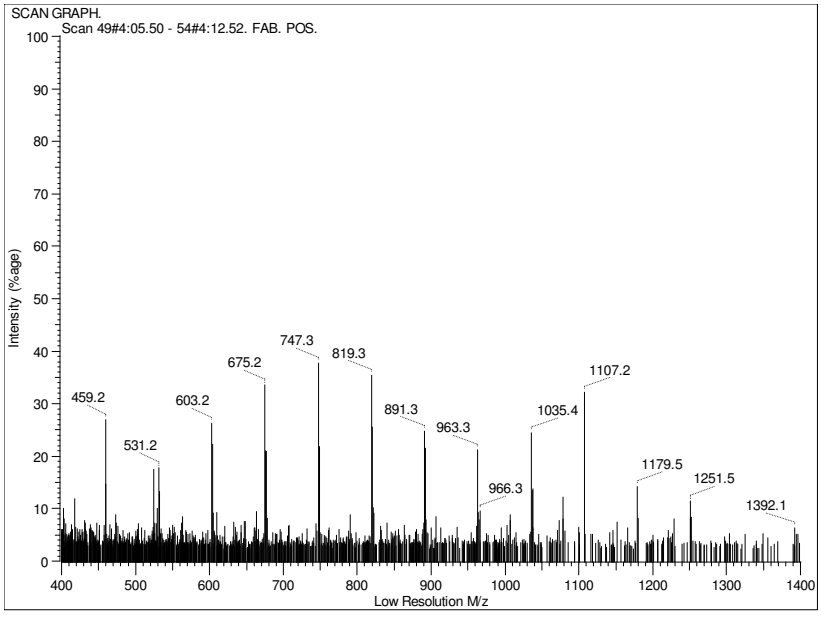

Figure 3-7 FAB-MS spectrum of α, ω-diallyl PTHF precursors

The positions of the spikes in the FAB-MS spectrum can be easily identified as:

$$\text{Reading value} = (M_n \text{ of repeat unit}) \times DP + 98 + 1$$

where DP is the degree of polymerization, 98 is the molecular weight of end groups and 1 is the proton attached to the molecules due to bombardment. Taking spike 819.3 as an example, calculation gave DP value of exactly 10, indicating that the structure of PTHF oligomers is just what we have designed with repeat unit of C_4H_8O and end groups of allyl groups with M_n of 98.

Consolidated results of M_n of some oligomers determined from different methods are listed in Table 3-1. As seen from the table, M_n values determined from independent techniques are quite consistent, indicating that the end-cap reaction is complete and the oligomers have the designed telechelic structure. Considering the efficiency and sample amount requirement, NMR was chosen as the main technique to determine M_n of the precursors in this research.

Table 3-1 Summary of molecular weight of PTHF oligomers

Sample	***NMR***	***C.T.****	***MALDI/FAB-MS***		***GPC***	
	M_n	M_n	M_n	PDI	M_n	PDI
O-28	17669	16025	-	-	20050	1.50
O-22	13051	12648	14880	1.27	15760	1.33
O-21	11546	10840	-	-	13586	1.40
O-15	8070	8265	8235	1.33	8844	1.28
O-14	6215	6093	-	-	6627	1.15
O-11	4908	4720	5023	1.25	5859	1.09
O-4	3246	3077	3402	1.30	3717	1.13
O-7	2243	2020	2204	1.12	2635	1.16
O-16	1526	1488	1555	1.05	1938	1.08
O-23	917	-	1000	1.04	-	-

O-19	853	-	823	1.07	-	-
O-9	607	-	-	-	-	-

* C.T. – chemical titration

Similarly, deuterated telechelic PTHF oligomers were prepared in two batches: short chain oligomer (M_n = 925) and long chain oligomer (M_n = 12,800). These deuterated PTHF precursors were used to prepare the selectively labeled model networks.

3.1.4. Thermal Behavior of Telechelic PTHF Precursors

PTHF is usually used as the soft segment component in the segmented polyurethane and polyester block polymers. Since the molecular weight and molecular weight distribution of PTHF precursors determine the intercrosslink molecular weight and molecular weight distribution in networks, it is of great importance to understand the thermal behavior and its dependence on the molecular weight of precursors before they are incorporated into model networks.

The thermal behavior of PTHF precursors was investigated by differential scanning calorimetry (Seiko Instruments Model DMS210). Typically the scan rate was 10°C/min ramping from -120°C to 90°C and two cooling-heating cycles were done on each sample. The glass transition temperatures, peak melting temperatures and heat of fusion were determined directly from DSC thermographs.

Figure 3-8 is a plot showing the relationship between the glass transition, T_g, of PTHF oligomers and the molecular weight, M_n. As seen from the diagram, major changes in T_g occur at low molecular weights and small changes occur at high molecular weights. For M_n greater than 6000, T_g is relatively independent of M_n. At lower molecular weights, the T_g shows an obvious decrease reflecting the increase in polymer chain ends and free volume of the polymer chains. Empirically, Fox-Flory equation describes

reasonably well the molecular weight dependence of the glass transition temperature at not very low molecular weight:

$$T_g = T_{g,\infty} - K/M_n,$$

where K is a constant and M_n is the number average molecular weight of polymer.

However, experimentally the situation regarding molecular weight dependence of glass transition temperature is much more complicated. As shown in Figure 3-8 (b), the plot of T_g vs. $1/M_n$ can be divided into three straight line regions. The glass transition temperatures change according to the molecular weight or molecular morphology changes: from entangled coils to isolated coils to rod like molecules.

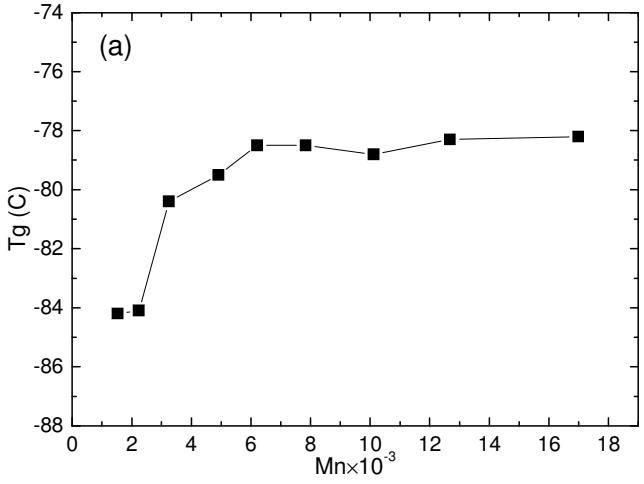

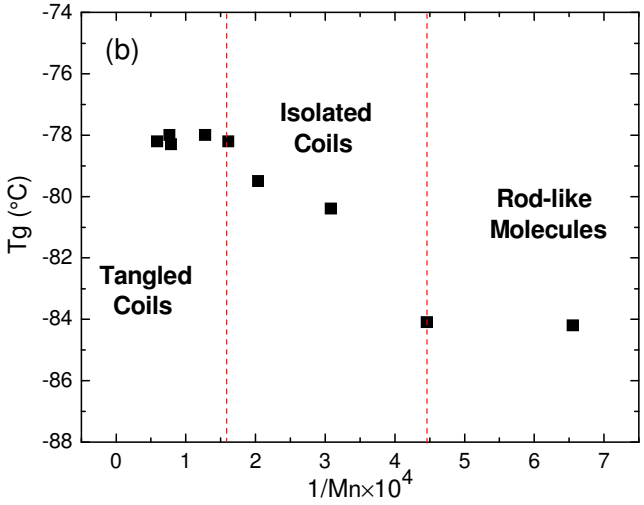

Figure 3-8 Dependence of T_g on molecular weight for PTHF oligomers. (a) T_g vs. M_n; (b) T_g vs. $1/M_n$

The melting of PTHF precursors was investigated at a rate of 10°C/min by DSC using nitrogen as inert gas. It was shown in all the DSC thermograms that the precursor polymers have very sharp endotherm peaks indicating the strong crystallization behavior. The melting point, T_m, is determined, for broad melting polymers, by the temperature at the maximum in the plot near this transition. Figure 3-9 shows the variations of the melting temperature as a function of M_n for precursor polymer crystallized at room temperature.

As results shown, oligomers of lower molecular weight have lower melting temperature than the long chain oligomers as expected. The melting temperature increases very fast with increasing the molecular weight in the relatively low Mn range (< 4000) and the melting temperature is relatively independent of the molecular weight when the Mn exceeds approximately 4000. This is due to the lower Mn oligomers crystallize into smaller crystallites compared with the one formed by long chain

oligomers. Concomitantly, the increase in melting temperature suggests larger crystals which result from a higher number of chains participating in the crystallization process. The equilibrium melting point for linear PTHF was estimated to be around 45°C. Also, it is shown in the DSC thermograms that as M_n decreases, the endotherm broadens implying a broader crystallite size distribution.

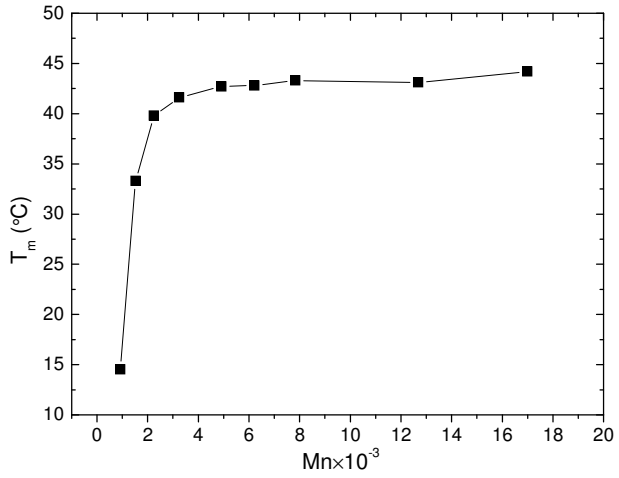

Figure 3-9 Dependence of melting temperature of PTHF precursors on M_n

3.2. Preparation of Model Networks through Endlinking

3.2.1. End-linking Process through Thiol-Ene Reaction

The end-linking process of preparing the model networks is based on thiol-ene reaction, which is the extension of the addition of thiol of olefins to form thioethers. The thiol-ene reaction exhibits several unique advantages such as being generally uninhibited by oxygen [131] and proceeding rapidly with a reasonable amount of initiator [132]. The radical thiol-ene addition reaction proceeds through 3 steps (Figure 3-10): the formation of a thiyl radical promoted by initiation, addition of the thiyl radical to a vinyl group, followed by radical transfer from the ensuing carbon radical to a thiol functional group.

These successive initiation/chain transfer reactions serve as the basis for the thiol-ene polymerization/cross-linking reaction [133].

Initiation	$In \rightarrow In\bullet$ $In\bullet + R\text{-}SH \rightarrow InH + RS\bullet$
Propagation	$RS\bullet + C{=}C \rightarrow RS\text{-}C\text{-}C\bullet$ $RS\text{-}C\text{-}C\bullet + C{=}C \rightarrow RS\text{-}C\text{-}C\text{-}C\text{-}C\bullet$
Chain transfer	$RS\text{-}C\text{-}C\bullet + R\text{-}SH \rightarrow RS\text{-}C\text{-}CH + RS\bullet$
Termination	$2\ RS\text{-}C\text{-}C\bullet \rightarrow RS\text{-}C\text{-}C\text{-}C\text{-}C\text{-}SR$ $\quad 2RS\bullet \rightarrow RS\text{-}SR$ $2\ RS\text{-}C\text{-}C\bullet + 2RS\bullet \rightarrow RS\text{-}C\text{-}C\text{-}SR$

Figure 3-10 Thiol-ene reaction scheme

The main character of above scheme is that the chain transfer reaction is much faster than the propagation and addition reactions dominating all other reactions. If a bi-functional thiol is used, the reaction is mainly a chain extending process:

$$(n+1)\ HS\text{-}R\text{-}SH + CH_2{=}CH\text{-}R'\text{-}CH{=}CH_2 \rightarrow HS\text{-}(R\text{-}SCH_2CH_2\text{-}R'\text{-}CH_2CH_2S)_n\text{-}R\text{-}SH$$

If a multi-functional mercaptan is involved in the reaction with di-vinyl monomer, a 3-dimensional network is formed. In addition, for dially oligomer the propagation reaction is actually very slow due to the resonance stabilization effect in the allyl group. Therefore the main composition of the final product is due to the crosslinking reaction of oligomer and multi-functional mercaptan through the chain transfer mechanism. In this study, α, ω-dially PTHF precursors were endlinked by a tetrafunctional crosslinker, pentaerythritol tetrakis 3-mercapto-propionate (PTMP) as shown in Figure 3-11.

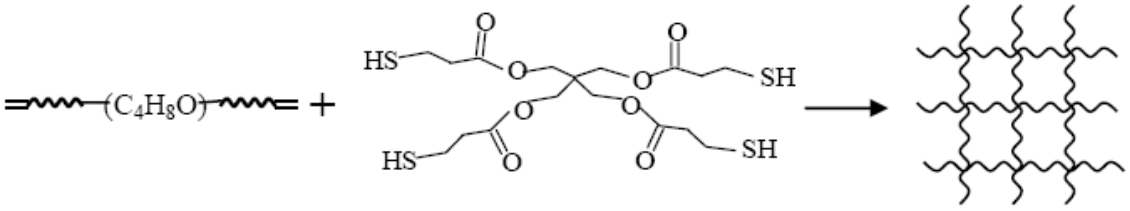

Figure 3-11 End-linking reaction of α, ω-dially PTHF with PTMP

Experimentally, PTHF precursors and stoichiometric amount of PTMP were first mixed and dissolved in benzene (~30 wt %), and 0.3 wt % AIBN was then added as an initiator. Pre-reaction was carried under N_2 at 65°C for about 1.5 hours before the mixture was poured into glass mold. The pre-reaction is necessary in preventing phase separation of crosslinker and oligomers. The glass mold containing pre-reacted mixture was put in a vacuum oven at 85°C and benzene was quickly removed by flushing and pumping N_2. The cure reaction was then continued under N_2 for another 48 hr at 85°C. The thol-ene reaction was confirmed by Raman as shown in Figure 3-12. The peaks at ~1646 cm^{-1} and ~3013 cm^{-1} disappeared indicating the consumption of allyl end group. The appearance of peak at ~ 1744 cm^{-1} is due to the introduction of -C=O from crosslinker PTMP.

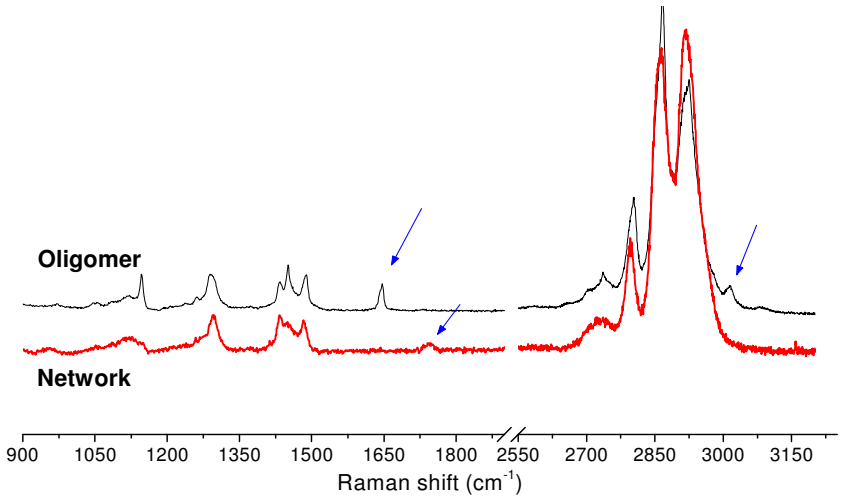

Figure 3-12 Raman spectra of PTHF oligomer and network

3.2.2. Unimodal and Bimodal Networks

Unimodal networks were prepared by directly end-linking one batch of mono-dispersed oligomer. Thus the chain length, M_c, between crosslinks in unimodal networks is exactly the molecular weight of the oligomer incorporated. Bimodal networks were

prepared by end-linking pre-determined amount of two batches of oligomers: short-chain oligomer and long-chain oligomer. The average chain length between crosslinks in bimodal networks was determined by the input mole fraction of short-chain (S) and long-chain (L) oligomers: $M_c = M_n$ (S) × mol% (S) + M_n (L) × mol% (L). The preparation processes of uni- and bimodal polymer networks are schematically shown in Figure 3-13.

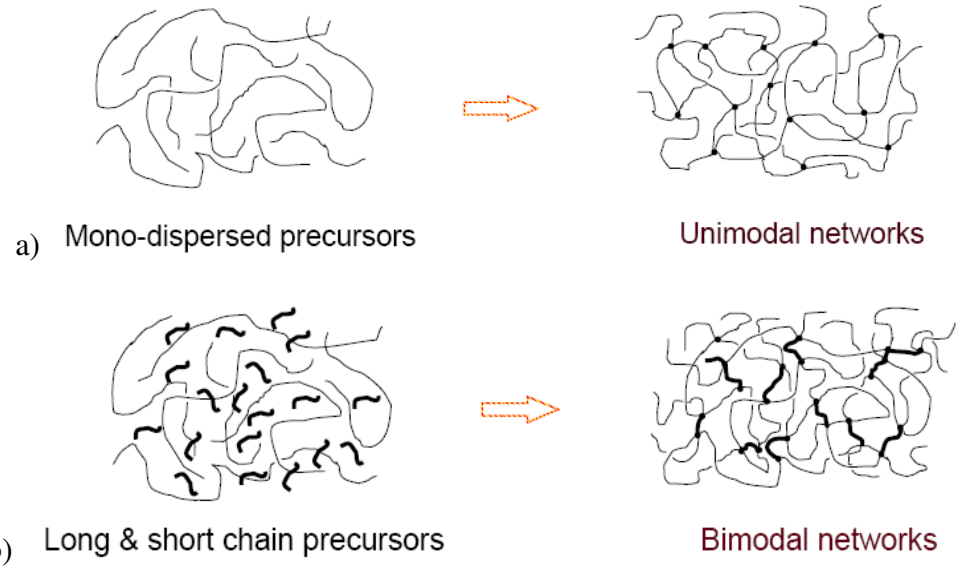

Figure 3-13 Schematic representation of preparation of (a) unimodal networks and (b) bimodal networks (bold lines - short chains)

In this work, unimodal and bimodal PTHF networks with varying crosslink densities (M_c) were prepared. The feed composition is given in Table 3-2.

Table 3-2 Composition of unimodal and bimodal networks

	Sample	***M_n (S)***	***M_n (L)***	***mol ratio (S)***	***mol ratio (L)***	***M_c^****
Unimodal	**U-5**	942	-	1.00	-	942
	U-11	1526	-	1.00	-	1526
	U-8	-	2146	-	1.00	2146
	U-3	-	3246	-	1.00	3246
	U-2	-	4908	-	1.00	4908
	U-4	-	6215	-	1.00	6215

	U-7	-	7835	-	1.00	7835
	U-6	-	11546	-	1.00	11546
	U-12	-	17669	-	1.00	17669
Bimodal	**B-12**	917	13051	0.95	0.05	1526
	B-7	917	13051	0.90	0.10	2130
	B-5	917	13051	0.80	0.20	3270
	B-8	917	13051	0.67	0.33	4900
	B-14	607	17669	0.75	0.25	4900
	B-16	917	6068	0.23	0.77	4900
	B-1	3246	13051	0.82	0.18	4900
	B-18	917	13051	0.56	0.44	6215
	B-6	917	13051	0.48	0.52	7208
	B-9	3246	13051	0.60	0.40	7208
	B-11	917	13051	0.30	0.70	9411
	B-13	917	13051	0.17	0.83	11050

Corresponding deuterated bimodal networks were also prepared by crosslinking deuterated short chains with hydrogenated long chains or deuterated long chains with hydrogenated short chains. The composition is summarized in Table 3-3.

Table 3-3 Composition of selectively deuterated unimodal and bimodal networks

Sample*	M_n ***(S)***	M_n ***(L)***	***mol ratio (S)***	***mol ratio (L)***	M_c
U-**L**	-	**12800**	-	1.00	12800
B**dL-**2	853	**12800**	0.82	0.18	3000
B**dS-**2	**925**	17782	0.88	0.12	3000
B**dL-**1	853	**12800**	0.65	0.35	5000
B**dS-**1	**925**	17782	0.76	0.24	5000
B**dL-**3	853	**12800**	0.49	0.51	7000
B**dS-**3	**925**	17782	0.64	0.36	7000
B**dS-**4	**925**	11546	0.62	0.38	5000

* **dL** – long oligomer chains are deuterated; **dS** – short oligomer chains are deuterated.

3.2.3. Multi-functional Clusters and Clustered Model Networks

Synthesis of clustered networks involved two steps: firstly, the very short chain oligomers were pre-reacted for a certain period of "clustering time" with controlling amount of PTMP to form the multi-functional "clusters". The size of the clusters was controlled through clustering time and stoichiometric ratio; secondly, the long chain precursors mixed with stoichiometric amount of PTMP were added into the pre-reacted multifunctional clusters mixture. Then the crosslinking continued between the multifunctional clusters and the long chain oligomer to form the networks. The intercrosslink chain length (M_c) of clustered networks is determined the same way as in bimodal networks: $M_c = M_n\,(S) \times \text{mol\%}\,(S) + M_n\,(L) \times \text{mol\%}\,(L)$. Selectively deuterated clustered networks were also prepared in the same manner except that the clusters or the long chains were deuterated. The schematic representation of preparation of clustered networks is shown in Figure 3-14.

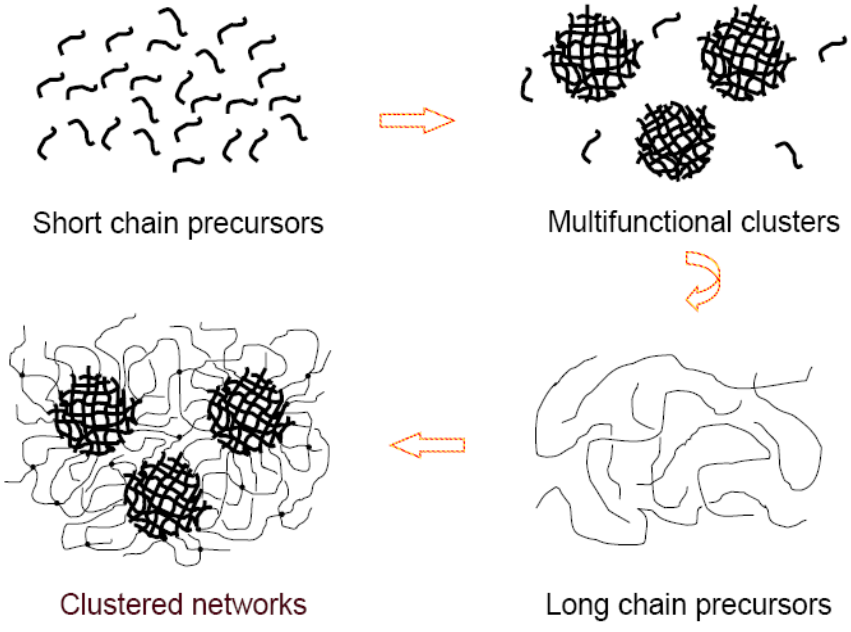

Figure 3-14 Scheme of preparation of clustered networks (bold lines - short chains)

The multifunctional structure of clusters was characterized by NMR and the cluster sizes were characterized by GPC. A NMR spectrum for cluster is presented in Figure 3-15. The structure of crosslinker PTMP is $(HSCH_2CH_2CO_2CH_2)_4C$. Compared with NMR spectrum of oligomer (Figure 3-4), the new peaks in the clusters can be recognized as: the thiol proton presents at ~ 1.6 ppm overlapping with the backbone protons; the twin peaks at ~ 2.6-2.8 ppm are due to CH_2 protons bonded with thiol group; the peak at ~ 4.2 ppm is due to CH_2 protons bonded with core carbon atom.

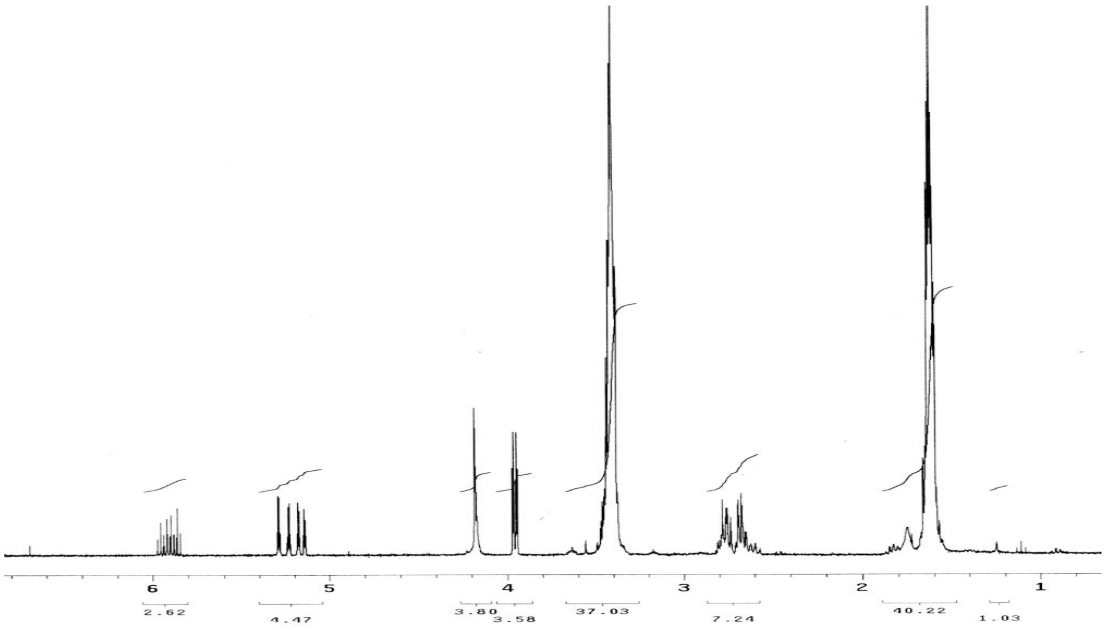

Figure 3-15 NMR spectrum of multifunctional PTHF clusters

The cluster size and size distribution are characterized using GPC. The retention time curves of clusters formed at varying clustering time are shown in Figure 3-16. As shown, longer clustering time gives large cluster size and wider size distribution, resulting in different degree of inhomogeneity. Conceptually, smaller cluster size has narrower size distribution, thus the resultant network has lower inhomogeneity.

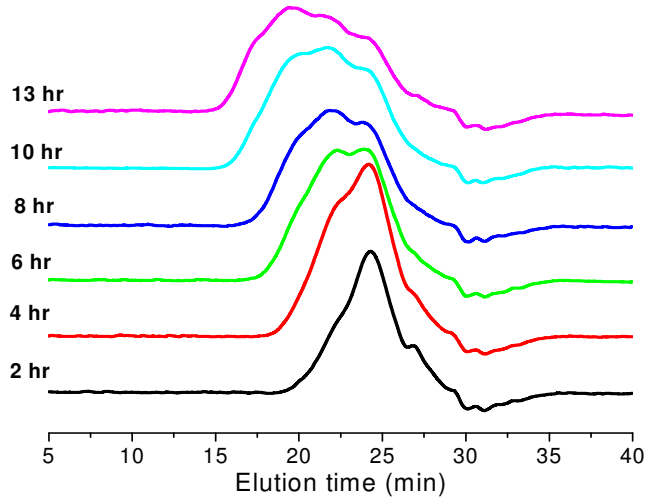

Figure 3-16 GPC retention curves of clusters at varying clustering time (starting oligomer: M_n = 917, PDI = 1.05, stoichiometric ratio (PTMP/oligomer) = 0.8)

The compositions of clustered networks with various sizes and size distribution of the multifunctional clusters were summarized in Table 3-4. Clustered networks with 3 different crosslink densities were prepared, i.e., Mc=3270, 4908, 7000.

Table 3-4 Size and size distribution of clusters and composition of corresponding clustered networks

Sample	*M_n (S)*	*M_n (L)*	*mol ratio (S)*	*mol ratio (L)*	*Clustering time (hr)*	*Cluster size**	*Cluster PDI**	*M_c*
CT-5	917	12684	0.80	0.20	2	2807	1.52	3270
CT-3	917	12684	0.80	0.20	4	3292	1.76	3270
CT-17	917	12684	0.80	0.20	6	3996	2.18	3270
CT-18	917	12684	0.80	0.20	8	4636	2.70	3270
CT-9	917	13051	0.80	0.20	10	5572	3.73	3355
CT-13	917	13051	0.80	0.20	13	6428	4.38	3355
CT-7	917	12684	0.80	0.20	18	-	-	3270
CT-2	917	12684	0.66	0.34	2	2807	1.52	4908
CT-6	917	12684	0.66	0.34	3	-	-	4908
CT-14	917	12684	0.66	0.34	4	3292	1.76	4908
CT-15	942	13051	0.66	0.34	6	3996	2.18	4908
CT-16	942	13051	0.66	0.34	8	4636	2.70	4908
CT-12	942	13051	0.66	0.34	18	-	-	4908

Selectively deuterated clustered networks were also prepared in the same manner. Clustered networks with deuterated short chains or deuterated long chains have been prepared as summarized in Table 3-5.

Table 3-5 Composition of selectively deuterated clustered networks

*Sample**	M_n *(S)*	M_n *(L)*	*mol ratio (S)*	*mol ratio (L)*	*Clustering time (hr)*	M_c
CT**dS-**3-**S**	925	17782	0.88	0.12	3	3000
CT**dS-**3-**M**	925	17782	0.88	0.12	6	3000
CT**dL-**3-**S**	853	12800	0.82	0.18	3	3000
CT**dL-**3-**M**	853	12800	0.82	0.18	6	3000
CT**dS-**1-**S**	925	17782	0.76	0.24	3	5000
CT**dS-**1-**M**	925	17782	0.76	0.24	6	5000
CT**dL-**1-**S**	853	12800	0.65	0.35	3	5000
CT**dL-**1-**M**	853	12800	0.65	0.35	6	5000
CT**dS-**2-**S**	925	17782	0.64	0.36	3	7000
CT**dS-**2-**M**	925	17782	0.64	0.36	6	7000
CT**dL-**2-**S**	853	12800	0.49	0.51	3	7000
CT**dL-**2- **M**	853	12800	0.49	0.51	6	7000

* CT**dS** – short chains are deuterated; CT**dL** – long chains are deuterated
** **S** – small size clusters (3 hr); **M** – medium size clusters (6 hr)

The selectively labeled clustered networks were prepared at three crosslink density levels: M_c = 3000, 5000 and 7000. For each crosslink density level, networks with deuterated short chains (or clusters) were prepared as well as the corresponding networks with deuterated long chains. There are some M_n differences in precursor polymers (deuterated long chain 12800, hydrogenated long chain 17782), but the averaged M_c was always kept the same to assure the validity of later investigation on some physical properties.

CHAPTER 4

THERMAL CHARACTERISTICS OF MODEL PTHF NETWORKS

As a routine technique, differential scanning calorimetry (DSC) measurements were carried out on a Seiko Instrument Model DMS210. All networks were brought to equilibrium at room temperature. Samples of 7 ~ 12 mg were crimped in aluminum DSC pans. A consistent thermal history was ensured for each sample by applying exactly the same heating-cooling conditions: The DSC cell containing the sample was first quickly cooled down from room temperature to -120°C at 20°C/min and hold for 3 min before heating to 80°C at a rate of 10°C/min. Two heating-cooling cycles were done for each sample. The thermal characteristics like glass transition, melting, and crystallization of model PTHF networks were investigated as a function of crosslink density (M_c) and inhomogeneity associated with crosslink density distribution. For better understanding the crosslink density and inhomogeneity effect, thermal characteristics of uncrosslinked linear PTHF prepolymers of varying M_n are shown in Figure 4-1 for comparison.

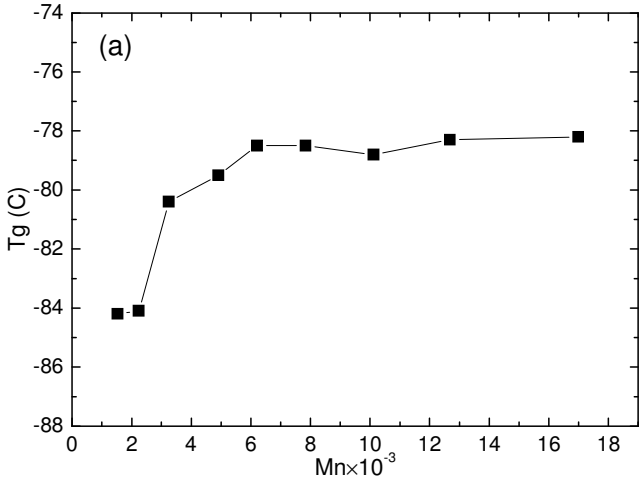

(a)

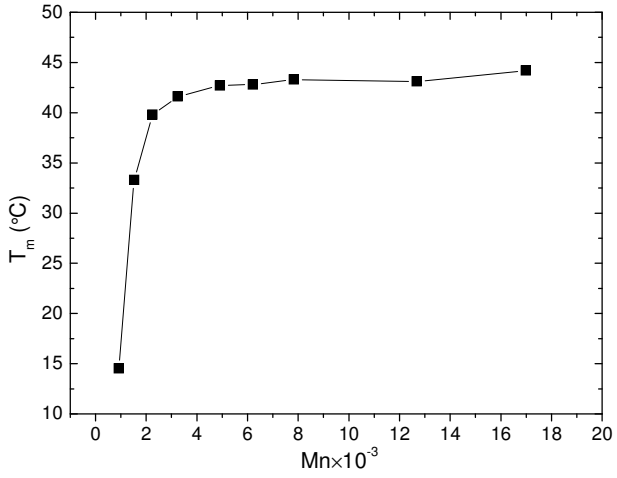

(b)

Figure 4-1 Thermal characteristics of α, ω-dially PTHF precursor polymers: (a) glass transition; (b) melting temperature

4.1. Crosslink Density Effect

Crosslink density is represented in this work by the average inter-crosslink molecular weight, *i.e.*, M_c, in the networks. Lower value of M_c gives higher crosslink density (per unit volume) in the model networks.

4.1.1. Glass Transition Temperature (T_g)

Figure 4-2 depicts the effect of crosslink density on glass transition temperature for model networks compared with those of precursors that formed the corresponding elastomers. Since the average molecular weight M_c in the unimodal networks is exactly same as the M_n of the precursor polymers by design, the only difference between them is the presence of crosslinks. Intuitively one could arrive at the conclusion that chemical cross-links increases T_g due to the additional restriction on molecular motion that reduces the segmental mobility.

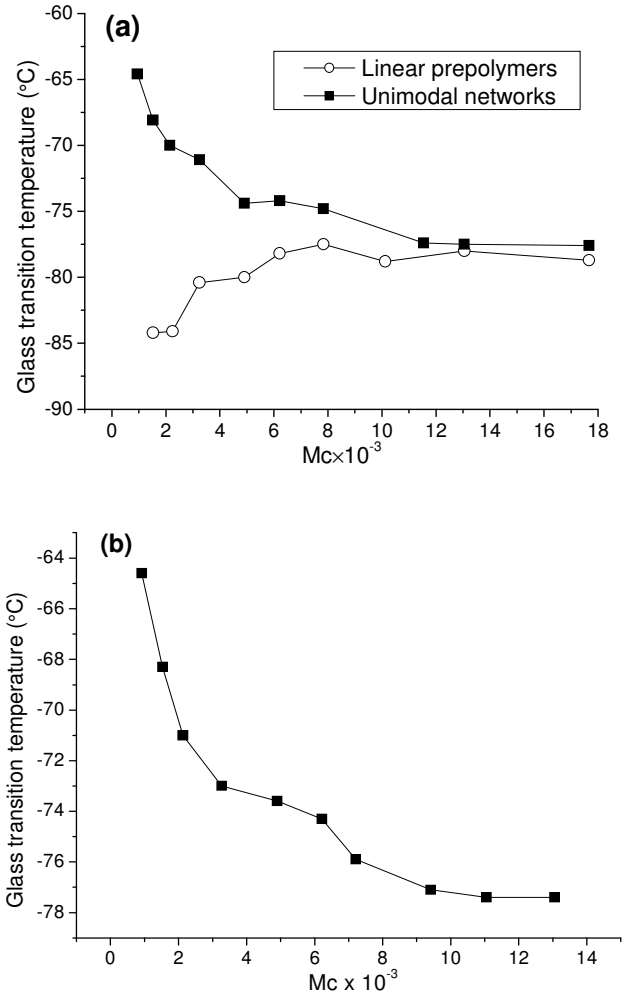

Figure 4-2 Effect of crosslink density (represented in M_c) on T_g: (a) linear precursors and unimodal networks; (b) bimodal networks (for composition details see Table 3-2)

As results shows, for given M_c, networks have higher T_g than the precursor liner polymers. Particularly, at high cross-link densities (for unimodal networks, $M_c < 3000$; for bimodal networks, short chain ratio > 80% mol), T_g rises even faster with increasing crosslink density indicating a severe restraint from crosslink junctions. As seen, the end-linking increases T_g by about 20°C for network of highest crosslink density compared with corresponding precursor polymer. T_g reaches the highest value of -64°C for the unimodal networks with shortest inter-crosslink chain length ($M_c = 942$). Similar finding

was reported for end-linked polyisobutylene [134] that T_g increases with increase in crosslink density or decrease in M_c. Theoretically, it was demonstrated by Charlesworth [135] that increasing the crosslink density would result in the increase of T_g for networks formed from α, ω-alkyldiamines.

However, the difference in T_g between networks and precursors decreases with increasing M_c. Finally there is only a subtle difference between T_g of PTHF polymers before and after crosslinking for high molecular weight chains (> 13,000), which indicate that as the segment between crosslinks is long enough, the effect of restriction due to crosslinks becomes less important, because for longer chains entanglements naturally occurring between the chains becomes the determining factor for segmental mobility.

4.1.2. Melting Temperature (T_m)

The appearance of melting peaks in DSC thermograms clearly indicates that PTHF model networks were capable of crystallization even in the presence of crosslinks although the crystallization was suppressed due to the crosslinking. The rate of crystallization at room temperature was of the order of hours and days depending on the segment length between crosslinks. Figure 4-3 shows the melting temperature of modal networks compared with precursor polymers as a function of crosslink density.

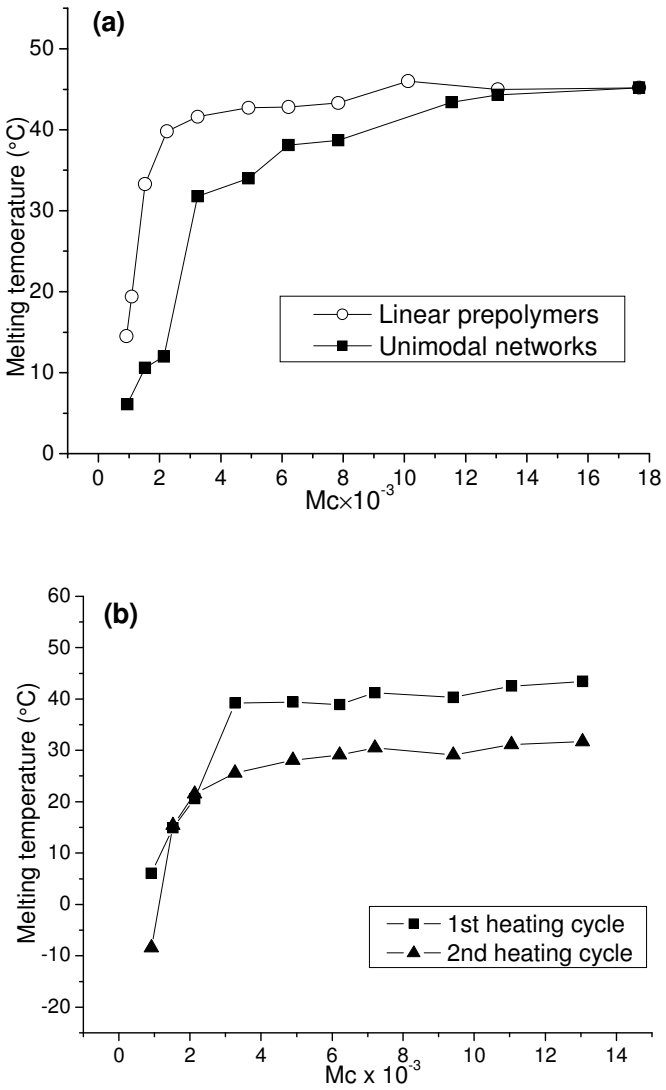

Figure 4-3 Effect of crosslink density on melting temperature: (a) linear precursors and unimodal networks; (b) bimodal networks (for composition details see Table 3-2)

From the results obtained (Figure 4-3 a), $T_{m,\infty}$ of α, ω-diallyl PTHF was roughly estimated to be 47°C, which was quite close to the value (321 K) reported by Trick et al [136] for hydroxyl-terminated linear PTHF. As can be seen, the melting temperature decreases for the networks compared with precursor polymers, indicating the limitation of crystallization due to the introduction of crosslinks. The reason is straightforward that upon crystallization, in addition to their shorter segment length of crystallizable units,

network chains can induce lower entropy configurations in the amorphous phase compared to that in the crystalline state. These effects hinder crystallization resulting in smaller and less perfect crystals [137] and thus lower T_m's of crosslinked networks compared to the equilibrium T_m's of linear precursors are expected. The melting points for both unimodal and bimodal networks systematically increases with M_c indicating a decreasing edge-free energy in the crystals [138]. Therefore crosslinking process reduces both the extent of crystallization and the stability (or perfection) of the crystalline phase. Similarly, it was also found that the difference in melting temperatures between high molecular weight precursors and networks with long inter-crosslink chain length is very small just like the pattern observed with glass transition behavior. Again, the entanglements, forming physical crosslinks, become the critical limiting factor for transition properties than the chemical crosslinks.

4.1.3. Heat of Fusion (ΔH_m)

Furthermore, the effect of crosslink density on the heat of fusion (ΔH_m) was also investigated for networks as shown in Figure 4-4. Comparison of networks and precursors clearly shows that the enthalpy of fusion, ΔH_m, is greatly suppressed by introduction of crosslinks indicating a much smaller degree of crystallinity (~ 60 wt% less). The heat of fusion for both precursors and networks follows a general trend that it increases with increasing molecular weight or the inter-crosslink chain length or decreases with the crosslink density. And the rate of increase in ΔH_m becomes smaller for M_n or M_c greater than ~3000. This trend is in accordance with the dependence of melting temperature on M_c, indicating that despite the presence of crosslinks, longer chains with the freedom to assume more conformations are more likely be incorporated into

crystalline regions and thus result in higher crystallinity. Therefore, the initiation of crystallization (or melting) is sensitive to the M_n or M_c.

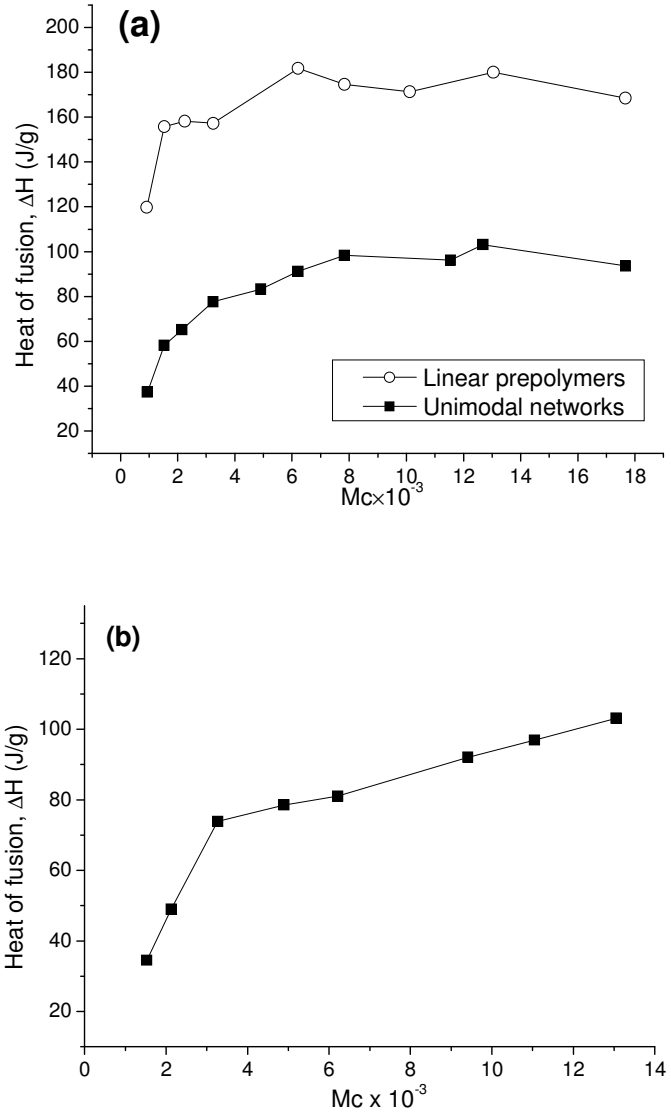

Figure 4-4 Effect of crosslink density on heat of fusion, ΔH_m: (a) linear precursors and unimodal networks; (b) bimodal networks (for composition details see Table 3-2)

4.2. Inhomogeneity Effect

In this section, the effect of inhomogeneity, resulting from inhomogeneous distribution in crosslink density, on thermal characteristics was investigated. By

definition, inhomogeneity is non-uniform spatial distribution of crosslinks in networks, which is non-relaxing frozen concentration fluctuation. In this work, three varieties of the inhomogeneities of crosslink density distribution were studied: 1) unimodal and bimodal networks with same average crosslink density (composition details see Table 3-2); 2) bimodal networks with same M_c but different size ratio of long and short chains (sample B-8, B-14, B-16, B-1 in Table 3-2); 3) clustered networks with same average M_c, but with different cluster size and size distribution (composition details see Table 3-4). As mentioned earlier, unimodal networks have close to mono-dispersed chain length distribution between crosslinks, while a bimodal distribution of inter-crosslink chain length exists in bimodal networks. Thus the bimodal networks are more heterogeneous in crosslink sites distribution than the unimodal ones for the same average M_c, at length scales larger than the length of short chains (but less than the length of long chains). A novel extension of controlling the crosslink density distribution is to prepare the networks with "clustered" topology, in which highly crosslinked clusters are linked to and embedded in long chain matrix which has lower crosslink density. Networks formed by crosslinking multifunctional clusters are considered to have more heterogeneous chain length distribution, i.e., higher degree of inhomogeneity in crosslink density distribution. Thus the inhomogeneity level of the networks is considered to be in the order of: unimodal < bimodal < clustered. This difference in network architecture is expected to influence the macroscopic properties like thermal characteristics.

4.2.1. Glass Transition Temperature (T_g)

As shown in Figure 4-5 (a), regardless of inhomogeneity of the chain length distribution, glass transition for unimodal and bimodal networks follows the same trend:

T_g increases with decreasing M_c. However, the inhomogeneity resulting from chain length distribution in bimodal networks exerted only a trivial influence on the glass transition temperature. For the same crosslink density the values of T_g of unimodal and bimodal networks are close to each other.

Since the contribution from topological aspect is of considerable theoretical and technological interest, another set of comparison was made using bimodal networks with various size ratios of short and long chains to further explore the effect of heterogeneous distribution of inter-crosslink chain length on the thermal behavior. The composition and size ratios are summarized in Table 4-1. The inhomogeneity of crosslink density distribution is represented here by the size ratio M_n (L) / M_n (S), i.e., the ratio of M_n for long chain sequences to M_n for short chain segments. The larger the size ratio is, the more heterogeneous the networks assume in crosslink density distribution.

Table 4-1 Composition of bimodal networks with different size ratios (same M_c)

Sample	*M_n (S)*	*M_n (L)*	*mol ratio (S)*	*mol ratio (L)*	*Size ratio***	*M_c*
B-14	607	17669	0.75	0.25	**29.1**	4900
B-8	917	13051	0.67	0.33	**14.2**	4900
B-16	917	6068	0.23	0.77	**6.6**	4900
B-1	3246	13051	0.82	0.18	**4.0**	4900

* Size ratio = M_n (L) / M_n (S)

As shown in Figure 4-5 (b), the inhomogeneity resulting from the different size ratio (M_n (L) / M_n (S)) does not exert an obvious influence on the T_g, which is consistent with the previous finding that unimodal and bimodal networks have similar T_g values given the same average M_c (Figure 4-5 a). Thus the glass transition behavior seems to depend solely on the average inter-crosslink chain length (M_c) in the networks.

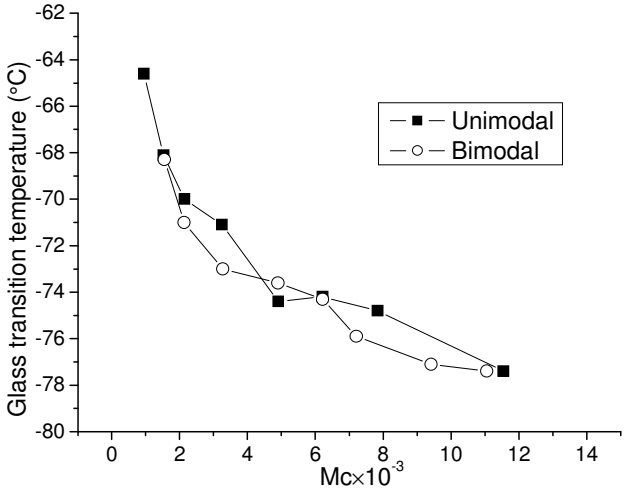
Glass transition temperature (°C)
-62
-64
-66
-68
-70
-72
-74
-76
-78
-80
0
2
4
6
8
10
12
14
Mc×10-3
Unimodal
Bimodal

a)

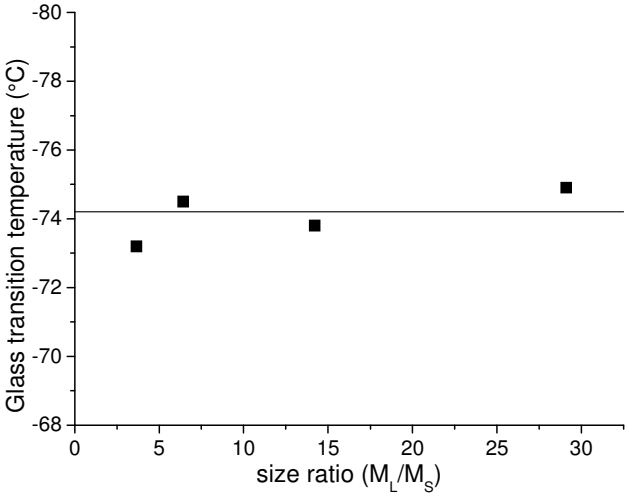
Glass transition temperature (°C)
-80
-78
-76
-74
-72
-70
-68
0
5
10
15
20
25
30
size ratio (ML/MS)

b)

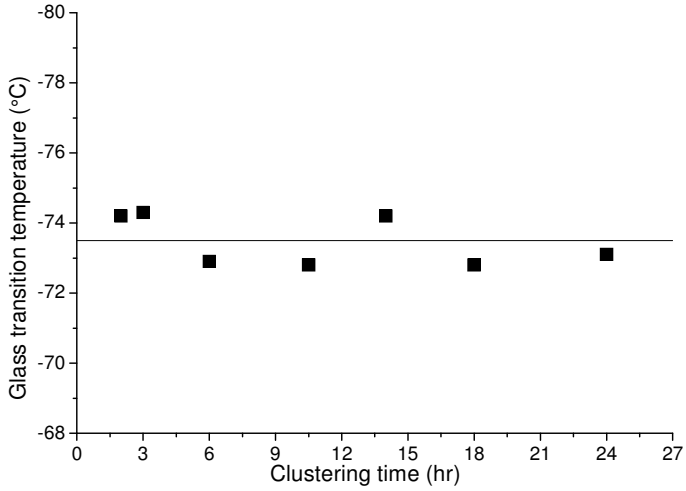
Glass transition temperature (°C)
-80
-78
-76
-74
-72
-70
-68
0
3
6
9
12
15
18
21
24
27
Clustering time (hr)

c)

Figure 4-5 Effect of inhomogeneity on T_g: a) same M_c but different chain length distribution; b) same M_c but different M_L/M_S ratio; c) same M_c but different cluster size (composition details see Table 3-2, Table 3-4 and Table 4-1)

As for the networks with clustered topology, the multifunctional cluster size was controlled by varying the "clustering" time. Longer "clustering" time gives large cluster size and wider cluster size distribution, resulting in different degree of inhomogeneity. Similarly, the difference in the inhomogeneity of crosslink density distribution has little influence on the glass transition as shown in Figure 4-5 (c). Regardless of clustering time, glass transition temperatures for clustered networks were found to be between -72.8℃ ~ -74.3℃ and no specific trend was found as a function of cluster size and distribution. This result is in accordance with the previous observations in uni- and bi-modal networks and bimodal networks with different size ratios. Therefore it seems to indicate that the inhomogeneity in crosslink density distribution has negligible effects on the glass transition behavior of networks and T_g seems to be dependant solely on the average inter-crosslink chain length (M_c) in the networks.

4.2.2. Melting Temperature (T_m)

Evidently, the inhomogeneity in crosslink density distribution could influence the crystallization and melting behavior in principle since it governs the crystallizable sequence of chain length. The investigation of the dependence of melting temperature on inhomogeneity was also carried out at three different inhomogeneity levels as shown in Figure 4-6 (a-c).

It can be seen from Figure 4-6 (a) that the melting temperature difference between unimodal and bimodal networks for the same average M_c does reflect the effect of the network architecture and inhomogeneity of crosslink distribution on T_m. For lower M_c,

the melting point of bimodal networks is about 8 °C higher than that of unimodal networks given the same average chain length between crosslinks; this likely reflects the presence of long sequence (M_c = 13051) of PTHF precursors in the bimodal networks, which is possible to be incorporated into crystalline phase more easily resulting in better crystals. When average chain length exceeds 6000, however, the unimodal networks, lacking the short sequences (M_n = 917), are probably able to form a more stable crystalline phase and thus the melting point becomes closer to that of bimodal networks of the same average M_c. For even longer chain length between crosslinks, the melting temperatures of unimodal networks are very close to the bimodal ones. This seems to indicate that for long enough inter-crosslink chain length with the same average crosslink density, inhomogeneous distribution of crosslinks has only a small effect on the crystallizability of molecular chains. The similar trend of the inhomogeneity effect on melting behavior was also found in bimodal networks with different chain size ratios and clustered networks with varying cluster sizes as shown in Figure 4-6 (b) and (c), respectively. These observations seem to indicate that inhomogeneities in crosslink density in networks increase the melting temperature due to the heterogeneous inter-crosslink chain length distribution.

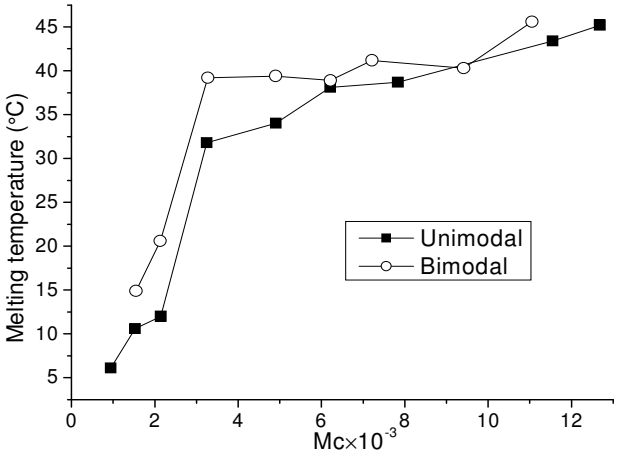

a)

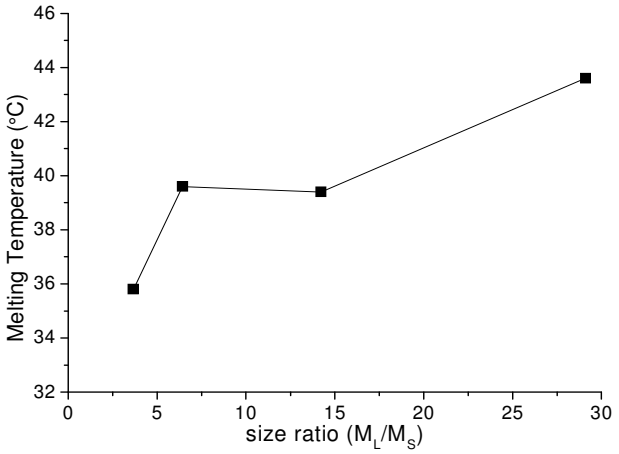

b)

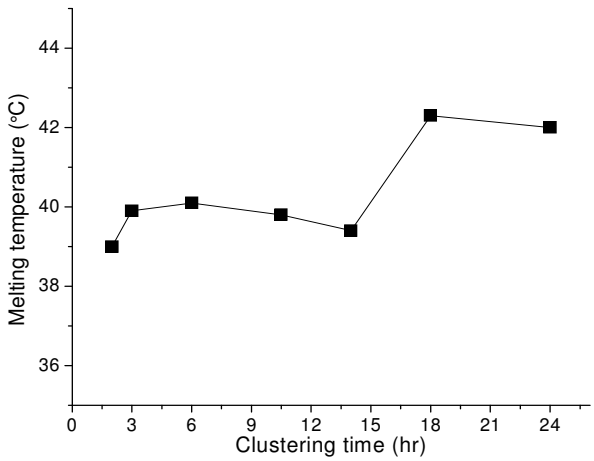

c)

Figure 4-6 Effect of inhomogeneity on T_m: (a) same M_c but different chain length distribution; b) same M_c but different M_L/M_S ratio; c) same M_c but different cluster size (composition details see Table 3-2,Table 3-4 and Table 4-1)

It is obvious that the melting temperature of all PTHF networks is lower than the corresponding uncrosslinked PTHF. This melting temperature depression results from the facts that the crosslink junctions themselves are not crystallizable and they would further prevent the topologically neighboring chain segments from being incorporated into crystalline phase. It was shown by Mandelken [137] and Flory [139] that the melting temperature depression caused by crosslink could be quantitatively determined by the following relationship:

$$\frac{1}{T_m} - \frac{1}{T_{m,\infty}} = -\frac{R}{H_f}\ln(1-f) \qquad \text{(Eq. 4-1)}$$

in which R is gas constant, H_f the enthalpy of fusion, and $T_{m,\infty}$ the equilibrium melting point for uncrosslinked PTHF, and f is the fraction of chain units that are crosslinked which is given by $f = m/2M_c$ with m being the monomer molecular weight. However, it was pointed out that [139] this suppression is less for endlinking model networks. A parameter ξ was then introduced to better account for the number of units precluded from crystallization per crosslink site (ξ actually denotes the number of units per crosslink prevented from crystallization) [140] as follows:

$$\frac{1}{T_m} - \frac{1}{T_{m,\infty}} = -\frac{R}{H_f}\ln(1-\xi f) \qquad \text{(Eq. 4-2)}$$

For PTHF model network system, taking ξ as an adjustable parameter, $T_{m,\infty}$ =321 K (estimated from T_m measurements of linear PTHF oligomers) and H_f = 12.6 KJ/mol [141], Equation 4-2 was applied to fit the melting temperature data for unimodal and bimodal networks. The fitting results are shown in Figure 4-7. As shown, theoretical values calculated using Equation 4-2 agree satisfactorily with experimental data using the best fit value of ξ = 25 for unimodal networks and ξ = 20 for bimodal networks. This

would suggest that more than 6 (25/4) adjoining units in unimodal networks are constrained from crystallization compared to 5 (20/4) units in bimodal networks when a tetrafunctional crosslinker used. Also this seems to suggest that for the same average crosslink density, bimodal chain length distribution between crosslinks weakens the confinement effects of crosslinks on crystallization to some extent. This is presumably because the existence of long chain segments in the bimodal networks dilutes the confinement effects.

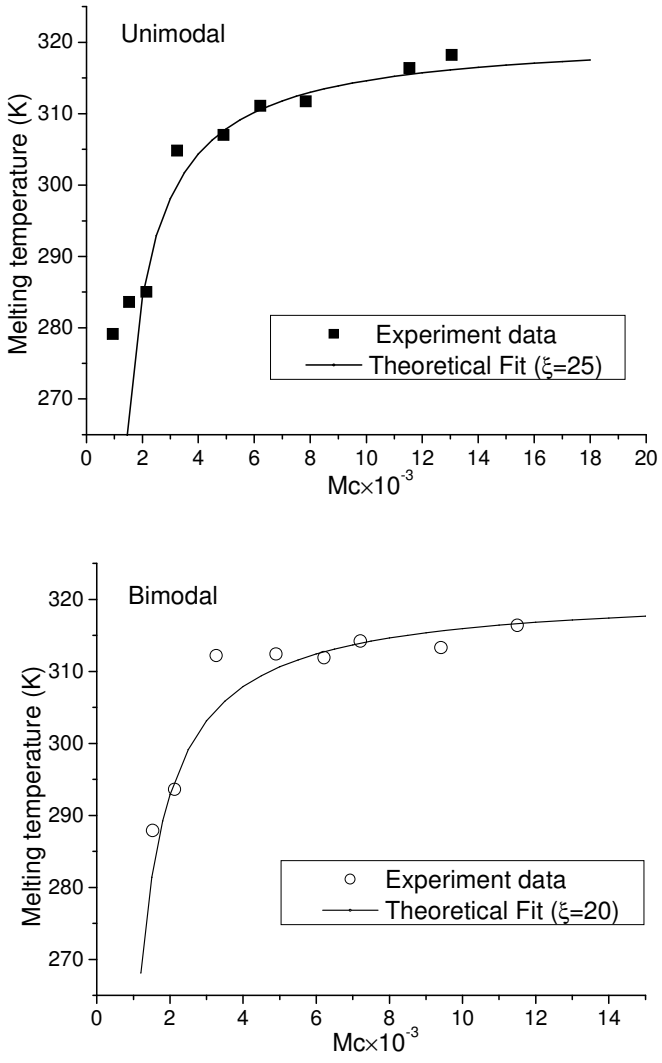

Figure 4-7 Theoretical fit for melting temperature depression for unimodal and bimodal networks (best fit value: ξ=25 for unimodal networks and ξ=20 for bimodal networks)

4.2.3. Heat of Fusion (ΔH_m)

For degree of crystallinity (presented by ΔH_m) as shown in Figure 4-8 (a-c), the same trend was found as that in the comparison between uni- and bi-modal networks of same average crosslink density. Given the same average M_c, more heterogeneous network architecture gives lower heat of fusion. ΔH_m for bimodal networks is lower than that of unimodal ones (Figure 4-8 a); and bimodal networks with larger size ratios have lower ΔH_m than those with small $M_n(L)/M_n(S)$ ratios (Figure 4-8 b). As a general trend, these observations suggest that more inhomogeneous distribution of inter-crosslink chain length lowers the crystallinity and stability of crystalline phase.

It is noticed that (Figure 4-8 c) given the same average M_c, the clustered networks have higher ΔH_m than both the unimodal and bimodal networks, which indicates that clustered networks have higher crystallinity than the other two types of networks. In clustered networks, there are two regions: highly crosslinked regions - "clusters" formed by pre-crosslinking of very short chains and a crosslinked region of very long chains associated with lower crosslink density. Due to this special topology, the very long chains have more mobility to be incorporated into crystals without being interfered much by the short chains, which are considered to be less crystallizable. In addition, ΔH_m for clustered networks decreases with increasing the cluster size (as represented by the "clustering time"), which indicates that increasing the cluster size lowers the crystallizability. More structural defects (especially cross-linking with the matrix of long chains at the cluster interface) are introduced into the networks that impedes crystallization.

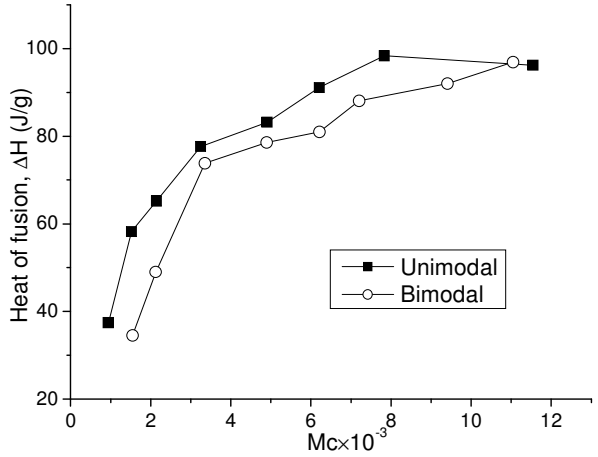

a)

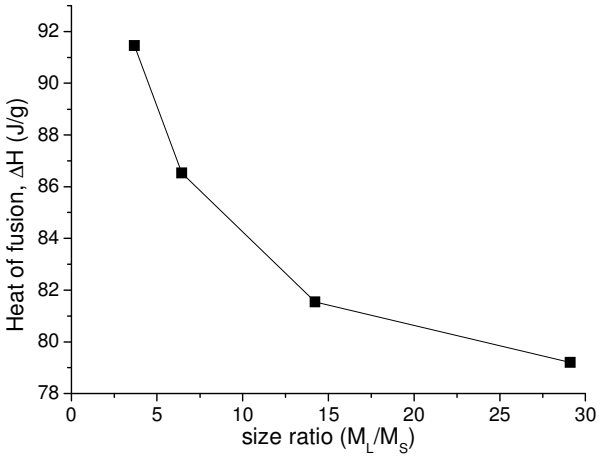

b)

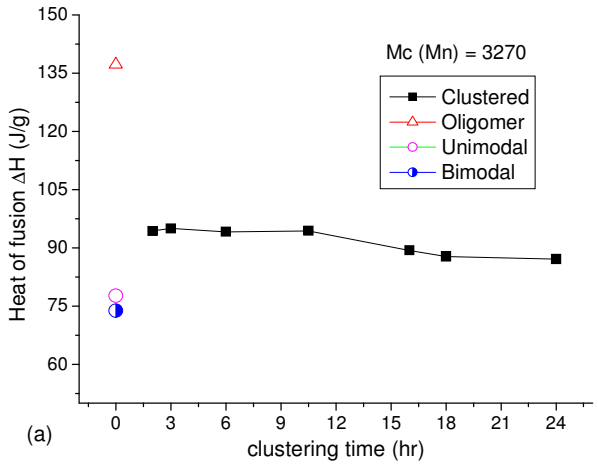

c)

Figure 4-8 Effect of inhomogeneity on ΔH_m: (a) same M_c but different chain length distribution; b) same M_c but different M_L/M_S ratio; c) same M_c but different cluster size (composition details see Table 3-2,Table 3-4 and Table 4-1)

CHAPTER 5

NANO-SCALE SOFT CONFINEMENT OF MODEL PTHF NETWORKS ON SOLVENT FREEZING BEHAVIOR

5.1. Background and Theory

It is well known that solvent confined in a capillary or in a small confinement of silica and other inorganic porous materials exhibits reduction in freezing point compared to its freezing point in its bulk state. The reduction is found out to be closely related to the pore size and size distribution in the materials. This thermo-porosimetry technique has been used to calculate the distribution of pore size in rigid porous materials, like glass beads, concrete etc. Same phenomenon has also been observed in soft confinement systems of water in polymer gels, like poly(acrylic acid)/poly(vinyl alcohol) gels [142] and poly(acryl amide) gels [143, 144]. And it has been further demonstrated for many organic solvents in polymer network systems, such as benzene-swollen vulcanizates [145]. For the usual dilute solution, the phenomenon of freezing point depression is a colligative effect. However, the abnormally large depression of freezing point (ΔT_f) of a monomeric solvent in a swollen network (gel) could not be fully explained by colligative effect alone due to the facts that: 1) magnitude of ΔT_f increases with increasing crosslink density for constant polymer-in-gel volume; and 2) ΔT_f is independent of molecular weight for non-crosslinked linear polymer solution. Kuhn and Majer [142] ascribed this abnormal depression to the limited solvent crystal size in the gel, resulting from the confinement of a mesh formed by the segments of the polymer networks. Based on the assumption that a crystal formed in the gel has a higher vapor pressure than that of the

free solvent crystal, they derived a relationship between the freezing point depression, ΔT_f, and the dimension of the solvent crystal, D:

$$\Delta T_f = \frac{zT_{sl}^0 \sigma_{sl}}{L_0 D \rho} \qquad \text{(Eq. 5-1)}$$

where z is the structure factor of the solvent crystal (cubic shapes: $z = 4$; long cylindrical capillaries: $z = 2$), T^0_{sl} is the normal freezing point of pure solvent, σ_{sl} is the interfacial tension between the crystal and its melt, ρ is the density of solvent crystal and L_0 is the specific melting heat. As for the benzene-swollen system, taking solvent parameters for benzene: $z = 4$, $T^0_{sl} = 278.65$ K, $\sigma_{sl} = 4.0\times10^3$ J/m^2, ρ =1.01 g/cm^3 and $L_0 = 126.1$ J/g, Eq. 5-1 can be further simplified to be:

$$\Delta T_f = -\frac{350\ \text{Å}}{D} \qquad \text{(Eq. 5-2)}$$

Here D (in Å) refers to the "characteristic" dimension of a confined solvent crystal. It is logical to assume that D is equivalent or at least very close to the segment length between crosslinks in the swollen gel since the inter-crosslink segments form the circumference of the "pores" resulting in the limited growth of solvent crystals. Thus many attempts have been made to estimate the degree of crosslinking and the distance between the junction points in networks according to the degree of freezing point depression. In addition, it was speculated that the melting point depression as well was probably associated with the network architecture to some extent. Very interesting observations were made in the past related to changes in freezing temperature. Oikawa et al [146, 147] observed that solvent crystal size in degraded rubbers was always lower than that for non-degraded samples even if they had similar chain densities. It was speculated to be due to the difference in their network structures, i.e., the dangling chains resulting from degradation are so

flexible that they may disturb the crystal lattice of benzene. Grobler et al [148] found that freezing point depression of cyclohexane in peroxide-cured polyisoprene was lower than those of γ-irradiated polyisoprene for the same swelling degree. These deviations were ascribed to the non-uniformity in peroxide-cured networks while the γ-irradiated polyisoprene networks were uniformly crosslinked. However, further investigation on how the heterogeneity of crosslink density distribution affects the ΔT_f was not available due to the fact that the networks architecture used was not ideal or controllable. In this section we tried to provide further insight into the effect of inhomogeneity (M_c distribution) in crosslinks on freezing point depression of softly confined gel solvent as well as the effect of the crosslink density using the model polymer networks with defined architecture.

5.2. Experimental Details

5.2.1. Sample Preparation

Model PTHF networks with different crosslink density and crosslink density distribution were prepared as described in Chapter 3 (section 3.1 and 3.2). Polymer networks with unimodal, bimodal and clustered architectures were designed and prepared as shown in Table 3-2 and Table 3-4. These samples were used to investigate the effects of crosslink density and the distribution of crosslinks, i.e., inhomogeneity.

In a typical case, a small piece of sample (~1 cm^2) was cut from the dry PTHF network sheet and the sample strip was swollen in benzene (HPLC grade, Sigma-Aldrich) at room temperature for 3 days. During the swelling process, the solvent was replaced every 24 hours to keep it fresh. Upon equilibrium swelling was reached, DSC sample for freezing point measurement was cut from the swollen network piece using a self-made

hollow punch and the size is such that it can fit the aluminum DSC pan loosely. Before sealing the DSC pan, a drop of fresh benzene was added into the pan to prevent the deswelling of the swollen sample by vaporization and also to act as a reference ("free" solvent) for the freezing point determination of trapped gel solvent. Care was taken to exclude any air so that the DSC pans contained only gel and solvent.

5.2.2. Freezing Point Measurements Using DSC

Differential scanning calorimetry (DSC) is one of the most convenient methods when dealing with phase transitions that involve thermal events such as melting, freezing, etc. The freezing point measurements were carried out using DSC (Seiko Instruments, DSC Model DMS210) and the values of freezing point were obtained from the temperatures of the heat-flow maxima in the DSC scans (thermograms). The DSC sample pans used in this work are large-volume hermetic aluminum pans (TA Instruments # 900793.901) designed for liquid state sample measurements.

Benzene was chosen as the swollen solvent in this work for the reasons that it is a good swelling agent for PTHF networks and the freezing point of pure benzene (~ 5.5 °C) is in a favorable range for these experiments. Also, the supercooling effect of benzene was moderate and it gave relatively large freezing point depressions with moderately crosslinked samples.

The choice of cooling rate is critical in freezing point depression measurements. It should be carefully chosen to balance the effect of deswelling at too slow cooling rate and suppression of freezing of trapped gel solvent at too fast cooling rate. When a slow cooling rate was used, confined solvent in the networks could diffuse to the surface to prevent a gel solvent freezing peak from being observed at all; while at a too fast cooling

rate, interference between the signal of the free solvent and the gel solvent was severe and the onset temperature for freezing of the gel solvent was difficult to detect. In this work, a cooling rate of 25 °C/min was found to be the most acceptable compromise. In each measurement, the thermograms of freezing (solidification) were recorded on DSC instrument by decreasing the temperature from room temperature to -65 °C at the rate of 25 °C/min.

Upon cooling, pure benzene shows a sharp, single peak corresponding to its bulk freezing point at -0.18 °C as shown in Figure 5-1 (a). The lower value of freezing point of pure benzene (compared with 5.5 °C) is due to the supercooling effect at high cooling rate of 25 °C/min. A typical DSC cooling curve for benzene in swollen PTHF networks is shown in Figure 5-1 (b). In all cases of benzene-swollen PTHF networks, two freezing peaks were observed: a sharp freezing peak and a broad freezing peak at lower temperature. The sharp freezing peak results from the freezing of solvent not trapped in the network, i.e. free solvent, whereas the trapped gel solvent freezes at a lower temperature due to the constraints in crystallization. The crystallization of the swelling agent occurs successively according to the size so that a broad freezing peak is observed instead of the sharp peak of free benzene. The width of the peak thus depends on the distribution of the size of cavities within the network. For homogeneous networks the width is narrower, while the heterogeneity in polymer networks is manifested as width broadening of the peak.

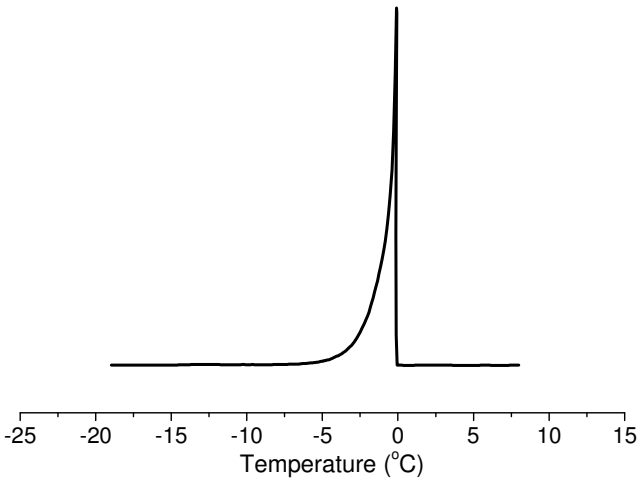

(a)

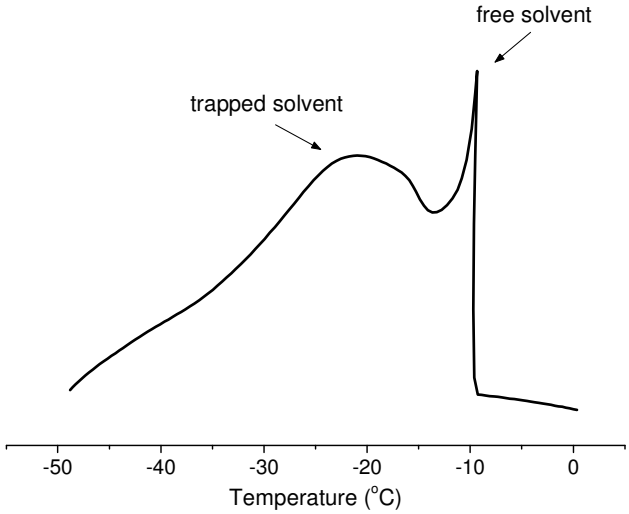

(b)

Figure 5-1 DSC freezing curves of: (a) pure benzene and (b) confined benzene in swollen PTHF network at cooling rate of 25 ºC/min

5.3. Crosslink Density Effect

Since the magnitude of the depression of freezing point is closely related to the limited size of solvent crystals formed, it would be expected that the nano-scale soft confinement from a rubber network would affect the freezing behavior of trapped gel solvent. Kuhn [142] postulated that solvent nuclei can grow undisturbed inside the

meshes of a gel until the crystallite sizes become comparable to the mesh dimensions. Further growth is hampered by the chains between the crosslinks, unless the temperature is lowered enough to render subsequent growth around the chains thermodynamically feasible. In actual practice, however, such low temperatures would simultaneously induce rapid nucleation in all meshes and effective growth beyond the range of each mesh can therefore be ruled out. As a result of this, the crystallite dimensions are essentially determined by the chain lengths between crosslinks, i.e., M_c.

For unimodal networks, the chain length between crosslinks has a very narrow distribution; therefore, the pore size distribution which solely depends on the inter-crosslink chain length distribution is fairly uniform. The freezing point should exhibit a larger depression with denser crosslink sites due to the smaller pore size or pocket size in the networks formed by the shorter inter-crosslink segments. The results of freezing point depression (ΔT_f) for unimodal PTHF networks with varying crosslink density (i.e., by varying the length of polymer chains between crosslinks) and corresponding pore size (D) calculated from Eq. 5-2 were shown in Figure 5-2. As mentioned, the average molecular weight between crosslinks, M_c, is used as an indicator of crosslink density. Shorter inter-crosslink segment length (lower M_c value) gives a higher crosslink density.

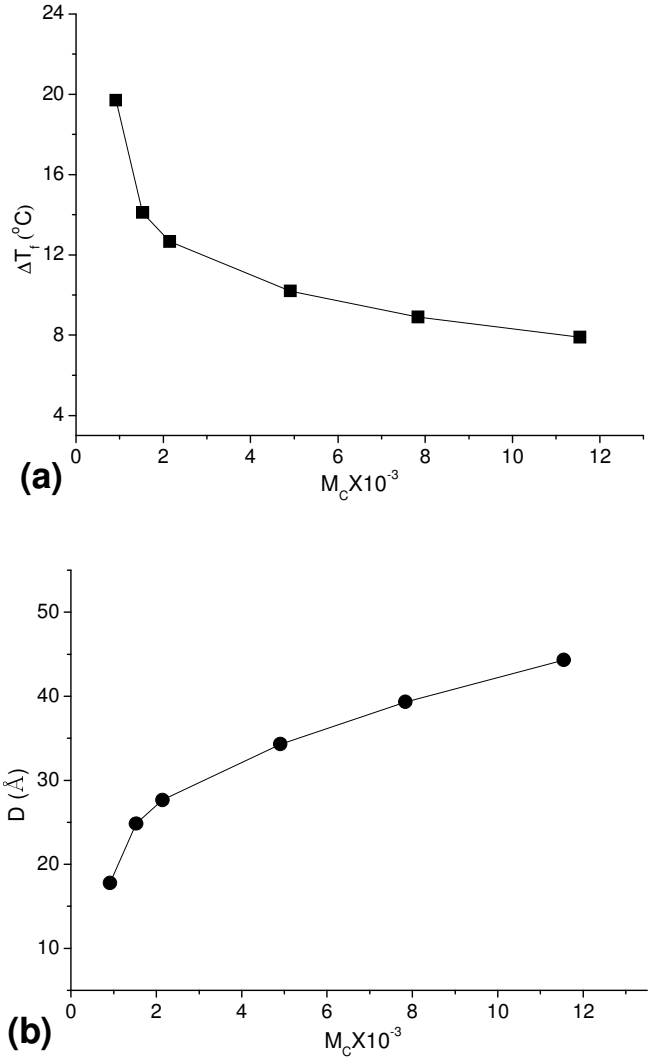

Figure 5-2 Effect of crosslink density on freezing behavior of confined benzene in unimodal networks: (a) freezing point depression; (b) calculated crystal size of benzene from Eq. 5-2

As can be seen, the freezing point depression, ΔT_f, progressively increases as the crosslinking density of the network increases. The network with shortest inter-crosslink chain length shows the largest magnitude in freezing point depression, as much as 20 °C was observed. Similar observations regarding the crosslink density effect on freezing point depression were also obtained in natural rubber swollen in cyclohexane [149] and

benzene [146], and cyclohexane-swollen polyisoprene networks [148], photo-irradiated EPDM networks swollen in *n*-heptane [150].

Freezing point of a trapped gel solvent is controlled by the possibility of the formation of a crystal nucleus with critical size within the meshes of polymer chains. Consequently, the depression in freezing point results from the limited size of the crystals formed. In swollen model networks, the trapped solvent can be considered to be micro-droplets, which are restricted in the small "pores" or "meshes" formed by the polymer segments as sketched in Figure 5-3. Intuitively, highly crosslinked networks (with small M_c) have smaller meshes compared with networks with lower crosslink density and thus the crystal growth of solvent within the smaller meshes is severely limited. Due to the higher surface energies of smaller crystallites, a higher vapor pressure prevails over such crystallites, leading to a larger decrease in their freezing point. Thus, not only does the presence of crosslinks retard crystallization of the network itself, but the crystallization of the diluent present in the swollen gel is also severely hampered.

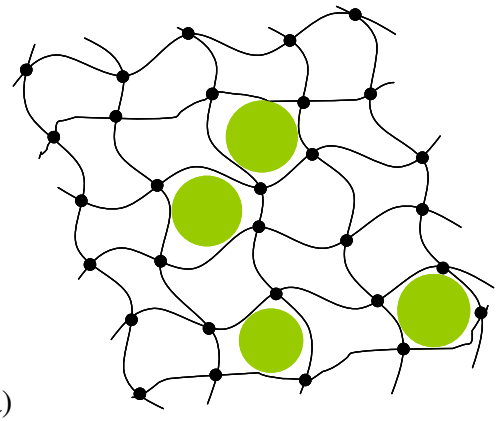

(a)

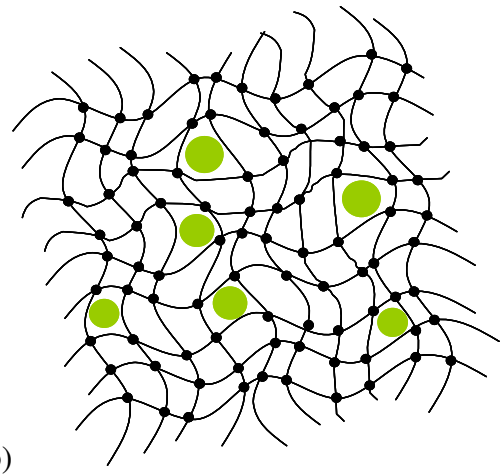

(b)

Figure 5-3 Schematic sketches of gel solvent crystals grown within the "meshes" formed by network inter-crosslink segments: (a) low crosslink density; (b) high crosslink density

Also it should be noticed in Figure 5-2 that the increase in freezing point depression with crosslink density becomes slower when M_c exceeds roughly 3000. This is probably due to the entanglement effect for relatively long segment between crosslinks, which would reduce the effective "pore" size and thus limit the growth of gel solvent crystals. The same trend was observed in bimodal networks with varying crosslink densities. Regardless of the bimodal architecture, the magnitude of the freezing point depression increases with increasing crosslink density, reflecting a smaller average pore size or mesh size in bimodal networks resulting from the high feeding ratio of short chains.

5.4. Inhomogeneity Effect

As shown in previous section, the extent to which the normal freezing point is suppressed depends on how much the solvent is constrained within the networks pores, i.e., the distance between the junctions, M_c. However, for the networks other than unimodal architecture, the pore size would take a wider distribution depending on the connectivity, even though the long chains and short chains are monodispersed chains.

This inhomogeneity effect in crosslink density distribution on the freezing point depression has not been clearly explored yet. In this section, the effect of inhomogeneity on freezing point depression was investigated by comparing the freezing behavior of benzene confined in model PTHF networks with different topologies, i.e., bimodal and clustered networks. By varying the feed ratio of long and short chain precursors in the pre-reaction process, inhomogeneities were introduced into the networks. It is expected that for the same average crosslink density (or average length of polymer chains between crosslinks, M_c), inhomogeneities increase from unimodal to bimodal to clustered network architecture. In other words, unimodal networks have the most homogeneous distribution in crosslink density and clustered ones are the most heterogeneous. This inhomogeneity in the network architecture would definitely manifest itself in the different freezing behavior of confined benzene.

Systematic freezing point measurements were carried out on the benzene-swollen networks with unimodal and bimodal M_c distribution. Figure 5-4 depicts the comparing results of freezing point depression and the corresponding pore size calculated through Eq. 5-2 for unimodal and bimodal networks. The composition details of the networks in question can be found in Table 3-2.

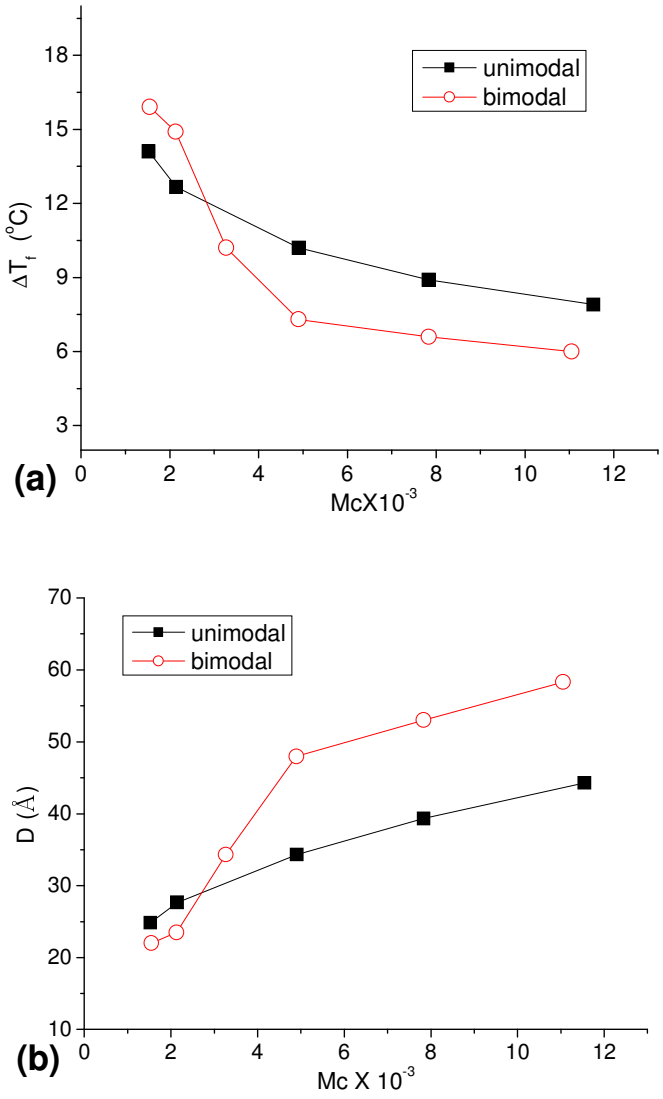

Figure 5-4 Effect of inhomogeneities on freezing behavior of confined benzene: (a) freezing point depression; (b) calculated crystal size of benzene using Eq. 5-2

Given the same average crosslink density (M_c), bimodal networks are more heterogeneous due to the random end-linking of long (M_n = 13051) and very short (M_n = 917) segments between crosslinks, while the segment length is quite uniformly distributed in unimodal networks. As shown, in lower M_c range (< 3000), bimodal distribution of segment length results in slightly larger depression of freezing point of gel solvent compared to the unimodal networks with same average M_c, indicating that the

average pore size or mesh size in bimodal networks is smaller than the one in unimodal networks. This is due to the existence of the very short segments (M_n = 917) in bimodal networks. It has been assumed in most previous works that the long and short chains are connected randomly in bimodal networks. However, SANS results in the study of epoxies [151] and bimodal PTHF networks [17] showed that segregation of short and long chains occurs during the end-linking process, i.e., the end-linking is not statistically random. For low M_c networks, very short chains are abundant in amount and thus aggregation of these short chains during end-linking is possible, resulting in formation of very small "meshes" and thus larger freezing point depression. With increasing the amount of long chains into bimodal networks, the aggregation effect of short chains is diluted and many more large-sized "meshes" are formed by the long segments. According to the nucleation theory, a higher freezing point is predicted for long inter-crosslink segments due to the higher nucleation in the larger "meshes". Therefore a lower depression in freezing point of gel solvent was observed in bimodal networks than that in corresponding unimodal networks for high average M_c. It seems to indicate that heterogeneous structure weakens the depression effect in freezing point of gel solvent, which was also observed by Grobler et al [148] in which heterogeneously crosslinked polyisoprene has higher freezing points than homogeneous γ-irradiated polyisoprene.

To further explore the inhomogeneity effect on the freezing behavior of confined benzene, benzene-swollen clustered networks was investigated. As mentioned, clustered networks have quite unique network architecture, in which highly crosslinked short chain clusters are embedded in a relatively loosely crosslinked long chain matrix. This topology is quite new and unique and no information is available in the literature on elastomers

with clustered topology. In this work, "clustering" time is taken as an evaluation of the cluster size. The longer "clustering" time is, the larger the cluster size and the broader the cluster size distribution become as shown in Table 3-4.

Measurements of freezing point depression were carried out on the clustered networks at 3 different cluster size level: small (2 or 3 hours), medium (6 hours) and large (8 hours). Resulting clustered PTHF networks have two different average inter-crosslink molecular weights, 3270 and 4908, respectively with three different cluster sizes (small, medium and large). Figure 5-5 (a) and (b) show the results of freezing point depression, ΔT_f, and calculated gel solvent crystal size, D, as a function of clustering time (i.e., cluster size) for these two batches of networks.

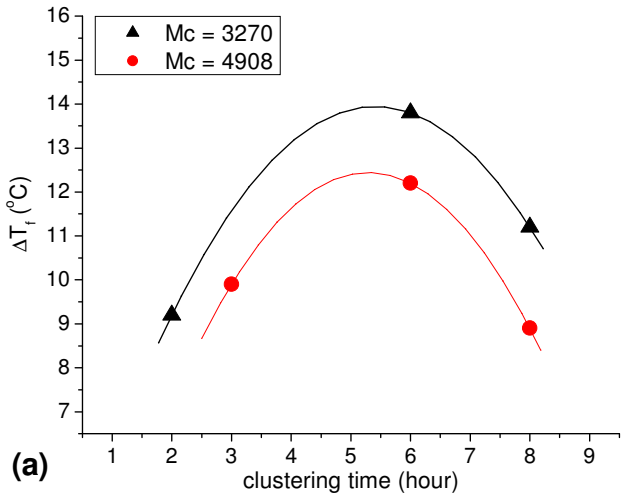

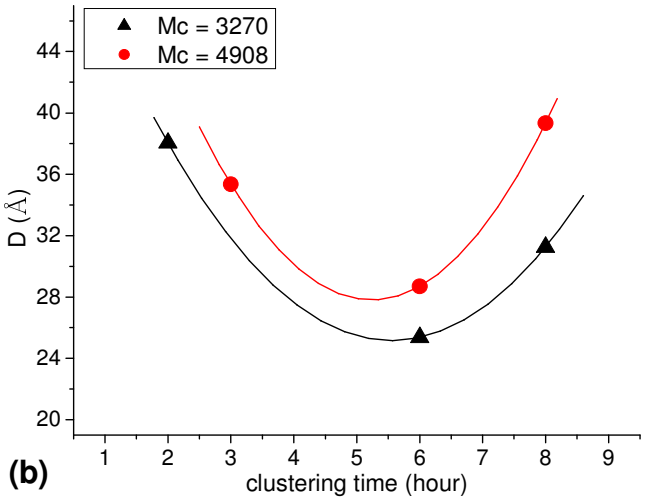

Figure 5-5 Effect of cluster size and cluster size distribution on freezing behavior of confined benzene: (a) freezing point depression; (b) calculated crystal size of benzene using Eq. 5-2

Firstly, it shows without exception that networks with lower average molecular weight between crosslinks (M_c = 3270) have larger values of freezing point depression than those with higher M_c (4908) indicating a smaller average "mesh" size. In addition, it is noticeable that the depression in freezing point of gel solvent increases with increasing cluster size at first and reaches a maximum value. Then it deceases with further growth of clusters. This trend was observed for both series of clustered networks with different average M_c. As mentioned in bimodal networks, short chain precursors tend to aggregate and form very small "meshes" during endlinking process. This aggregation situation becomes extreme in clustered network preparation since the short chain precursors are intentionally allowed to exclusively end-link with each other for certain clustering time before further end-linking with long chain precursors. Longer clustering time gives larger clusters of high crosslink density, resulting in many more small "meshes" that are able to severely confine the crystallization of gel solvent. Also according to PDI values

measured by GPC (Table 3-4), small and medium-sized clusters are relatively narrowly distributed in size (PDI < 2.2), which means that they are also relatively evenly embedded or distributed in the final networks. Therefore it is reasonable to see that ΔT_f increases with increasing clustering time at first. With further clustering reaction, it is possible that these multifunctional medium-sized clusters would react with each other to form clusters with very large size, while the number of these clusters would decrease fast at the same time. In addition, due to their large size, these clusters may not be able to be fully incorporated into the final networks, which would result in more defects like dangling long chains, and even dangling large clusters. Large-sized meshes are thus formed resulting from these defects and therefore a reduction in the magnitude of freezing point depression for clustered networks after long clustering time (~ 5 hours) occurs. Therefore not only the size but also the size distribution of clusters has effects on the freezing behavior of confined gel solvent.

CHAPTER 6

MOLECULAR DEFORMATION BEHAVIOR OF MODEL PTHF NETWORKS - SMALL ANGLE NEUTRON SCATTERING STUDIES

Molecular deformation of polymer networks under uniaxial stretch is the focus of this chapter. Direct measurements of chain deformation in polymer networks were carried out using small angle neutron scattering (SANS) on networks containing some labeled chains. In SANS the degree of chain extension (anisotropy of radii of gyration) and the morphologies arising from external uniaxial strain on polymer networks were measured. Dimensions of molecules or segments are obtained from quantitative measurements of scattering vector Q variation of the scattered intensity.

6.1. SANS Instrumentation

Small angle neutron scattering facility used in this work is located in IPNS (Intense Pulsed Neutron Source) at Argonne National Laboratory (Argonne, IL). Figure 6-1 shows an overhead plan view of the SANS instrument. The neutron source is a direct thermal beam from the reactor which passes through solid methane moderator, MgO filter, a Soller collimator and finally reaches the sample. Since it is a fixed-geometry instrument, i.e., the sample-detector distance is fixed at 2.0 m, different wavelength neutrons (arriving at the detector at different times), scattered through the same angle will have different Q values even though the scattering angle is still determined by the detector size and the sample detector distance. Hence the broader the incident wavelength range, the wider the Q range of the instrument. The wavelength available for this instrument is from 1 Å to 14 Å and the pulsed beam has a frequency of 30Hz. Therefore

the corresponding Q range is within 0.0035 to 0.6 $Å^{-1}$ with a resolution ($\Delta Q/Q$) of 0.3 to 0.023.

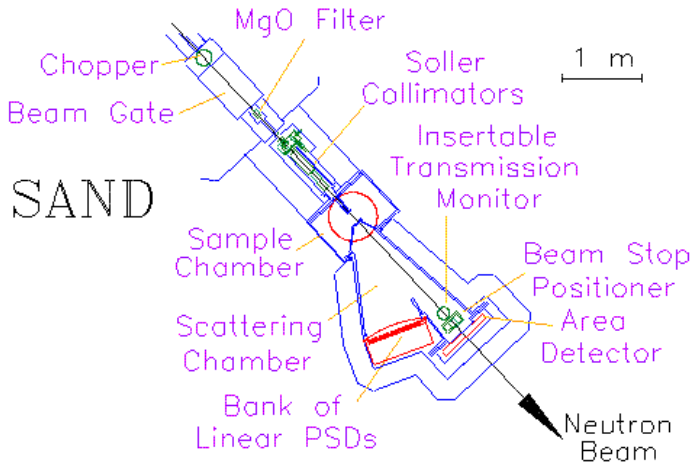

Figure 6-1 SANS instrument at Argonne National Laboratory

At the sample position, a chamber housing an 8-specimen, computer controlled, stepping-motor-driven sample changer is available for room temperature measurements and stretching measurement is available using a manual stretcher.

The detector is a larger area detector of dimensions 40×40 cm^2 with a spatial resolution of 4 - 6 mm FWHM. The detector is in a plane perpendicular to the incident neutron beam at a distance of 2 m behind the sample. The beam diameter at the area detector is 2.1cm. The large area detector and large sample-to-detector distance enable SAND to obtain higher quality data in a much wider Q range in a single measurement.

6.2. SANS Measurements and Data Analysis

6.2.1. SANS Samples and Uniaxial Stretching

Samples used in SANS measurements are selectively deuterated PTHF networks with known amount of deuteration fraction: unimodal network (designated as UdL), short

chain deuterated (BdS-1, 2…) and long chain deuterated (BdL-1, 2…) bimodal networks, clustered networks with either deuterated clusters (CTdS-1, 2…) or deuterated long chains (CTdL-1, 2…). The composition is listed in Table 3-3 and Table 3-5. Sample sheets were cut into strips with dimensions of approximately 1 in×3 in×0.5mm to cover the incident beam and fit with both sample changer and stretcher.

Network strip was held firmly on a sample stretcher (Figure 6-2) by means of two crossheads and was aligned perpendicularly to the incident beam. A micrometric screw operated the displacements of the crossheads, which allows uniaxial stretching of the sample and accurate measurements of its length before and after deformation. The extension ratio $\lambda = L/L_0$ was obtained by measuring the distance between two marks. The scattering from a given network sample was measured at the unstretched state first and then at increasing extension ratios. All measurements were done at room temperature.

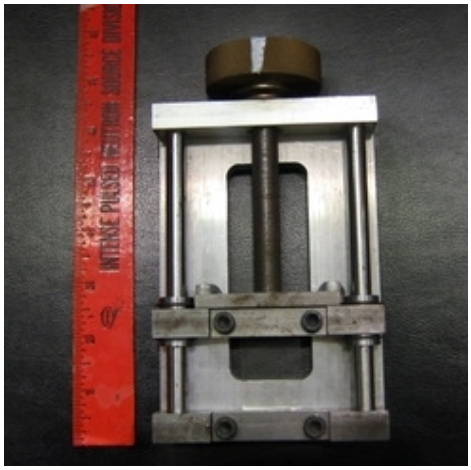

Figure 6-2 SANS sample stretcher

6.2.2. SANS Data Analysis

Neutron scattering patterns were recorded and all the data for coherent scattering contribution was obtained by appropriate subtraction of background and incoherent

scattering over whole Q range investigated and were corrected for the sample thickness. Scattered intensity $I(Q)$ of samples was measured as a function of Q. The scattering vector Q is defined as the difference between the incident wave vector and the scattered wave vector with a modulus of

$$Q = \frac{4\pi}{\lambda} sin\frac{\theta}{2} \qquad \text{Eq. (6-1)}$$

where λ is the wave length and θ is the angle between incident and scattered wave vector. Therefore Q is always in a plane perpendicular to the incident wave vector and it may have any direction with respect to the stretching axis indexed by azimuthal angle ψ. The important direction are the parallel direction (ψ = 0°) and the perpendicular direction (ψ = 90°) to the stretching axis (see Figure 6-3).

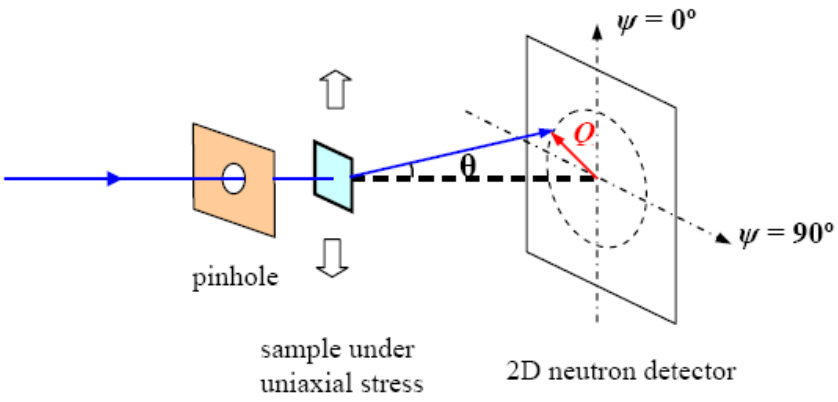

Figure 6-3 Schematic representation of the neutron scattering experiment

One of the most important properties of SANS is that the second term of the expansion of form factor or shape factor, $F(Q)$, has a very simple geometrical meaning, independent of the scattering properties of the sample. It depends on and is sensitive to both the size and shape of the scattering center; it gives the radius of gyration [152].

$$F(Q)^{-1} = 1 + [\langle R_g^2 \rangle / 3]Q^2 + \ldots \qquad \text{for } Q^2 R_g{}^2 << 1 \qquad \text{Eq. (6-2)}$$

For isotropic samples (unstretched networks) the scattered intensity was circularly averaged ($0^o \leq \psi \leq 360^o$). The radius of gyration (R_{g0}) was then calculated by fitting the intensity with appropriate model like Debye-Gaussian flexible polymer chains or unified fit. For the anisotropic stretched samples, what is analyzed is the projection of the radius of gyration in two directions, i.e., directions parallel and perpendicular to the stretching axis. The sector angle is optimized so that the maximum or minimum radius of gyration is obtained, depending on whether the scattering is parallel or perpendicular to the deformation axis, respectively. Therefore, only sectors at $\psi = 0^o$ and 90^o were analyzed and averaged within $\Delta\psi = \pm 20^o$ (Figure 6-4) to calculate $R_{g\parallel}$ and $R_{g\perp}$.

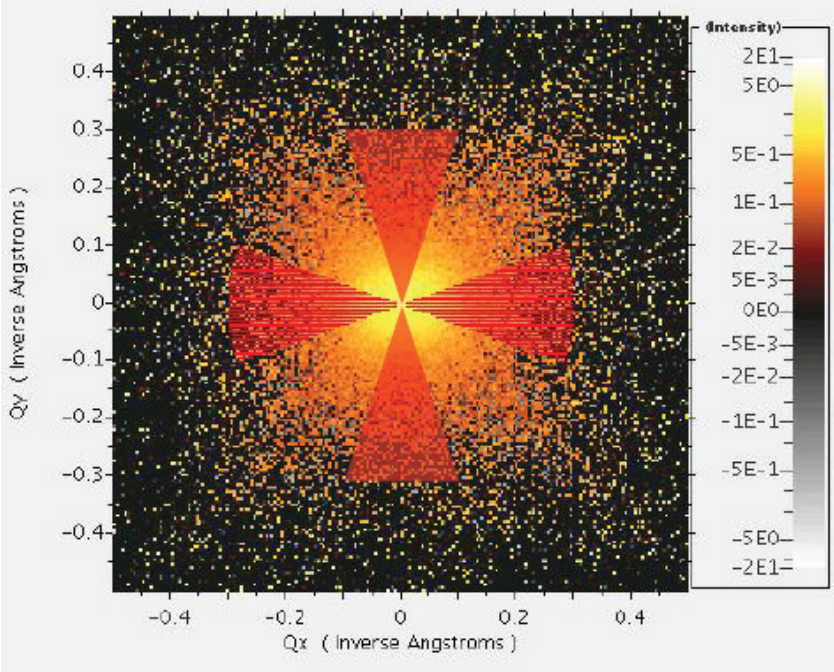

Figure 6-4 Sectors averaging at $\psi = 0^o$ and 90^o ($\Delta\psi = \pm 20^o$)

For a given two-dimensional spectrum, lines may also be drawn joining all points of equal neutron count, called isointensity lines. In this way neutron scattering intensity contour plots can be made.

6.3. Radius of Gyration in Anisotropic Neutron Scattering

The anisotropic radii of gyration relevant to scattering are given by [153]

$$R_{g,k}^2 = R_{g0}^2\left(\frac{1}{2}+\frac{3}{2}\frac{\left\langle R_k^2\right\rangle}{\mathbf{R}_0^2}\right) \qquad \text{Eq. (6-3)}$$

where k denotes $\|$ and $\perp$ respectively, R_{g0} is the isotropic radius of gyration, and $\mathbf{R_0}$ is the isotropic end-to-end vector of the elementary chain. R_k is the projection of the deformed end-to-end vector $\mathbf{R}$ in the direction parallel ($\mathbf{R}_{\|}$) and perpendicular ($\mathbf{R}\perp$) to the direction of elongation, and <...> denotes an average over all elementary chains.

With respect to the deformation of end-to-end vector $\mathbf{R}$, different theoretical network deformation modes can be applied to relate it with the extension ratio λ. Here three popular models are considered: affine deformation, phantom network deformation and junction affine deformation.

Affine Deformation.

As the simplest rubber elasticity model, affine deformation theory says that each chain segment of the network chains are oriented as if embedded in an affinely deforming continuum - that is, the macroscopic and microscopic deformations are identical. If the chains deform affinely, the radii of gyration parallel and perpendicular to the deformation axis are related to the extension ratio λ by

$$\frac{R_{g,\|}}{R_{g0}} = \alpha_{\|} = \lambda$$

$$\frac{R_{g,\perp}}{R_{g0}} = \alpha_{\perp} = \lambda^{-1/2} \qquad \text{Eq. (6-4)}$$

where the network is assumed to be incompressible.

Phantom Network Deformation.

The phantom network model, due to James and Guth [154, 155], is based on the assumption that the mean position of the crosslink points deform affinely and that the fluctuations in the crosslink points are Gaussian and independent of the applied deformation. It was shown that phantom network deformation has dependence on the functionality f of the crosslinks [156].

$$\frac{R_{g,\|}}{R_{g0}} = \alpha_{\|} = \left[\frac{f+2+(f-2)\lambda^2}{2f}\right]^{1/2}$$

$$\frac{R_{g,\perp}}{R_{g0}} = \alpha_{\perp} = \left[\frac{f+2+(f-2)\lambda^{-1}}{2f}\right]^{1/2} \qquad \text{Eq. (6-5)}$$

Model PTHF networks in this study have tetrafunctional junction points, i.e., f = 4, the expressions can then be simplified further as

$$\frac{R_{g,\|}}{R_{g0}} = \alpha_{\|} = \left(\frac{3+\lambda^2}{4}\right)^{1/2}$$

$$\frac{R_{g,\perp}}{R_{g0}} = \alpha_{\perp} = \left(\frac{3+\lambda^{-1}}{4}\right)^{1/2} \qquad \text{Eq. (6-6)}$$

Junction affine deformation.

It is also called end-to-end pulling model. In this mode, the crosslink junctions are fixed in space and the deformation of the elastic chains is induced by the displacement of the crosslink junction, which is affine in the macroscopic deformation [157].

$$\frac{R_{g,\|}}{R_{g0}} = \alpha_{\|} = \left(\frac{1+\lambda^2}{2}\right)^{1/2}$$

$$\frac{R_{g,\perp}}{R_{g0}} = \alpha_{\perp} = \left(\frac{1+\lambda}{2\lambda}\right)^{1/2} \qquad \text{Eq. (6-7)}$$

This case can be considered as a limiting case of phantom network behavior as f becomes infinite in Eq (6-5), which corresponds to the theoretical case in which the crosslink fluctuations are frozen.

6.4. Results and Discussion

6.4.1. Chain Conformation in Unstretched Model Polymer Networks

SANS experiments were first conducted on the networks in unstretched state to study the dependence of chain conformation on different network architectures. Also the radii of gyration measured are referred as undeformed or original dimension of labeled elastic chains, R_{g0}, in Eq. (6-3) – (6-7). Table 6-1 shows the values of radii of gyration of labeled chains in undeformed unimodal, bimodal and clustered networks.

Table 6-1 Chain Dimension in Unstretched Model PTHF Networks

Networks*	M_n **(L)**	M_n **(S)**	M_c	R_{g0} **(Å)**
Ud**L**	12800	11546	11860	44.157 ± 0.612
Bd**L**-1	12800	853	5000	32.598 ± 0.155
CTd**L**-2-S	12800	853	7000	25.749 ± 0.222
CTd**L**-2-M	12800	853	7000	24.434 ± 0.151
Bd**S**-4	11546	925	5000	21.226 ± 1.482
CTd**S**-2-M	17782	925	7000	44.190 ± 1.804

* d**S** – short chains are deuterated; d**L** – long chains are deuterated
** S – small size clusters (3 hr); M – medium size clusters (6 hr)

As shown in Table 6-1, the conformation of the long chains changes when they are incorporated or crosslinked in different types of networks. The dimension of long chains decreased with increase in crosslink inhomogeneities. In unimodal network, the long chains are endlinked to the chains that have similar length. The chains are long and flexible so that their conformation is not affected much due to the restriction of crosslink

junctions. They could assume the similar conformation as in melt state and thus the long chains in unimodal network show the largest radius of gyration of around 44Å (Figure 6-5 a). While in bimodal network, due to the introduction of very short chains, long chains have more chance to endlink with them rather with the long chains themselves. In this sense the long chains have to "squeeze" in dimension to complete the crosslinking with the short chains. These chemical crosslinks restrict the freedom and mobility of long chains and thus result in smaller radius of gyration of about 32Å (Figure 6-5 b).

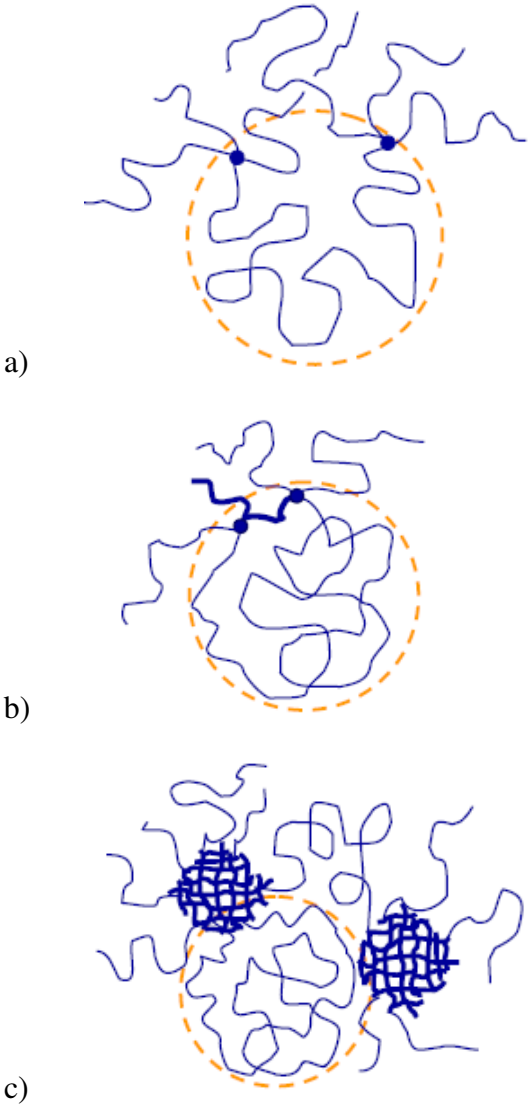

Figure 6-5 Chain conformation in undeformed (a) unimodal network; (b) bimodal network; (c) clustered network (bold lines indicate short chains)

For long chains in clustered network, the restriction on the chain mobility due to the inhomogeneities becomes worse. In addition to the restriction of some short chains that are not incorporated in clusters, clusters act as "giant" multifunctional crosslinker in crosslinking reactions. Therefore the long chains lose more possible conformations due to the spatial restriction, which results in even smaller dimension of around 25Å (Figure 6-5 c). However, the change in cluster size (CTd**L**-2-S vs. CTd**L**-2-M) does not have obvious influence on the long chain conformation for given average M_c.

As for the conformation of short chains (Bd**S**-4 vs. CTd**S**-2-M), it should be noted that the short chain dimension in clustered network is much larger than that in bimodal network. Recalling the unique architecture of clustered network, it is logical to assume that what SANS observed in short-chain-deuterated clustered networks are the clusters rather than individual short chains. The clusters were measured as a unity since they are densely crosslinked short chains.

6.4.2. Inhomogeneity Effect on 2D Neutron Scattering Patterns upon Uniaxial Stretching

Three sets of representative neutron scattering isointensity contour plots for deuterated long chains in unimodal (UdL), bimodal (BdL-1) and clustered networks (CTdL-2-M) are shown in Figure 6-6, Figure 6-7 and Figure 6-8, respectively. The contour plots were recorded at unstretched state (0%) and four strain levels (25%, 50%, 100% and 200%) for each sample. There are two general observations: i) the two dimensional scattering patterns become progressively anisotropic as the elongation ratio increases for all three types of networks; the intensity varies with ψ (angle between Q vector and stretching axis) at small Q region; ii) the discrepancies in the scattering

patterns among unimodal, bimodal and clustered networks becomes remarkable at high strain levels (e.g., 100% and 200%).

According to theory prediction, a so-called "butterfly pattern", a two-lope isointensity scattering pattern, should form in the direction perpendicular to the stretching axis at low Q region. However, it is interesting to notice that "butterfly patterns" are actually observed in the direction parallel to the stretching axis for bimodal and clustered networks, which are referred as "*abnormal* butterfly patterns". When increasing λ, they look inscribed inside an ellipse or "diamond" envelope. The contour maps prolate and oblate with respect to the stretching direction at small and large Q's, respectively.

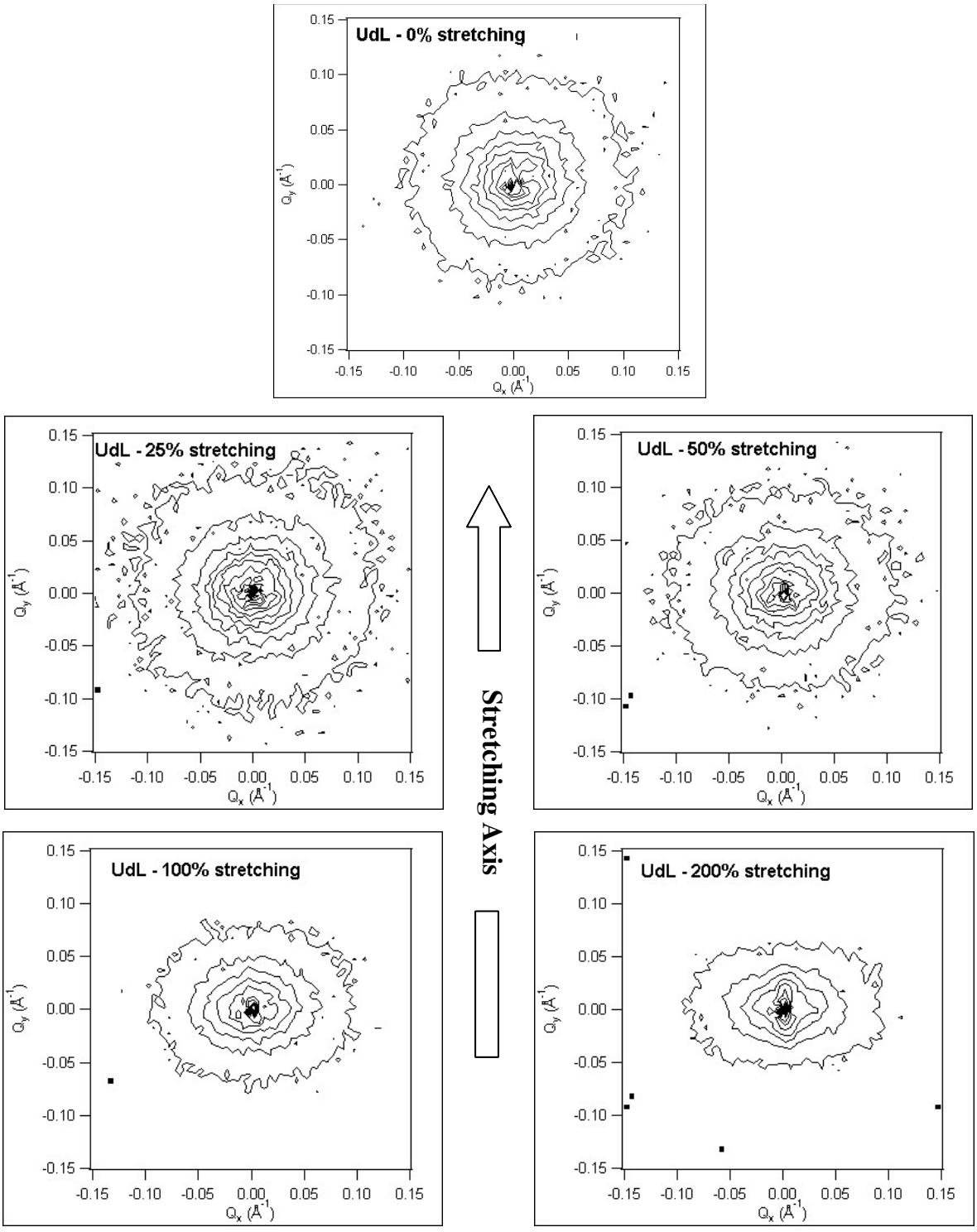

Figure 6-6 Isointensity patterns for unimodal network (UdL) at four elongation levels: 25%, 50%, 100% and 200%

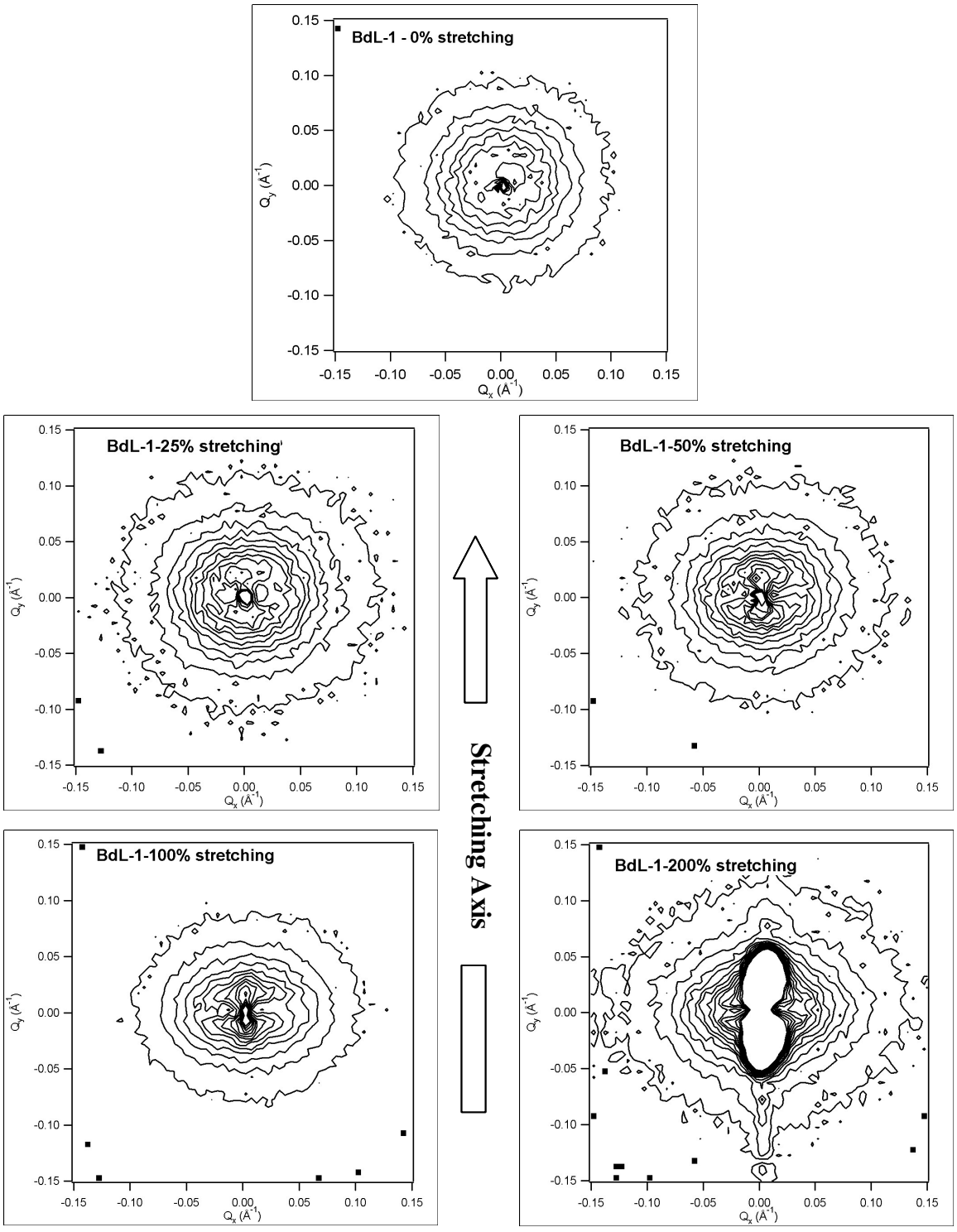

Figure 6-7 Isointensity patterns for bimodal network (BdL-1) at four elongation levels: 25%, 50%, 100% and 200%

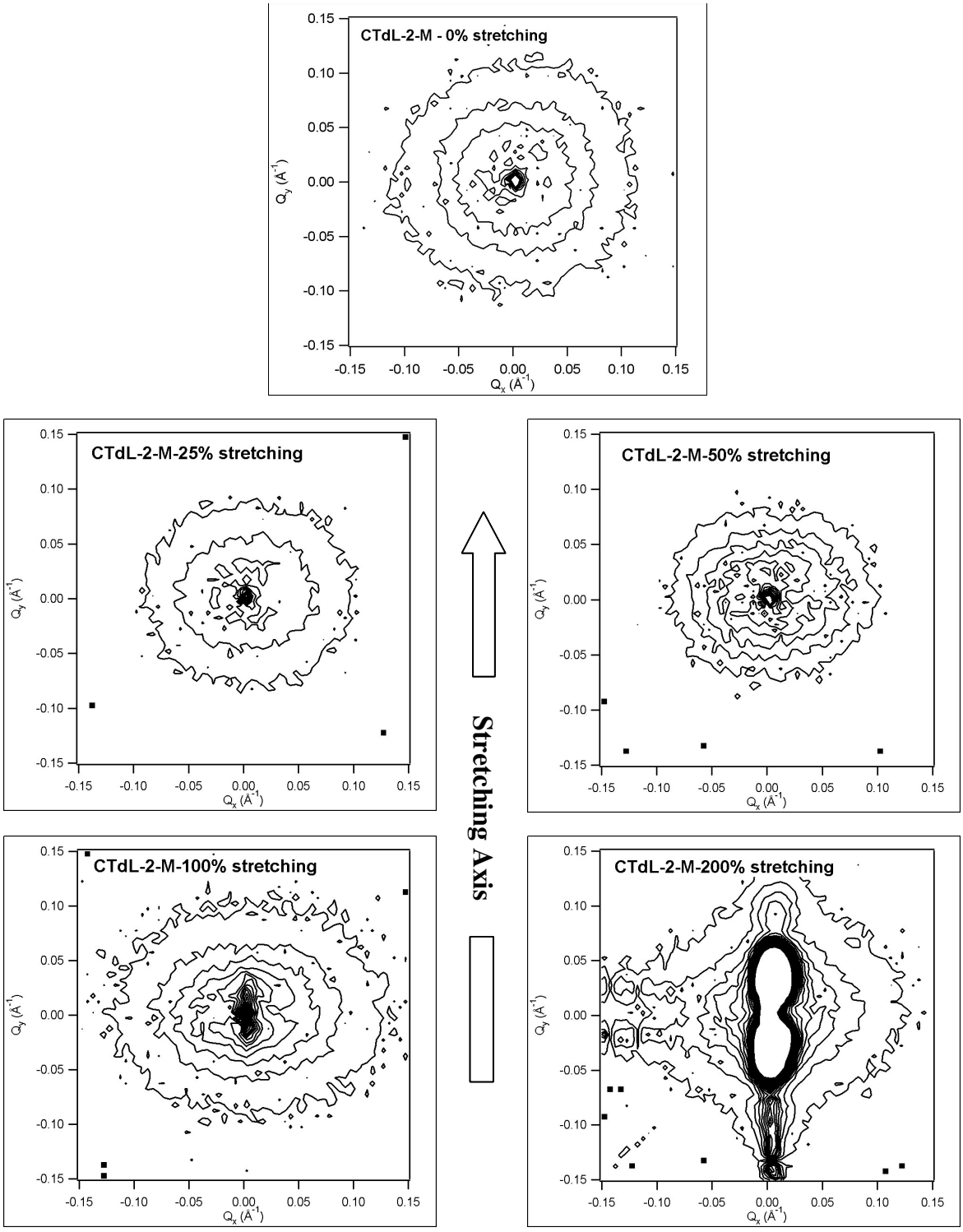

Figure 6-8 Isointensity patterns for clustered network (CTdL-2-M) at four elongation levels: 25%, 50%, 100% and 200%

The "*abnormal* butterfly patterns" were also observed by Bastide et al [31, 158, 159] and Onuki [160, 161] in anisotropically deformed PS gels. By adding a spatial inhomogeneities term in the scattering function, an "*abnormal* butterfly pattern" was reproduced by Onuki through the elasticity theory approach, i.e., the structure factor due to the inhomogeneity was maximized in the most stretched directions and suppressed in the perpendicular direction. Thus it was stated that spatial inhomogeneities in crosslinks were the molecular origin that is responsible for the "*abnormal* butterfly patterns".

The above approach is also reasonably applicable to our case for the reason that the long deuterated chains studied are the same in all three networks, the only difference lies in the distribution of crosslink points, i.e., inhomogeneities in network topology and the way how they are crosslinked. As designed, inhomogeneity level increases in the order of unimodal network < bimodal network < clustered network, i.e., unimodal network is the most homogeneous in terms of crosslink distribution while clustered one is the most heterogeneous. Inhomogeneities are implicit in the state of preparation because topological inhomogeneities introduced by cross-links are buried by concentration fluctuations of the polymer chains. The inhomogeneities, however, become explicit by deformation, such as swelling, stretching, or compression.

For unimodal network, in addition to its homogeneous nature, the intercrosslink polymer chains are long and flexible. Therefore the crosslinks are relatively "mobile", which may reduce the increase in spatial inhomogeneities during deformation due to the ability of rearrangement of the distribution of crosslinks. As a result unimodal network show the expected normal scattering pattern with a major deformation axis perpendicular to the stretching direction (Figure 6-6). In this sense it is expected that the deformation

behavior of unimodal network would deviate far from affine behavior but be close to phantom deformation, which will be discussed quantitatively in next section.

For intrinsically heterogeneous bimodal and clustered networks (Figure 6-7 and Figure 6-8), the innermost isointensity contours begin to change shape with stretching and the "*abnormal* butterfly patterns" become more and more defined as the elongation ratio increases. According to Onuki's theory, the crosslink inhomogeneities preferentially increase in the stretching direction. When stretched, the frozen inhomogeneity "blobs" are displaced along the stretching direction without changing their shapes significantly. Thus the anisotropic spatial separation of the frozen "blobs" amplifies the concentration fluctuations along the stretching axis, generating an appearance of "*abnormal* butterfly pattern" at small Q regions. For higher Q regions, the isointensity curves show the tendency to become ellipses, which is related to the average stretching of individual chains.

As discussed in the literature, crosslink inhomogeneities usually manifest themselves as an increase or upturn in the scattered intensity, which is particularly amplified in deformed networks, such as in swollen gels (isotropically deformed) and in stretched or compressed networks (anisotropically deformed). Figure 6-9 shows the scatted intensity of these three networks at 200% stretching in the direction parallel to and perpendicular to the stretching axis. As shown the trend in scattering intensity for three PTHF networks is in agreement with the scattering pattern observed and also in good agreement with the inhomogeneity levels of those networks. Clustered network (CTdL-2-M) has the highest degree of inhomogeneity and thus the largest scattered intensity especially at high strain. Unimodal network (UdL) shows the lowest scattering

intensity since it is the most homogeneous one. Bimodal network (BdL-1) is in the intermediate region.

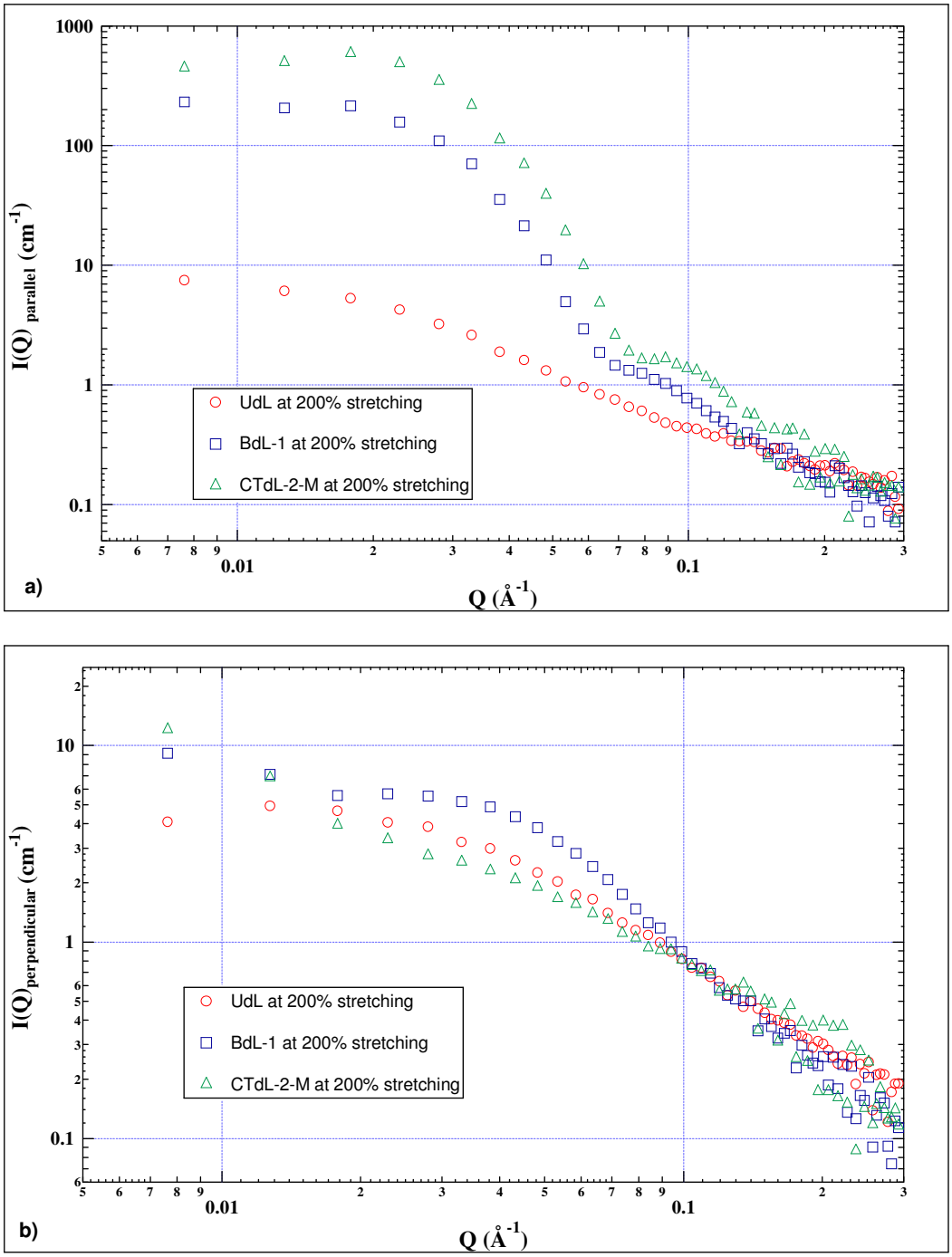

Figure 6-9 SANS scattering intensity, I(Q), in the parallel (a) and perpendicular (b) directions for unimodal (UdL), bimodal (BdL-1) and clustered (CTdL-2-M) networks at the elongation ratio of 200%

However, to obtain insightful molecular deformation mechanism, quantitative analyses on the radii of gyration at directions parallel and perpendicular to the stretching axis are necessary. With qualitative discussions on "*abnormal* butterfly patterns" we are now on the stage to explain it in quantitative way. In next three sections the chain conformations in unimodal, bimodal and clustered networks are analyzed quantitatively and the molecular deformation mechanisms are proposed.

6.4.3. Chain Conformation in Unimodal PTHF Network under Uniaxial Stretching

Figure 6-10 compares the experimental data of chain conformation in unimodal network with the predictions of three theoretical models based on affine deformation (solid line, Eq. 6-4), phantom network deformation (dash dot line, Eq. 6-6) and junction affine deformation (dash line, Eq. 6-7).

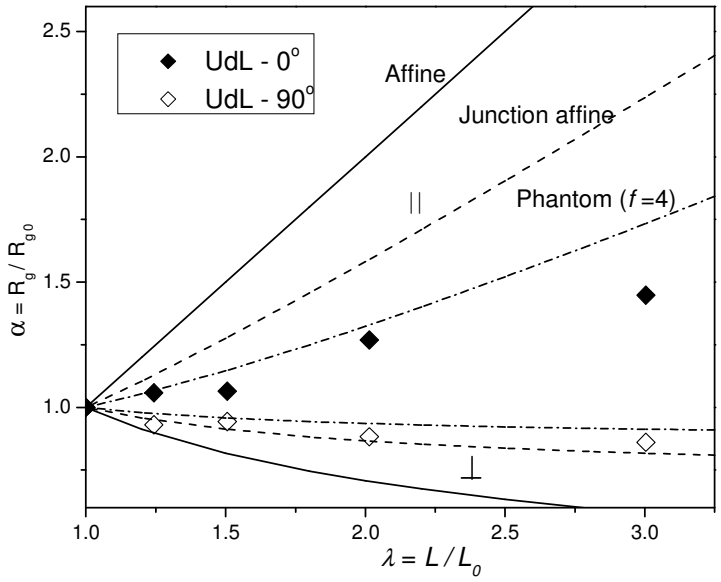

Figure 6-10 Variation of $\alpha_{\parallel}$ (0º) and $\alpha_{\perp}$ (90º) for deuterated chains as a function of draw ratio λ for unimodal network. Curves represent theoretical predictions: affine deformation (——), phantom network deformation f=4 (- · - ·) and junction affine deformation (- - -)

Clearly the chain radius of gyration in unimodal network increases on stretching far less than predicted by the affine deformation mechanism on mesh level. In the perpendicular direction, R_g evolution is close to the junction affine model and essentially more deformed than predicted by the phantom network. However in the direction parallel to stretching axis the chain deformation is even smaller than expected for a phantom networks with functionality of 4, which accentuates the extension of the end portions of the chains rather than the central section.

One might imagine that chain entanglements prevent the motion of the central portion of long chains in unimodal network. In addition, since the elastic chains are long (M_n=12,800) in unimodal network and crosslink reactions occur exclusively at functional chain ends, it is very likely that some functional groups are not linked or remain unreacted. Therefore the presence of pendent chains cannot be neglected and it also implies a decrease of the crosslink functionality. In this case the fluctuations of the junction positions are severe. As pointed out by Ullman [162, 163], chains in endlinked model networks have much greater sensitivity to crosslink functionality upon stretching than random crosslinked networks. Thus as shown in Figure 6-11, the chain deformation behavior in unimodal network is very close to that predicted for phantom network with average functionality of 3, rather than designed tetrafunctional ($f = 4$). This behavior implies the possibility of a high degree of mobility of junction positions and rearrangements of cross-link positions could possibly occur during deformation process. The crosslink junction points rearrange to yield the system with the lowest free energy. This rearrangement minimizes the actual extension of the chain.

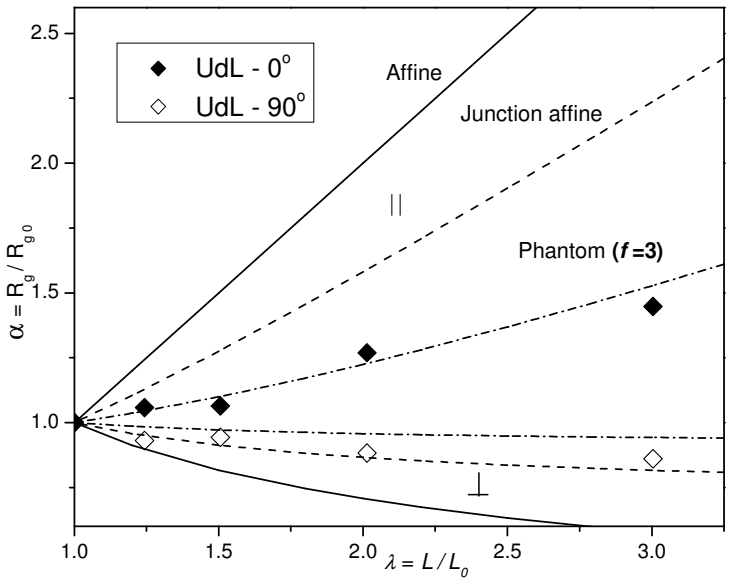

Figure 6-11 Variation of $\alpha_{\parallel}$ (0º) and $\alpha_{\perp}$ (90º) for deuterated chains as a function of λ for unimodal network. Curves represent theoretical predictions: affine deformation (––), phantom network deformation f =3 (- · - ·) and junction affine deformation (- - -)

6.4.4. Chain Conformation in Bimodal PTHF Networks under Uniaxial Stretching

As mentioned earlier, unimodal networks have close to mono-dispersed chain length distribution between crosslinks, while a bimodal distribution of inter-crosslink chain length exists in bimodal networks. Thus the bimodal networks are more heterogeneous than the unimodal ones in terms of crosslink distribution, at length scales larger than the length of short chains (but less than lengths that are much larger than the length of long chains). This difference in network architecture is expected to influence the responses of chain conformation to external strains. The conformations of deuterated long chains in unimodal and bimodal networks as a function of λ are compared as shown in Figure 6-12 (BdL-1 vs. UdL). Similar to unimodal network, the elementary chains in bimodal network are less extended in the direction of elongation than expected by the

assumption of affine deformation. Junction affine deformation model shows better agreement with the data for long chains in bimodal network.

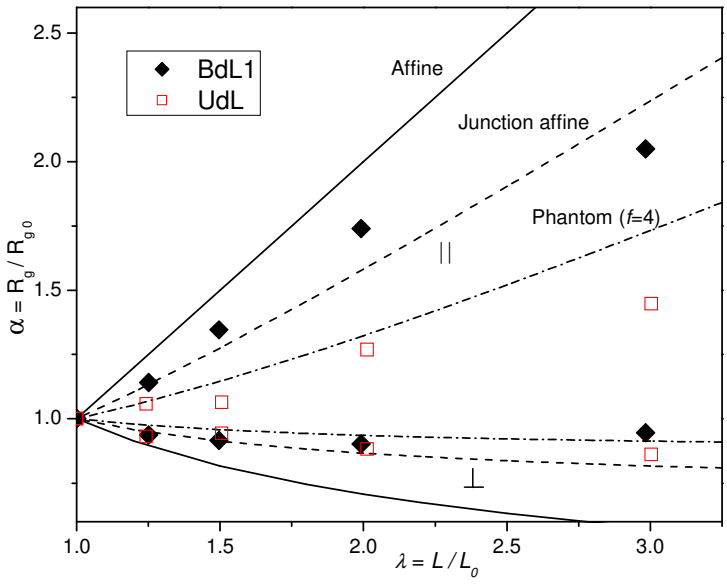

Figure 6-12 Comparison of $\alpha_{\parallel}$ (0º) and $\alpha_{\perp}$ (90º) for deuterated long chains in unimodal and bimodal network as a function of λ. Curves represent theoretical predictions: affine deformation (––), phantom network deformation f =4 (- · - ·) and junction affine deformation (- - -).

For a given strain, long chains in bimodal network have much higher orientation or unfolding than those in unimodal network. The discrepancy increases in the parallel direction with increase in strain, especially at high strain levels. Obviously crosslinking of long chains with very short chains in bimodal network moves the long chain elongation behavior from phantom deformation towards affine deformation. It is close to the prediction based on junction affine deformation. This observation implies that inhomogeneities in networks reapportion the strain distribution among chains, resulting in a much higher percentage of chains reaching their finite extensibility and increasing

network ultimate properties. This also explains the extraordinary mechanical properties of bimodal networks compared with unimodal ones in many rubber elasticity studies.

One advantage of using SANS to characterize the chain conformation is that the deformation behaviors of both long chains and short chains can be observed by selectively labeling one or other type of chains. Figure 6-13 depicts the conformation evolution of both long and short chains in bimodal networks upon uniaxial stretching.

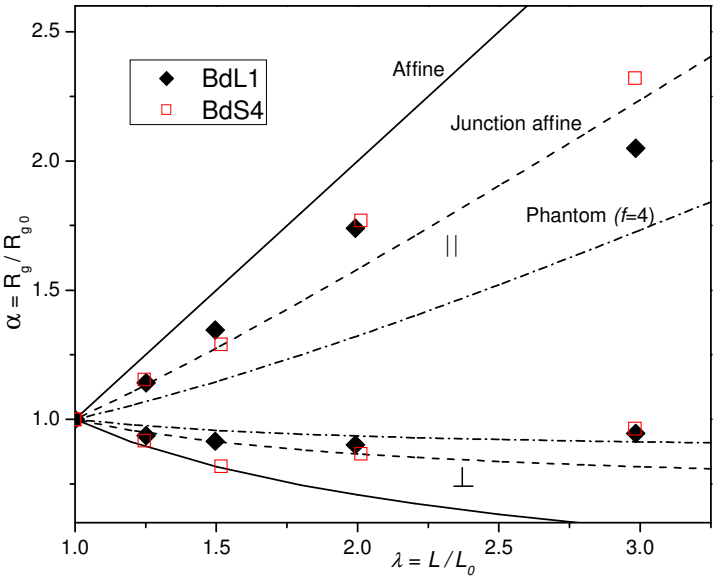

Figure 6-13 Comparison of $\alpha_{\parallel}$ (0º) and $\alpha_{\perp}$ (90º) for deuterated long chains and short chains in bimodal networks as a function of λ. Curves represent theoretical predictions: affine deformation (––), phantom network deformation f =4 (- · - ·) and junction affine deformation (- - -)

As a general observation, elastic behavior of both long chains and short chains in bimodal networks roughly follows junction affine deformation. At relatively low strains ($\leq$ 50%), both types of chains may be roughly described by the end-to-end pulling mechanism or junction affine deformation. However with further stretching, the responses of long chains and short chains become quite different. Short chains behave

closer to affine deformation while long chains deformation is closer to the phantom model prediction. In terms of orientation, short chains extend or unfold more than long chains along the stretching direction at large strain levels. In other words, short chains reach the finite extensibilities faster than the long ones. The result implies a high degree of mobility of the junction position related to long chains resulting in their low observed molecular deformation at high strain level. This behavior leads to the conclusion that during the deformation rearrangements of crosslink position could occur due to the inhomogeneities in crosslink distribution.

6.4.5. Chain Conformation in Clustered PTHF Networks under Uniaxial Stretching

To further explore the inhomogeneities effect on the chain elastic behavior, networks with clustered topology were prepared (Figure 3-14). Regarding the crosslink distribution clustered networks are the most heterogeneous. The big cluster junctions have their unique characteristics that differ from the traditional crosslink junctions (e.g., crosslinker) at least in two aspects: first, the clusters are tough but not rigid; they just need higher stress for deformation than the flexible long chains. They can be viewed as densely crosslinked unimodal networks made of very short chains. Second, the clusters are multifunctional; therefore, many more long chains are connected to a single cluster than to a regular tetrafunctional crosslinker. Also, the possibility of more defects (i.e., unreacted functional groups) increases at the same time. The conformation of long chains in clustered network (CTdL-2-M) and bimodal network (BdL-1) under uniaxial stretching is compared in the plot of Figure 6-14.

Obviously long chains in clustered network are more sensitive to the stretching than those in bimodal networks, especially at high elongation ratio. The long chains

become more anisotropic or more elongated along the stretching direction in clustered network than in bimodal network. The only possible cause for this observation is the different ways how long chains are connected to short chains in these two types of networks. In bimodal networks, long chains are randomly or statistically linked with short chains during the crosslinking process. While in clustered networks, long chains are connected to the big tough clusters rather than individual short chains. Moreover since multiple long chains are linked to single cluster, it is logical to assume that this topology actually increases the functionality, or in other words, it reduces the fluctuations of the average positions of crosslink junctions. It follows that upon uniaxial stretching the deformation of the elastic chains should be enhanced as observed that long chains in clustered network are more sensitive to the external strain.

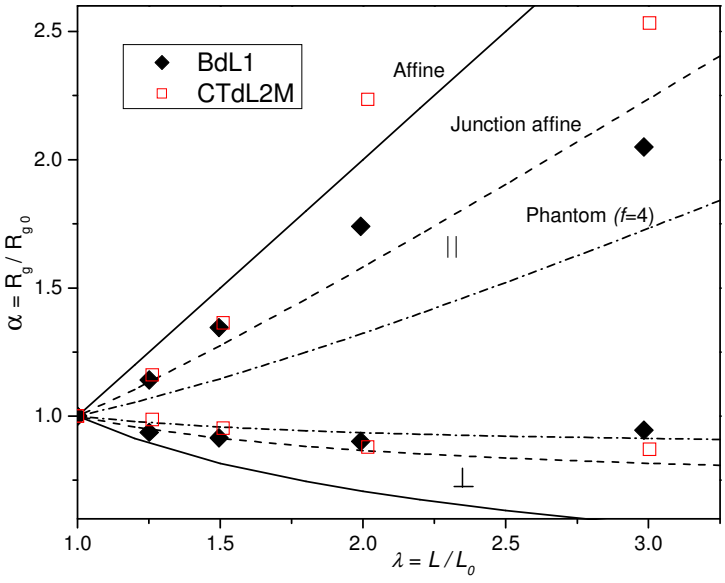

Figure 6-14 Comparison of $\alpha_{\parallel}$ (0º) and $\alpha_{\perp}$ (90º) for deuterated long chains in bimodal and clustered networks as a function of λ. Curves represent theoretical predictions: affine deformation (––), phantom network deformation f =4 (- · - ·) and junction affine deformation (- - -).

It would be interesting to observe the long chain orientation and the short chain orientation separately in clustered networks. It should be noted that for short-chain-deuterated clustered network, what is observed is not likely or necessarily the individual short chains between crosslinks; it is more likely that the clusters were measured as a unity since they are densely crosslinked short chains. The hypothesis is confirmed by the fact that R_g values for short-chain-deuterated clustered networks are much larger than those for short-chain-deuterated bimodal networks, in which short chains are assumed to be measured as individual chains. Therefore for short-chain-deuterated clustered networks, the short chain behavior that SANS measured is actually the behavior of the clusters. The comparison of the elongation behavior of long chains (CTdL2M) and clusters (CTdS2M) in the clustered networks is shown in Figure 6-15.

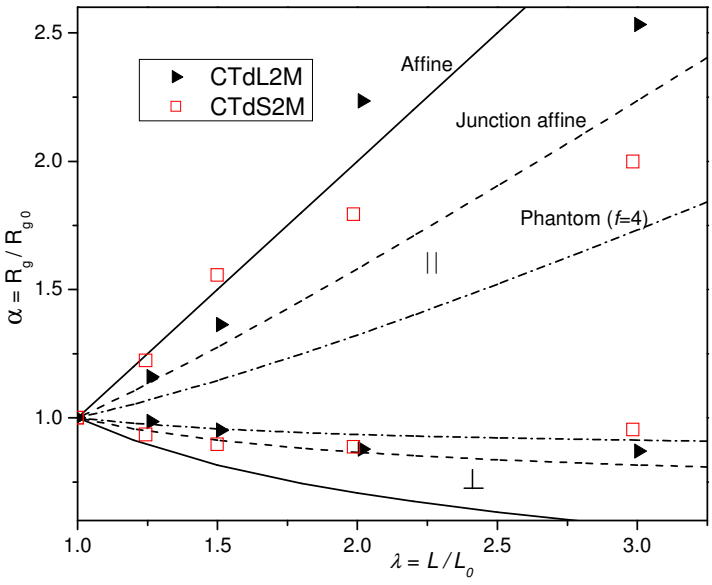

Figure 6-15 Comparison of $\alpha_{\parallel}$ (0º) and $\alpha_{\perp}$ (90º) for deuterated long chains and short chains in clustered networks as a function of λ. Curves represent theoretical predictions: affine deformation (––), phantom network deformation f =4 (- · - ·) and junction affine deformation (- - -).

As shown, at low strain levels ($\leq 50\%$), the clusters response to the external strain much faster than long chains. The deformation behavior of clusters approximately agrees with affine deformation predictions while long chains behave more like junction affine. When further increasing strain, the deformation behaviors of long chains and clusters in parallel direction change in opposite ways. The long chains assume a large portion of the deformation while the clusters are much less deformed relative to the stretching ratio.

To rationalize this observation, let us first recall this unique "clustered" topology. Due to the two-step crosslinking process, crosslink junctions are designed purposely to be non-randomly distributed in networks, which results in a high degree of inhomogeneities. Based on this consideration and the experimental findings, the deformation model for the clustered network is proposed as following. It is known that crosslink inhomogeneities preferentially increase in the stretching direction. At relatively low strains, compared with more flexible long chains, clusters respond to the strain faster due to their densely-packed short chain nature. However, with further increasing the strain, these clusters are displaced along the stretching direction without changing their shapes significantly. So they should separate in space along the stretching direction and interpenetrate more in perpendicular direction. Meanwhile long chains begin to assume most of the elongation and fully unfold or well orient along the stretching direction. That is why the transitional behavior in elongation of long chains and clusters is observed.

In addition, cluster size effect on the deformation behavior of long chains in the clustered network was also investigated. As described in Chapter 3 (section 3.2.3), cluster size was controlled by the "clustering time" and longer clustering time gives larger average cluster size and wider size distribution. Two size levels are considered: small

(CTdL-2-S, 3 hours “clustering”) and medium (CTdL-2-M, 6 hours “clustering”). The cluster size effect is shown in Figure 6-16. As can be seen, the size of clusters has negligible effect on the elongation behavior of the long chains that connect with them. It seems to indicate that the size change in clusters does not change much the way how long chains are connected to the clusters, which means the degree of inhomogeneities does not change much. Therefore it has minor effect on the elongation behavior of long chains.

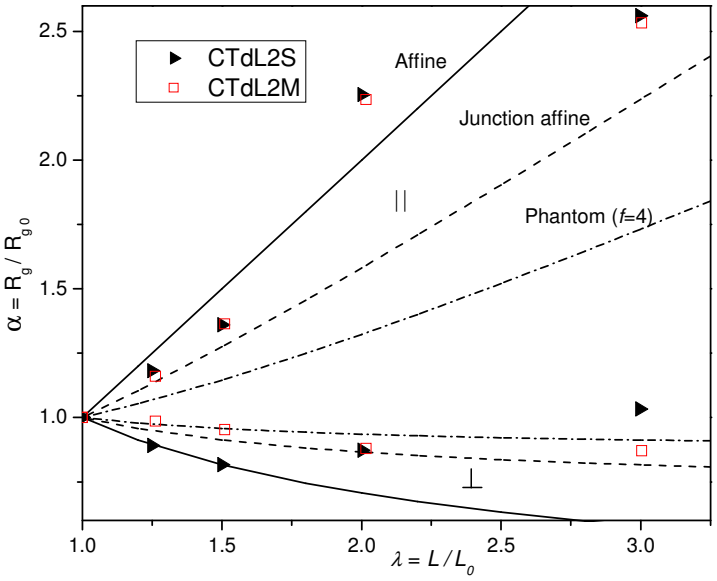

Figure 6-16 Comparison of $\alpha_{\parallel}$ (0º) and $\alpha_{\perp}$ (90º) for deuterated long chains in clustered networks with different cluster sizes as a function of λ. Curves represent theoretical predictions: affine deformation (––), phantom network deformation f =4 (- · - ·) and junction affine deformation (- - -).

CHAPTER 7

FREE VOLUME DISTRIBUTION IN MODEL LINEAR POLYMERS – MOLECULAR DYNAMICS SIMULATIONS

7.1. Methodology

A domain-decomposed parallel MD code, *ddgmq*, was used to evaluate the change in molecular architecture due to applied strains and temperature change. In the domain decomposition method the physical domain is divided into sub-domains, so that each processor only needs to account for one sub-domain. This accelerates the simulation speed on parallel computers with multiple processors [164, 165]. A model linear polymer resembling polyethylene was used for this study. A united atom model was adopted, and the force field used to compute the forces on each unit is explained below. This force field was used previously and has provided realistic results [166]. The covalent bond between two atomic clusters was treated as a rigid bond with the bond length of 1.53Å.

The bond angle potential is: $\Phi_\theta = 1/2\ k_\theta (cos\theta - cos\theta_0)^2$, where k_θ is a constant (520 KJ/mole) for a bending spring that idealizes the bond angle variation; θ_0 is the equilibrium bond angle (112.813^o); and θ is the bond angle at any time. Torsional potential restricts molecular rotation around single bonds due to steric hindrance and for a given dihedral angle it is taken as: $\Phi(\tau) = \sum_{m=0}^{5} C_m \cos^m \tau$, where τ is the dihedral angle that varies from -180^o to +180^o with $\tau = 0^o$ corresponding to the *trans* conformation. C_m's are the coefficients of a polynomial. For the united atom model, C_m's are taken from

literature as 8832.1806, 18087.0660, 4880.8037, -31800.0510, 0, 0 (J/mole). The Weeks-Chandler-Andersen potential (WCA) is used to account for the non-bonded interactions:

$$\Phi(|r_{ij}|) = \begin{cases} 4\varepsilon((\sigma/|r_{ij}|)^{12} - (\sigma/|r_{ij}|)^{6}) + \varepsilon & for\ |r_{ij}| \le 2^{1/6}\sigma \\ 0 & for\ |r_{ij}| > 2^{1/6}\sigma \end{cases}$$

where σ = 4.28 Å; ε = 57.0 (KJ/mol). Columbic interactions are not included as the sample is non-polar. Since MD simulations are computationally intensive, sample size should be small enough to be suitable for the computational capabilities but large enough to capture the essential physics of the behavior. Therefore, a compromise between both requirements needs to be found. Generally, several hundreds to several tens of thousands of atoms or atom units are used. Our samples are 400 PE-like chains with 100 repeat units (totally 40,000 atom units). Because the simulation cell is quite small compared to real systems, periodic boundary condition is used to reduce the influence of boundary effects on the simulation results. The temperature control is achieved using the loose coupling technique by Berendsen et al [165]. The internally measured temperature, *T(t)*, is coupled to an external heat bath of a temperature $T_{req}(t)$: $\dot{T}(t) = -(T(t) - T_{req}(t))/\tau_T$, where τ_T is a user specified relaxation time that determines how fast the temperature approaches to the required value. Simultaneously, the pressure tensor is also controlled. The size and shape of simulation box changes according to: $\dot{h}(t) = [P(t) - P_{req}(t)]/\tau_p \mu$, where μ is a pre-defined constant and τ_p is a user-defined relaxation time, P is the internally measured pressure tensor, and P_{req} is the required pressure tensor. The loose coupling technique is naturally over-damped and produces smoother, less oscillatory response to sudden changes in pressure or temperature.

All the simulations were done on a Silicon Graphics Origin2000 parallel system with 28 processors. A sample of 400 C100 PE chains with a density of 0.7g/cm^3 was generated by Pivot Monte Carlo sampling technique at 300K. It has been shown that the initial chain configurations prepared from Pivot MC sampling is not only unbiased, but also very close to that expected of the bulk melt [166]. Before simulation, the prepared sample was heated to 525K at a rate of 0.1K/ps and then was relaxed at 525K for 3 ns to minimize energy. After that, it was cooled to the required temperature at a rate of 0.1 K/ps. The tensile stress was applied at a rate of 1bar/ps. The boundary deformation of polymer sample under the applied stress is used to calculate the draw ratio (the ratio of the final length of sample to its original length) to represent the amount of stretch, along with engineering strains defined as the increase in stretch per unit original length. A flow chart of the simulation processes is given in Figure 7-1.

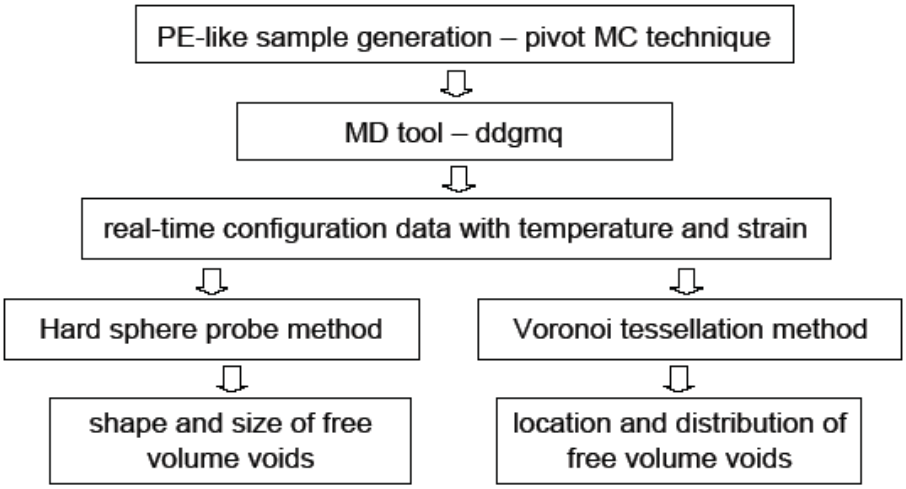

Figure 7-1 Flow chart of MD simulation on free volume and free volume distribution

7.1.1. Hard Sphere Probe Method

One geometric approach of analyzing MD configuration output is hard sphere probe method [167-169]. In this method the periodic box containing polymer samples is

divided into small cubic subcells (usually grid size < 1 Å) and each grid is scanned by a hard spherical probe. All of the atomic units are assumed to be hard spheres with radii of 88% of the van der Waals radii, R_{vdw}, which is modified to reflect the interaction between the probe and the polymer atom. Due to the insertion of a small probe of radius R_p, each atomic unit is assigned an effective radius: $R = R_{vdw} + R_p$, representing the radius of the volume that is excluded to the atom center. All polymer atoms are scanned first and marked as occupied subcells. After all polymer segments are exhausted what remains is the possible free volume. After checking occupancy, the hard probe is introduced at the center of an unoccupied subcell. An unoccupied subcell is considered to be inaccessible whenever more than half of the subcell lies within effective radius R of any atom. And they are classified as occupied subcells as well. Only the accessible unoccupied cells are counted as holes contributing to the free volume. The shape of the voids can be obtained if a dimensionless surface-to-volume ratio is defined: $w = (S/4\pi)/(3V/4\pi)^{2/3}$, where S is surface area and V is volume. The schematic diagram representing the hard sphere probe method is shown in Figure 7-2. Using hard sphere probe method, both the size and the shape of free volume voids in the polymer systems can be obtained.

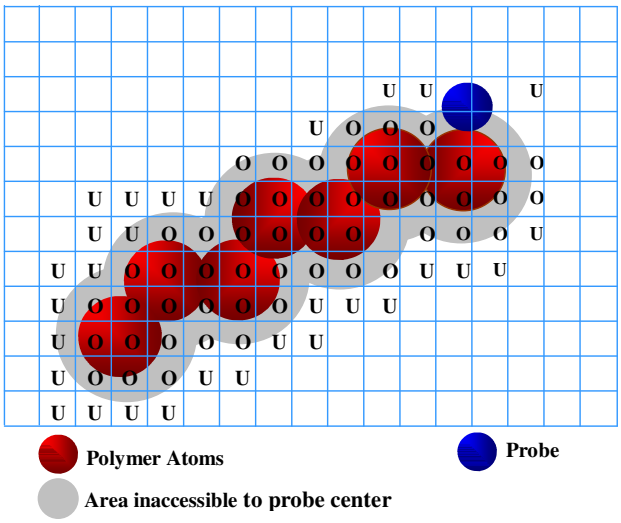

Figure 7-2 Hard sphere probe method

Obviously, the resulted value of free volume depends on the probe size. This dependence has been studied for both static [167] and stretching state [170]. It has been showed that the free volume decreased rapidly with increasing probe size and approached zero near a probe radius of 2Å, regardless of temperature and strain. In our study a probe size of 1Å is chosen in most cases due to the fact that it is close to the size of positron probe (1.06Å) in PALS, which makes the comparison between simulation results and experiment results reasonable.

7.1.2. Voronoi Tessellation Method

Voronoi tessellation [117, 171-173] method provides a good way to qualitatively characterize the free volume distribution. In tessellations, the atoms are considered to be the points distributed in the space and these points are partitioned into irregular tetrahedra such that the circumsphere of each tetrahedron is devoid of points except those lying on the vertices. Tessellation is thus obtained by connecting all geometric neighbors, where a set of atoms form a polyhedron as shown in Figure 7-3. So the system volume is uniquely

and completely divided into polyhedra comprising the space nearest to each atom. The volume of each polyhedron can be calculated from the tessellation result, which is then used to study the free volume. The solid lines form the Voronoi polygon about atom *i* and the dashed lines form the Delaunay triangles, whose circumspheres are centered at the corresponding vertices of the Voronoi polygon. The polymer atoms lie on the vertices of the Delaunay triangles and the void particles centered on the vertices of the Voronoi polygon. The diameter of voids equals that the diameter of the circle circumscribing the Delaunay triangle minus the diameter of the atoms. Thus a larger polyhedron volume around one atom indicates larger free volume around that atom. In this way, Voronoi tessellation technique provides a relative way to evaluate the distribution and location of free volume voids in the system.

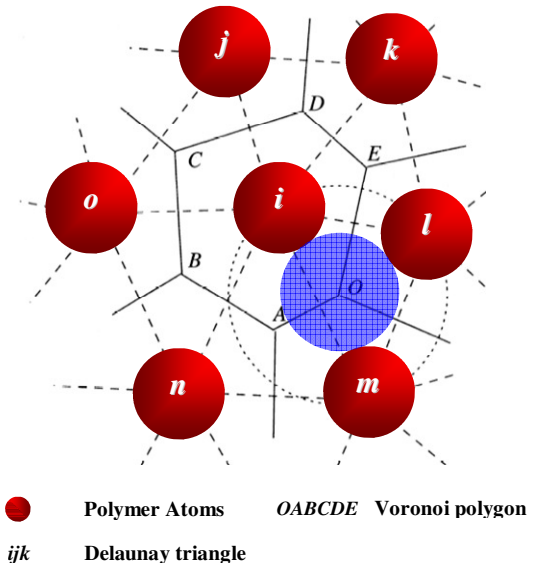

Figure 7-3 Voronoi tessellation method (2-D representation)

7.2. Probe Size Effect as a Function of Temperature

The amount of free volume highly depends on the size of the probe used for identifying and calculating the free volume using the hard sphere probe method,

irrespective of the temperature. Figure 7-4 shows the dependence of free volume fraction on the probe radius R_p for a polymer sample at various temperatures for an unstrained polymer. The simulation results are presented for three temperatures, 250K, 300K, and 360K. It can be seen that at 250K the free volume fraction is roughly equal to 33 % for R_p = 0 when draw ratio is equal to one, which is close to the simulation results for polybutadiene (32%) [167] and polycarbonate (39%) [174] with probe radius equal to 0. In the undrawn state, the total free volume increases slightly with an increase in temperature, at 300K, the free volume increases to 35% and at 360K it reaches 37 % with R_p = 0. The increase in free volume for a specific temperature increase is relatively unaffected by the probe size until the probe size reaches 1.15 Å. For probe size larger than 1.15 Å, the free volume becomes less dependent on temperature. When the probe size reaches 1.25 Å, temperature does not have any significant influence on the free volume. It is clear from the figure that the free volume fraction depends on the size of the probe, as the probe size increases free volume decreases rapidly. When the probe radius is above 1.5 Å, almost no free volume is accessible at all three temperatures.

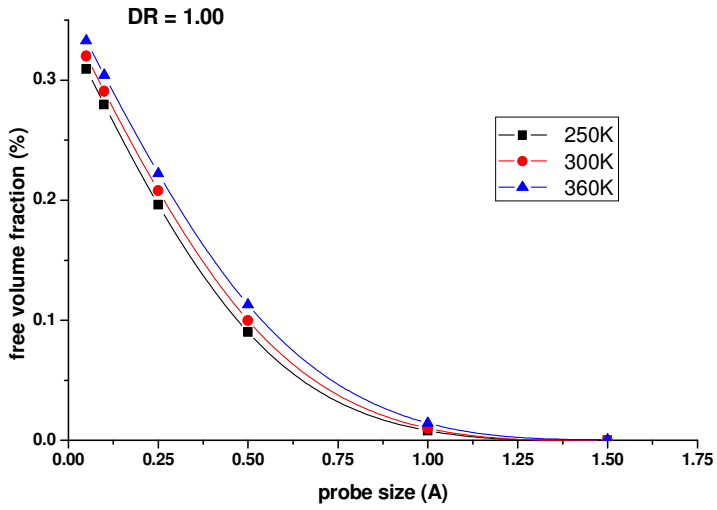

Figure 7-4 Free volume fractions accessible to spherical probes of different sizes for various temperatures

When the probe radius is less than 0.5 Å, voids with "infinite" size are found in the bulk system with periodic boundary conditions, as cavities are interconnected for all three temperatures. By increasing the probe size, the free volume cavities break up into discrete voids of finite size depending on the size of the probe. In this study, the "connectivity" between unoccupied regions was accomplished with a hard sphere of radius 1 Å. This connectivity diminishes significantly with a larger probe size. When explored with a probe size of 1 Å, the free volume fraction for an undrawn polymer was calculated to be around 1% for the system we studied for all three temperatures as shown in Figure 7-4. It is worthwhile to note that a comparable simulation result for a PBO system with a probe radius of 1 Å was 0.61% [169]. One could also see that the magnitude of changes in free volume induced by temperature is not significant compared to choice of the probe size. In most of our study, the probe size was chosen to be 1 Å for the fact that this size is comparable to the positron size used in PALS measurements. In this way, our simulation results can be reasonably compared with experimental results.

Even though the changes in the free volume due to stretch and temperature are not very high on an absolute scale, it should be noted that many properties, such as viscosity, change exponentially with the changing free volume fraction. Thus, small changes in free volume could result in significant changes in polymer properties. Some polymer properties, such as diffusion, depend not only on the total free volume but also on the orientation, shape, and size of the regions that form the total free volume. In the following sections the effects of orientation and temperature on the change of free volume cavities and its distribution are described.

7.3. Temperature Effect

Temperature effects on the free volume and the size distribution of free volume are shown in Figure 7-5. As shown from hard sphere probe method, temperature increase results in the expansion of total free volume (Figure 7-5 a). Figure 7-5 (b) shows the simulation results obtained from Voronoi tessellation analysis indicating the size distribution of relative free volume and corresponding Voronoi polygon size (with *y* axis showing the ratio of the number of atoms or atomic units with a specific polyhedron volume to the total number of atomic units in the system). As shown, the size distribution curve shifts to a large value indicating an increase in the mean size of free volume elements and the distribution becomes broader upon increase in temperature.

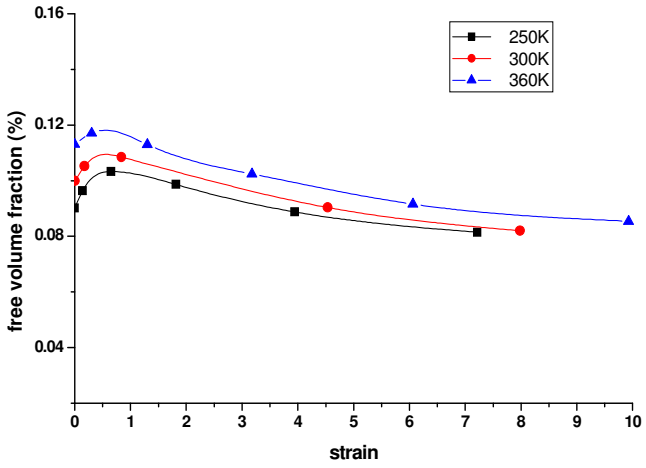

(a)

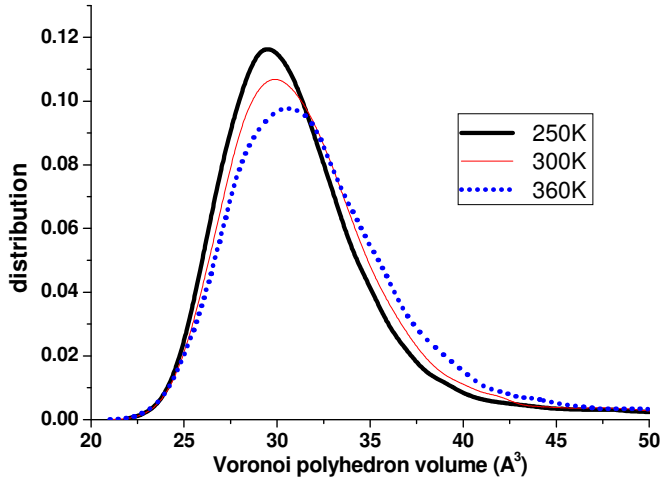

(b)

Figure 7-5 Temperature effect: (a) total free volume fraction from hard sphere probe method; (b) size distribution of free volume voids from Voronoi tessellation method.

Shape of free volume voids, as indicated by the shape factor *w*, at different temperatures is shown in Table 7-1. For voids of given size, temperature change does not have much influence on the shape of these voids. While at a given temperature, the increase in the free volume size is accompanied with the increase in the shape factors, indicating that large free volume voids are more elliptical than the smaller ones.

Table 7-1 Shape factor *w* of free volume voids at various temperatures*

	<= 5 Å	5 ~ 10 Å	10 ~ 20 Å	20 ~ 40 Å	40 ~ 60 Å	60 ~ 100 Å	> 100 Å
250 K	1.403	2.376	2.616	2.807	3.209	-	-
270 K	1.408	2.415	2.630	2.921	2.845	-	-
300 K	1.402	2.412	2.663	2.870	3.494	-	-
360 K	1.391	2.410	2.652	2.906	3.346	3.559	4.314

* Shape factor w = 1 for spherical shape, w > 1 for ellipsoid

7.4. Uniaxial Stretching Effect

Stretching effects on free volume and its distribution was analyzed at different draw ratios at 300 K as shown in Figure 7-6.

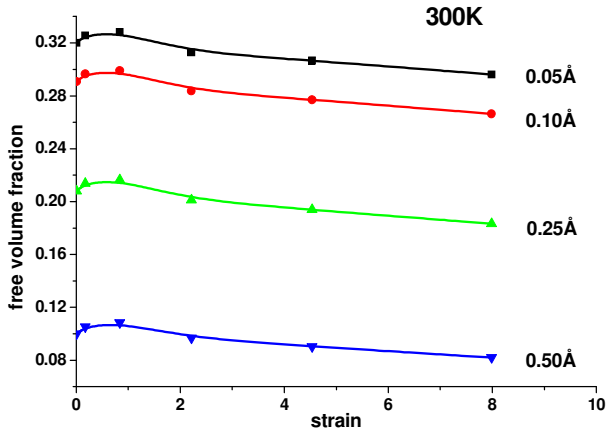

(a)

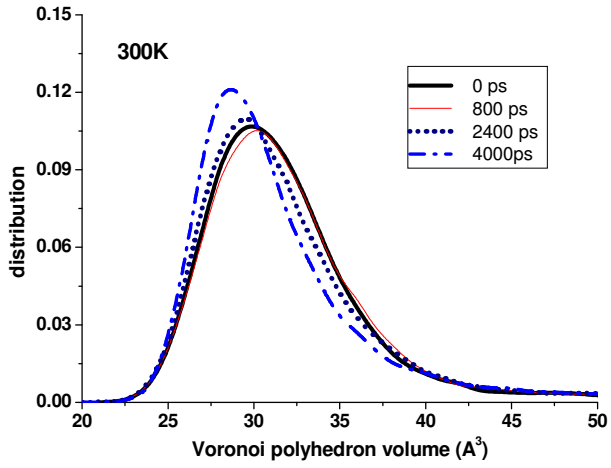

(b)

Figure 7-6 Stretching effect: (a) total free volume fraction from hard sphere probe method; (b) size distribution of free volume voids from Voronoi tessellation at 300K

From Figure 7-6 (a), one could see that the total free volume increases slightly for small uniaxial strains followed by a larger reduction for higher strains, which was also observed by some other researchers [175-177]. The initial expansion is possibly due to Poisson effect. As the draw ratio is increased, however, the chains begin to pack better and the resulting densification starts to dominate. In addition, uniaxial stretching results in smaller mean size of free volume voids and narrower size distribution (Figure 7-6 b). It should be mentioned that strains are shown in terms of stretching time, as strains increases with stretching time in a pattern given in Table 7-2.

Using hard sphere probe method, detailed classification of the size of free volume cavities with the number of such cavities present in 1 nm^3 of the polymer for different strains can be obtained as shown in Table 7-2. The number of small free volume voids (< 5 $Å^3$ size) decreases fast with strain. The number of medium sized holes (10 ~ 60 $Å^3$) initially increases and then decreases with larger strains. However, the number of larger cavities (> 60 $Å^3$) shows increase with strain. Moreover the formation of extra large cavities (> 100 $Å^3$) was observed at high strain level.

Table 7-2 Size distribution of free volume voids at different strain level at 300 K

Time	**0 ps**	**800 ps**	**1600 ps**	**2400 ps**	**4000 ps**
DR	**1.00**	**1.18**	**1.84**	**3.21**	**8.99**
<= 5 $Å^3$	9.627	9.118	7.900	6.575	4.986
5 ~ 10 $Å^3$	0.267	0.303	0.257	0.228	0.166
10 ~ 20 $Å^3$	0.160	0.206	0.202	0.168	0.134
20 ~ 40 $Å^3$	0.057	0.111	0.101	0.087	0.072
40 ~ 60 $Å^3$	0.006	0.021	0.021	0.021	0.024
60 ~ 100 $Å^3$	0	0.007	0.008	0.008	0.015
> 100 $Å^3$	0	0	0.001	0.002	0.002

Shape of the free volume voids, as indicated by the shape factor *w,* due to stretching effects is listed in Table 7-3. At any given strain, increasing cavity size is associated with increasing shape factor, indicating that larger voids are more elliptical than smaller ones and the shape factor increases with the size of the cavity. Increase in orientation results in the formation of more elongated larger voids in the sample corresponding to the largest size of voids.

Table 7-3 Shape factor *w* under various draw ratios (DR) at 300 K

DR	<= 5 Å	5 ~ 10 Å	10 ~ 20 Å	20 ~ 40 Å	40 ~ 60 Å	60 ~ 100 Å	> 100 Å
1.00	1.402	2.412	2.663	2.870	3.494	-	-
1.18	1.397	2.409	2.579	2.933	3.221	3.604	-
1.84	1.396	2.398	2.626	2.913	3.186	3.359	4.476
3.21	1.396	2.398	2.622	2.875	2.997	3.572	3.540
8.98	1.394	2.361	2.558	2.639	3.059	3.129	4.748

Upon stretching, polymer chains tend to align for better packing, resulting in the reduction of total free volume. However, there are no explanations on how these larger and more elongated free volume voids form with strain. It is logical to assume that the free volume cavities around a chain end are more likely to increase when the polymer sample is subjected to tensile force, since atoms can be pulled apart more easily at these locations. To verify this assumption, Voronoi tessellation technique was applied and the free volume distribution associated with atoms at the chain ends was separated from those associated with other atoms.

From Figure 7-7, one could see that that the polyhedron volume at chain ends increases with increasing DR, indicating the free volume at chain ends increases with increasing orientation. On the other hand, with increasing DR decreasing in polyhedron volume associated with atoms away from the ends of the polymer chains is observed.

This phenomenon indicates that the larger voids associated with the free volume during uniaxial stretching is formed at chain ends.

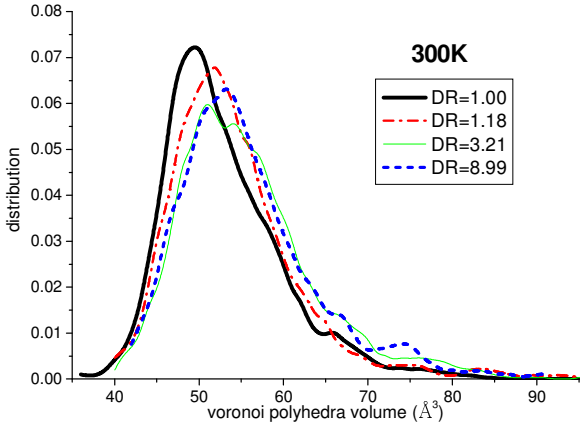

(a)

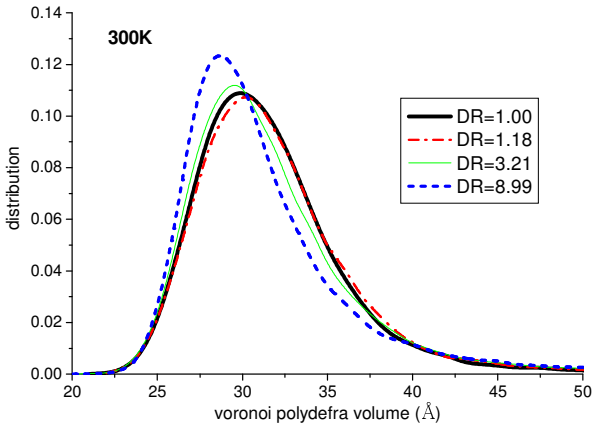

(b)

Figure 7-7 Voronoi polyhedron volume distribution for (a) atoms at chain ends; (b) atoms located away from chain ends at 300K

This mechanism was tested for its validity at various temperatures. Voronoi polyhedron volume distribution for atoms at chain ends at 250 K and 360 K is shown in Figure 7-8. One can see that the free volume distribution for atoms at chain ends follows a similar trend for all the temperatures. These observations indicate that the proposed mechanism for the formation of large voids during stretching is valid for all temperatures investigated in this work.

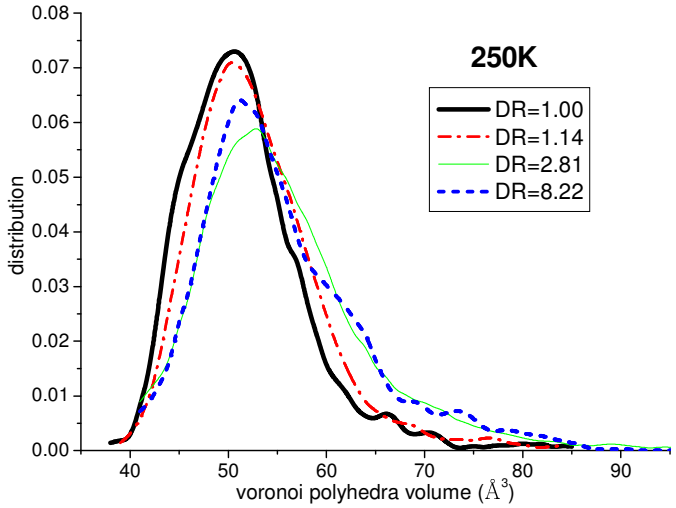

(a)

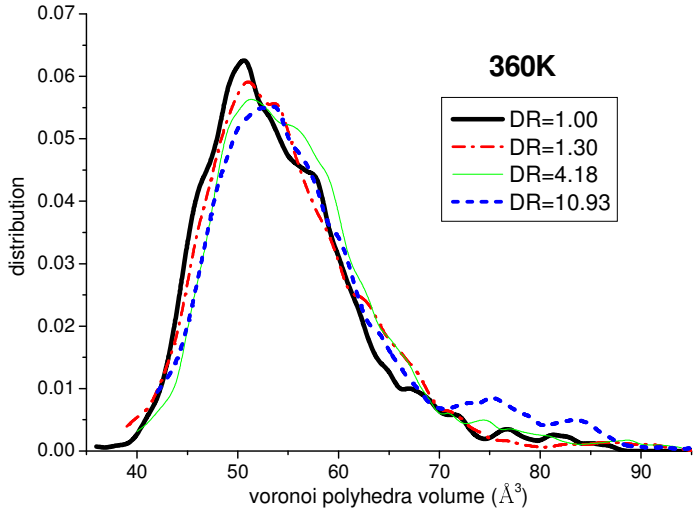

(b)

Figure 7-8 Voronoi polyhedron volume distribution for atoms at chain ends at (a) 250K and (b) 360K

7.5. Combined Effects of Temperature and Stretching

Since temperature and strain act on the free volume distribution in an opposite way, it is interesting to explore the combined effects of these two. The combined effect of orientation and temperature on free volume distribution was analyzed at different stretching level at four different temperatures. As shown in Figure 7-9, when the effect of temperature and stretch are combined, a redistribution of the size of free volume

occurs. One can see that at low strain levels (Figure 7-9 a and b), the distribution of free volume cavities depends on the temperature, while this dependence diminishes with increasing strain and finally the distribution becomes relatively independent of the temperature at high strain levels (Figure 7-9 c and d). It seems to indicate that as the molecular orientation is increased with increasing applied forces, the effect of temperature is not sufficient enough to overcome the entropic reduction induced by the applied force. It should be mentioned that strains are shown in terms of stretching time, as strains increases with stretching time in a pattern given in Table 7-4 and Table 7-5. Although materials at different temperatures deform at different levels, the general trend that the distribution is relatively independent of the temperature at high strains is reasonable.

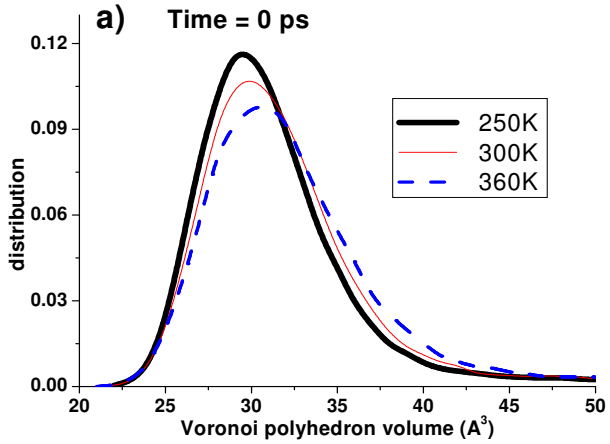

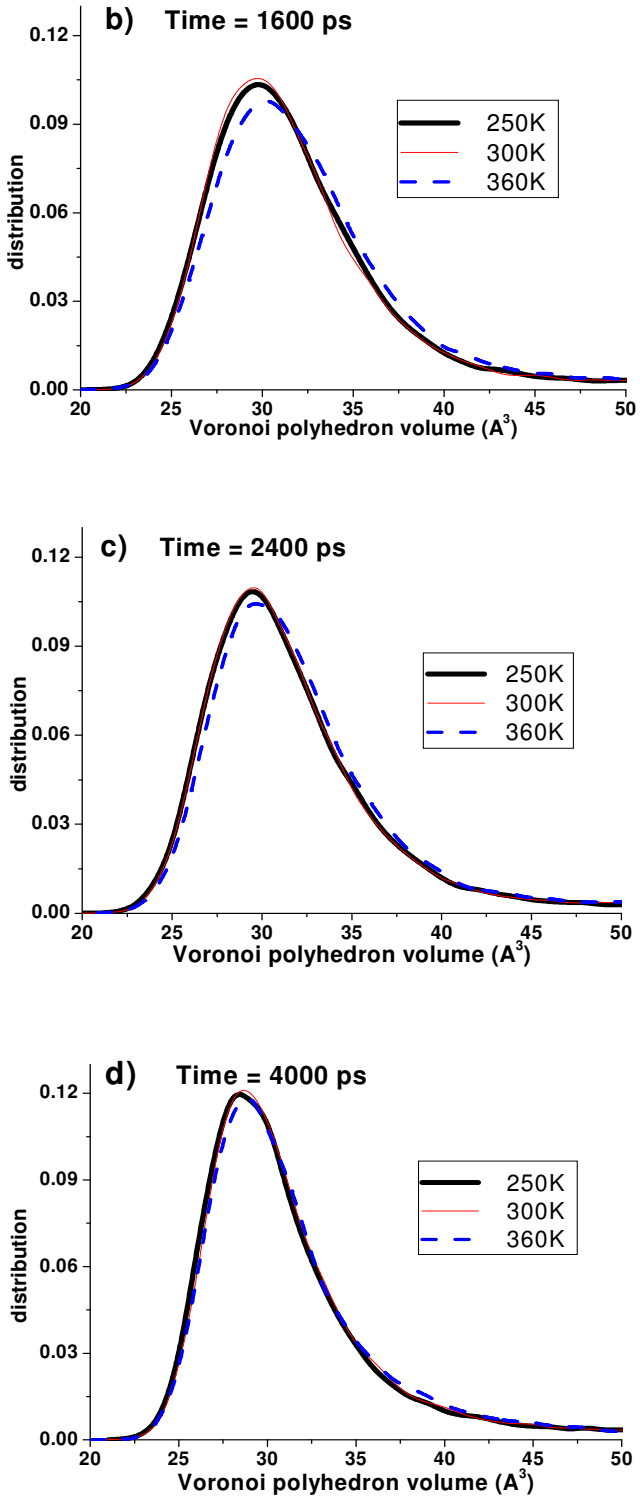

Figure 7-9 Rearrangement of free volume size distribution at different temperatures different strain levels: (a) 0 ps (b) 1600 ps (c) 2400 ps (d) 4000 ps.

Detailed classification of the size of free volume cavities with the number of such cavities for different strains and temperatures is listed in Table 7-4. A general pattern can be observed. The number of small cavities always decreases with strain. The number of medium sized holes initially increases and then decreases with larger strains. However, the number of larger cavities sometimes oscillates between high to low, especially at higher temperatures, but the general trend shows increasing cavity size with strain.

Table 7-4 Distribution of void size for different strains and temperatures (number/nm^3)

	Time	**0 ps**	**1600 ps**	**2400 ps**	**3200 ps**	**4000 ps**
250K	**DR**	**1.00**	**1.14**	**1.65**	**2.81**	**8.22**
	<= 5	9.155	8.759	8.560	7.639	5.783
	5 ~ 10	0.258	0.239	0.277	0.247	0.185
	10 ~ 20	0.125	0.167	0.197	0.192	0.154
	20 ~ 40	0.038	0.054	0.096	0.112	0.077
	40 ~ 60	0.002	0.006	0.022	0.022	0.021
	60 ~ 100	0	0.002	0.010	0.009	0.010
	> 100	0	0	0	0	0.001
270K	**DR**	**1.00**	**1.221**	**1.90**	**3.31**	**9.26**
	<= 5	9.565	9.450	8.499	7.594	5.607
	5 ~ 10	0.244	0.285	0.271	0.256	0.193
	10 ~ 20	0.125	0.170	0.220	0.194	0.141
	20 ~ 40	0.043	0.078	0.092	0.099	0.090
	40 ~ 60	0.006	0.007	0.020	0.024	0.024
	60 ~ 100	0	0.002	0.010	0.009	0.007
	> 100	0	0.001	0.001	0	0.001
300K *	**DR**	**1.00**	**1.18**	**1.84**	**3.21**	**8.99**
	<= 5	9.627	9.118	7.900	6.575	4.986
	5 ~ 10	0.267	0.303	0.257	0.228	0.166
	10 ~ 20	0.160	0.206	0.202	0.168	0.134
	20 ~ 40	0.057	0.111	0.101	0.087	0.072
	40 ~ 60	0.006	0.021	0.021	0.021	0.024
	60 ~ 100	0	0.007	0.008	0.008	0.015
	> 100	0	0	0.001	0.002	0.002
360K	**DR**	**1.00**	**1.30**	**2.30**	**4.18**	**10.93**
	< = 5	9.996	9.827	9.066	7.901	5.708
	5 ~ 10	0.304	0.302	0.289	0.245	0.191
	10 ~ 20	0.222	0.227	0.215	0.195	0.147
	20 ~ 40	0.113	0.133	0.133	0.112	0.088
	40 ~ 60	0.018	0.030	0.023	0.026	0.022
	60 ~ 100	0.009	0.013	0.017	0.007	0.014
	> 100	0.001	0.002	0.002	0	0

* Same as in Table 7-2.

The shape factors as well were analyzed at different strains and temperatures as shown in Table 7-5. As shown, there is no significant influence of temperature on the shape factor for various strain levels. With increasing orientation, more elongated larger voids are formed. However, the more elongated voids formed due to stretch does not remain intact from further stretch, especially at higher temperature.

Table 7-5 Shape factors of free volume voids at different strain and temperatures

	Time	**0 ps**	**1600 ps**	**2400 ps**	**3200 ps**	**4000 ps**
250K	**DR**	**1.00**	**1.14**	**1.65**	**2.81**	**8.22**
	<= 5	1.403	1.4004	1.395	1.398	1.394
	5 ~ 10	2.376	2.369	2.409	2.383	2.385
	10 ~ 20	2.616	2.646	2.602	2.592	2.547
	20 ~ 40	2.807	2.871	2.922	2.868	2.813
	40 ~ 60	3.209	3.161	3.108	3.043	3.197
	60 ~ 100	-	3.717	3.527	3.505	2.868
	> 100	-	-	-	-	2.503
270K	**DR**	**1.00**	**1.22**	**1.90**	**3.31**	**9.26**
	<= 5	1.408	1.404	1.390	1.395	1.334
	5 ~ 10	2.415	2.403	2.378	2.381	2.712
	10 ~ 20	2.630	2.618	2.615	2.582	2.954
	20 ~ 40	2.921	2.928	2.852	2.827	3.228
	40 ~ 60	2.845	3.128	3.232	3.108	3.551
	60 ~ 100	-	3.713	3.362	3.216	3.840
	> 100	-	4.1893	4.263	-	4.824
300K *	**DR**	**1.00**	**1.18**	**1.84**	**3.21**	**8.99**
	<= 5	1.402	1.397	1.396	1.396	1.394
	5 ~ 10	2.412	2.409	2.398	2.398	2.361
	10 ~ 20	2.663	2.579	2.626	2.622	2.558
	20 ~ 40	2.870	2.933	2.913	2.875	2.639
	40 ~ 60	3.494	3.221	3.186	2.997	3.059
	60 ~ 100	-	3.604	3.359	3.572	3.129
	> 100	-	-	4.476	3.540	4.748
360K	**DR**	**1.00**	**1.30**	**2.30**	**4.18**	**10.93**
	< = 5	1.391	1.388	1.389	1.397	1.391
	5 ~ 10	2.41	2.402	2.406	2.409	2.383
	10 ~ 20	2.652	2.652	2.662	2.621	2.579
	20 ~ 40	2.906	2.955	2.939	2.895	2.767
	40 ~ 60	3.346	3.304	3.425	3.139	2.963
	60 ~ 100	3.559	3.872	3.605	3.408	3.226
	> 100	4.314	4.096	4.145	-	-

* Same as in Table 7-3

CHAPTER 8

CONCLUSIONS & RECOMMENDATIONS

8.1. Conclusions

In this work, both experimental approach and computer simulation approach were applied to investigate the evolution of micro-structure in model polymer systems subjected to thermal, swelling and mechanical processes. Architecture-property-process relationship was examined and explored on the model polymeric systems with controllable architectures. The research carried out to date has led to a more thorough understanding of the effects of architecture at the molecular level on the macroscopic properties of polymeric materials.

8.1.1. Model Network Synthesis and Characterization

Monodispersed α, ω-diallyl PTHF precursors (both hydrogenated and deuterated) have been synthesized through cationic ring-opening living polymerization and terminated with allyl alcohol. The telechelic structure, functionality, molecular weight, and polydispersity were characterized with FTIR, Raman, GPC, chemical titration, NMR, MALDI and FAB-MASS spectroscopy. The results demonstrate that: 1) the precursors have the designed telechelic structure; 2) molecular weight of precursors was well controlled by varying reactant concentration and reaction temperature and precursors are nearly monodispersed in M_n distribution; 3) the absolute values of M_n were crosschecked through multiple characterization techniques and accurately determined. NMR turned out to be the most effective approach in determining M_n and was used in most of time.

Following the thiol-ene reaction mechanism, model PTHF networks have been synthesized by endlinking α, ω-diallyl PTHF precursors with stoichiometric amount of pentaerythritol tetrakis (3-mercaptopropionate), a tetrafunctional thiol crosslinker. By controlling the feeding ratio of short and long chain precursors, networks with unimodal and bimodal inter-crosslink chain length distribution were prepared at various crosslink density levels and inhomogeneity levels. Moreover, unique networks with clustered topology were designed and prepared through a two-step process. Different levels of inhomogeneity were designed and incorporated through controlling the "clustering time".

The completeness and efficiency of thiol-ene endlinking reaction was confirmed by the disappearance of -C=C groups in Raman spectra and by the low sol-fraction of final networks (less than 8 wt%). It is concluded that the chemical structure and the inter-crosslink chain length of the end-linked elastomers are known and well controlled.

8.1.2. Thermal Characteristics of Model PTHF Networks

Thermal characteristics of model PTHF Networks were comprehensively investigated as a function of crosslink density and the inhomogeneity of crosslink density distribution.

Increasing the crosslink density in the model networks increases the glass transition temperature and lowers the melting points and the enthalpy of fusion due to the crosslink junction confinement and the reduced flexibility of chain segments. The crosslinks in the model PTHF networks inhibits the crystallization of chain segments in the vicinity of the junction as indicated by the large decrease in enthalpy of heat compared with PTHF precursors. From the melting depression measurements, it was

estimated that 6 neighboring units and 5 units from crosslink were prevented from crystallization in unimodal and bimodal networks, respectively.

Inhomogeneity effect was investigated in three ways given same average inter-crosslink chain length: chain length distribution, short chain and long chain size ratio, and cluster size and cluster size distribution. All results shows that inhomogeneity in the crosslink distribution has little effect on the glass transition behavior. However, the heterogeneous network structure lowers the crystallinity of bimodal networks than that of unimodal ones with relatively homogeneous crosslink distribution. The supramolecular structure in bimodal networks depends not only on the input ratio of long chains and short chains but also on the size ratio of two kinds of chains. As for the clustered networks, it was found that cluster size and size distribution exerted a trivial influence on glass transition. However large cluster size in networks seemed to increase the melting temperature and decrease the crystallinity probably due to more defects introduced by the large clusters.

8.1.3. Freezing Behavior of Gel Solvent Confined in Model PTHF Networks

An experimental approach based on the freezing point depression of a solvent confined in a swollen gel has been developed to characterize the structure of model PTHF networks. Although it has been extensively used for the study of rigid materials, this thermoporosimetry technique has been successfully applied to polymeric gel media in this work, i.e., model PTHF networks with unimodal, bimodal and clustered topologies. The relationships between the pore size and the freezing point depression were obtained, providing a good reflection of the existing architecture facts in the networks.

The crosslinked elastomeric matrix, once the equilibrium swelling is reached, is comparable to a three-dimensional network with the size of the mesh depending on the crosslinking level. The higher the crosslinking level, the smaller the mesh size of the network. As a result, the magnitude of freezing point depression (FPD) decreased with increasing the inter-crosslink segment length, reflecting large gel solvent crystals formed in large meshes. FPD also shows dependence on the inhomogeneous distribution in crosslink density. For high crosslink density, bimodal distribution resulted in a higher depression in gel solvent freezing point than the unimodal distribution due to segregation of short chain precursors. While for low crosslink density, bimodal networks have higher freezing points (lower ΔT_f) than unimodal networks due to its more heterogeneous architecture. As for clustered network, a maximum value of ΔT_f was observed as a function of clustering time indicating that the freezing point depression depends on the size distribution of clusters as well as the size of clusters.

8.1.4. Uniaxial Deformation of Model PTHF Networks – SANS Studies

The small-angle neutron scattering spectra of uniaxially elongated swollen gels have been investigated as a function of the elongation ratio, λ, for three different types of PTHF model networks – unimodal, bimodal and clustered networks. The spatial inhomogeneities in crosslink distribution in bimodal and clustered networks gave rise to the formation of isointensity curves in the form of "*abnormal* butterfly patterns" on a 2D detector. The butterfly patterns became more pronounced as λ increases. Accordingly an increase in intensity was observed at small Q's in the direction parallel to elongation axis.

Quantitatively, the scattering intensity was measured as a function of λ in the directions parallel and perpendicular to the elongation axis. The radii of gyration were

calculated and the dependence of these quantities on the elongation ratio was compared to the predictions of three theoretical rubber elasticity models, namely (i) affine model, (ii) phantom model, and (iii) junction affine model.

The comparison between the experimental results and the behavior deduced from theoretical models does not allow an interpretation of the molecular deformation at the level of the mesh size within the framework of any single model among those proposed by the classical theories of rubber elasticity. Depending upon the length of the elementary chains, the description of the molecular response is achieved by taking into consideration more or less accentuated junction fluctuations and the network topologies. The increase in crosslink inhomogeneities moves the molecular deformation behavior of long chains from phantom deformation in unimodal network towards junction affine deformation in bimodal networks, and to affine deformation behavior in clustered networks. The short chains in bimodal networks assume more deformation than long chains especially at high strain level due to the limited extensibility accounting for the extraordinary mechanical properties of bimodal networks. However, in clustered networks long chains assume large portion of deformation rather than the clusters which deform as an entity other than individual short chains. As for cluster size effect, there is negligible influence observed on the elongation behavior of long chains.

8.1.5. MD Simulation of Free Volume Distribution of Model Linear Polymer

MD simulations coupled with hard sphere probe method and Voronoi tessellation technique were carried out in investigating the evolution of free volume and free volume distribution in polymer system subjected to external time-dependent changes.

In the undrawn state, the total free volume fraction increases slightly with an increase in temperature and a broader free volume size distribution was observed due to temperature elevation. For voids of given size, temperature change does not have much influence on the shape of these voids. While at a given temperature, the increase in the free volume size is accompanied with the increase in the shape factors, indicating that large free volume voids are more elliptical than the smaller ones.

In an opposite way, uniaxial stretching results in smaller mean size of free volume voids and narrower size distribution. The number of small free volume voids decreases fast with strain. The number of medium sized holes initially increases and then decreases with larger strains. However, the number of larger cavities shows increase with strain. Moreover the formation of extra large cavities (> 100 $Å^3$) was observed at high strain level. At any given strain, increasing cavity size is associated with increasing shape factor, indicating that larger voids are more elliptical than smaller ones.

More insight on the evolution of free volume distribution was provided under the combined effect of orientation and temperature. Upon stretching, the distribution of free volume cavities showed its dependence on the temperature at low strain levels, while this dependence diminishes with increasing strain and finally the distribution becomes relatively independent of the temperature at high strain levels. Simulation results showed that temperature does not have any significant effect on the pattern on free volume change associated with atoms at chain ends or away from chain ends. Also no significant influence of temperature is seen on the shape factor for various strain levels. As a general pattern, the total free volume initially increases slightly and then decrease with increasing axial strains for all three temperatures we studied, and the free volume associated with

atoms away from chain ends follow a similar pattern. For free volume cavities at chain ends, the effect of stretch is to shift the distribution towards larger cavities while temperature increase shifts the distribution slightly towards smaller cavity size. These simulations show that those large and more elliptical free volume voids during stretching are formed at chain ends.

8.2. Recommendations

8.2.1. Mapping the Inhomogeneities in Polymer Networks

The purpose of this recommended work is to provide a more direct view of the inhomogeneity, i.e., mapping the inhomogeneous crosslink distribution in the networks. Although various properties have been investigated as function of inhomogeneity and crosslink density, there is still no direct way to describe or quantify the inhomogeneity. One possible way out is to map the inhomogeneities in networks using Raman spectroscopy with single-wall carbon nano-tube (SWNT) as sensors.

It is well known that there are several characteristic Raman bands associated with SWNT, which are related to different Raman modes, like RBM band (radial breathing mode), G band (tangential mode, corresponds to the stretching mode), and disorder-induced D band. Especially it has been demonstrated [178-180] that a second-order overtone of D band called D* (or G') band located at ~ 2500-2700 cm^{-1} responds appropriately to indicate the strain (or stress) and transitions in polymers, which could in turn be quantified by means of Raman spectroscopy. The position of the D* Raman band of SWNTs is strongly dependent on the strain transferred from the polymer matrix to the nanotubes. When SWNTs are embedded in a polymer matrix, they are hydrostatically compressed and this shifts the wave number of the D* band upwards from 2610 cm^{-1} in

air to around 2628 cm^{-1}, depending on the polymer used. It is expected that SWNT located in different part of our model networks would have different interactions with polymer segments due to inhomogeneity in crosslink density and the differences would manifest themselves on the Raman shifts. In this way, it is possible to "map" the inhomogeneity in the model polymer networks providing the direct view.

Moreover, this type of application only needs a small amount of nanotubes (less than 0.5 wt% of nanotubes) and the sensitivity of the measurement can be at the micro-scale and molecular level. Therefore, to use nanotubes as functional materials might be a very effective but less expensive research avenue.

Of course there are some possible difficulties to be expected: 1) dispersion or compatibility of SWNT in polymer networks; 2) possible side effects of SWNT in the crosslinking process, which might disturb the architecture control of final polymer networks; 3) complicated interactions of SWNT with polymer matrix, which would make the explanation of Raman spectra very difficult.

8.2.2. PALS Measurements on Model PTHF Networks

Free volume and its distribution are important in determining properties like gas transportation/barrier, fiber dyeability etc. Many efforts have been taken on the free volume study on the linear polymer systems as reviewed in Chapter 2. However the study on the free volume and free volume distribution in crosslinked polymeric materials is very limited. How the crosslinking process and the inhomogeneities in the distribution of crosslinks would affect the free volume and free volume distribution in polymeric networks is still not clear. How total free volume fraction and free volume distribution evolve with external uniaxial strains has not been systematically studied yet, especially

on the crosslinked polymeric systems. Since the systems we studied are polymer networks with known structure, it would be possible to establish the exact relationship between the networks architectures and free volume and free volume distribution using PALS measurements. It is expected that the differences in network architecture would definitely give rise to the differences in free volume distribution due to the spatial inhomogeneities in the distribution of crosslink points. How these inhomogeneities affect the free volume and free volume distribution when networks are subjected to external time-dependent changes like temperature and strain is also an interesting and pioneering study in this field.

8.2.3. MD Simulations on Cyclic Polymers and Polymer Networks

In the present work, we have studied the evolution of free volume and free volume distribution of linear polymers subjected to uniaxial stretching and temperature changes through MD simulation coupled with hard sphere method and Voronoi tessellation method. It was shown that during uniaxial stretching, large and elliptical free volume voids are formed at polymer chain ends due to weaker interactions. Upon this finding, it would be interesting if one studies the free volume evolution of cyclic polymers, which have no free chain ends. It has been shown that cyclic copolymer membranes show attractive permeability values and ideal separation factors. The O_2/N_2 ideal selectivity was among the highest values reported by other authors using traditional membrane materials [181]. However, how this attractive behavior of cyclic polymers in gas transportation is related to the free volume and free volume distribution is not clear and has not been studied yet. The major difficulty of this recommended work would be the generation of initial configurations of cyclic chains.

Another work one can try to do is to study the free volume and free volume distribution of polymer networks with temperature and uniaxial stretching. It is generally believed that high crosslinking results in high macroscopic density, high stiffness and low penetrant absorption as in vulcanized rubbers. However, studies on crosslinked epoxy networks suggest that high crosslink density can actually lead to opposite results due to the poorer packing of molecules arising from constraints on the packing of molecules imposed by crosslinks. For example, Gupta *et al* [182] observed that epoxy resins with high crosslink density are in poor packing and thus have relatively higher free volume at and below T_g. However, it is very difficult to establish the relationship between the network structure and the free volume distribution through experimental approach due to many unknown factors in network micro-structure. While through MD technique, unambiguous network structure can be readily obtained through proper MD programs like LAMMPS, and free volume distribution can then be clearly extracted from instantaneous chain configurations. The possible difficulty in this work is the modification of the codes of hard sphere probe method and Voronoi method in order to make them feasible in analyzing network structures.

CHAPTER 9

REFERENCES

[1] B. Erman and J. E. Mark, "Calculations on trimodal elastomeric networks. Effects of chain length and composition on ultimate properties," *Macromolecules*, vol. 31, pp. 3099-3103, 1998.

[2] S. Besbes, L. Bokobza, L. Monnerie, I. Bahar, and B. Erman, "Molecular-Orientation in Deformed Bimodal Networks .2. Fourier-Transform Infrared Measurements on Poly(Dimethylsiloxane) Networks and Comparison with Theory," *Macromolecules*, vol. 28, pp. 231-235, 1995.

[3] M. A. Sharaf and J. E. Mark, "Interpretation of the Small-Strain Moduli of Model Networks of Polydimethylsiloxane," *Polymer*, vol. 35, pp. 740-751, 1994.

[4] M. A. Sharaf, J. E. Mark, and E. Ahmed, "Elastomeric Properties of End-Linked Networks of High Cross-Link Functionality - Accounting for Possible Changes in Effective Functionality with Extent of Reaction and Chain-Length Distribution," *Colloid and Polymer Science*, vol. 272, pp. 504-515, 1994.

[5] V. Galiatsatos, P. R. Subramanian, and L. Klein-Castner, "Designing heterogeneity into bimodal elastomeric PDMS networks," *Macromolecular Symposia*, vol. 171, pp. 97-104, 2001.

[6] E. E. Hamurcu and B. M. Baysal, "Interpenetrating Polymer Networks of Poly(Dimethylsiloxane) .1. Preparation and Characterization," *Polymer*, vol. 34, pp. 5163-5167, 1993.

[7] J. E. Mark, *Physical properties of polymers* 3rd ed. Cambridge ; New York: Cambridge University Press, 2004.

[8] Y. Gnanou, G. Hild, and P. Rempp, "Molecular-Structure and Elastic Behavior of Poly(Ethylene Oxide) Networks Swollen to Equilibrium," *Macromolecules*, vol. 20, pp. 1662-1671, 1987.

[9] S. J. Clarson, J. E. Mark, C. C. Sun, and K. Dodgson, "Effect of bimodal chain length distribution on the thermal characteristics of poly(ethylene oxide) end-linked networks," *European Polymer Journal*, vol. 28, pp. 823-825, 1992.

[10] Y. Gnanou, G. Hild, and P. Rempp, "Hydrophilic Polyurethane Networks Based on Poly(Ethylene Oxide) - Synthesis, Characterization, and Properties - Potential Applications as Biomaterials," *Macromolecules*, vol. 17, pp. 945-952, 1984.

[11] J. E. Mark and M. A. Llorente, "Model Networks of End-Linked Polydimethylsiloxane Chains .5. Dependence of the Elastomeric Properties on the Functionality of the Network Junctions," *Journal of the American Chemical Society*, vol. 102, pp. 632-636, 1980.

[12] M. Ilavsky and K. Dusek, "The Structure and Elasticity of Polyurethane Networks .1. Model Networks of Poly(Oxypropylene) Triols and Diisocyanate," *Polymer*, vol. 24, pp. 981-990, 1983.

[13] H. Goering, H. Kruger, and M. Bauer, "Multimodal polymer networks: design and characterisation of nanoheterogeneous PU elastomers," *Macromolecular Materials and Engineering*, vol. 278, pp. 23-35, 2000.

[14] M. K. Hassan, G. G. Abdel-Sadek, G. Beaucage, J. E. Mark, and M. A. Sharaf, "Sol-gel condensations to form polytetrahydrofuran networks and their elastomeric behavior," *Journal of Macromolecular Science-Pure and Applied Chemistry*, vol. A41, pp. 1-13, 2004.

[15] L. Jong and R. S. Stein, "Synthesis, Characterization, and Rubber Elasticity of End-Linked Poly(Tetrahydrofuran) Elastomer," *Macromolecules*, vol. 24, pp. 2323-2329, 1991.

[16] B. Erman and J. E. Mark, *Structures and properties of rubberlike networks*. New York: Oxford University Press, 1997.

[17] W. Wu, L. D. Coyne, L. Jong, A. Hanyu, and R. S. Stein, "Molecular-Structure of Bimodal Polymer Networks," *Macromolecules*, vol. 23, pp. 351-353, 1990.

[18] P. Weiss, G. Hild, J. Herz, and P. Rempp, "Preparation of Crosslinked Gels by Anionic Block-Copolymerization of Styrene and Divinylbenzene," *Makromolekulare Chemie*, vol. 135, pp. 249-&, 1970.

[19] K. Matyjaszewski, American Chemical Society. Division of Polymer Chemistry., and American Chemical Society. Meeting, *Advances in controlled/living radical polymerization*. Washington, DC; New York: American Chemical Society ; Distributed by Oxford University Press, 2003.

[20] F. Asgarzadeh, P. Ourdouillie, E. Beyou, and P. Chaumont, "Synthesis of polymer networks by "Living" free radical polymerization and end-linking processes," *Macromolecules*, vol. 32, pp. 6996-7002, 1999.

[21] G. Hild, R. Okasha, and P. Rempp, "Free-Radical Crosslinking Copolymerization in the Post-Gel State .3. Swelling and Mechanical-Properties of Polystyrene Networks," *Makromolekulare Chemie-Macromolecular Chemistry and Physics*, vol. 186, pp. 407-422, 1985.

[22] R. S. Stein, "Determination of Inhomogeneity of Crosslinking of a Rubber by Light Scattering," *Journal of Polymer Science Part B-Polymer Letters*, vol. 7, pp. 657-&, 1969.

[23] F. Bueche, "Light Scattering from Swollen Gels," *Journal of Colloid and Interface Science*, vol. 33, pp. 61-&, 1970.

[24] V. Soni and R. S. Stein, "The Preparation, Properties, and Scattering from Model Bimodal Poly (Dimethyl Siloxane) Networks," *Abstracts of Papers of the American Chemical Society*, vol. 190, pp. 173-POY, 1985.

[25] V. K. Soni and R. S. Stein, "Light-Scattering-Studies of Poly(Dimethylsiloxane) Solutions and Swollen Networks," *Macromolecules*, vol. 23, pp. 5257-5265, 1990.

[26] H. Oikawa, "Dynamic Light-Scattering Study on a Bimodal End-Linked Polydimethylsiloxane Network Structure," *Polymer*, vol. 33, pp. 1116-1119, 1992.

[27] K. Urayama, T. Kawamura, Y. Hirata, and S. Kohjiya, "SAXS study on poly(dimethylsiloxane) networks with controlled distributions of chain lengths between crosslinks," *Polymer*, vol. 39, pp. 3827-3833, 1998.

[28] N. C. B. Tan, B. J. Bauer, J. Plestil, J. D. Barnes, D. Liu, L. Matejka, K. Dusek, and W. L. Wu, "Network structure of bimodal epoxies - a small angle X-ray scattering study," *Polymer*, vol. 40, pp. 4603-4614, 1999.

[29] M. Shibayama, H. Takahashi, and S. Nomura, "Small-Angle Neutron-Scattering Study on End-Linked Poly(Tetrahydrofuran) Networks," *Macromolecules*, vol. 28, pp. 6860-6864, 1995.

[30] E. Mendes, B. Girard, C. Picot, M. Buzier, F. Boue, and J. Bastide, "Small-Angle Neutron-Scattering Study of End-Linked Gels," *Macromolecules*, vol. 26, pp. 6873-6877, 1993.

[31] J. Bastide, L. Leibler, and J. Prost, "Scattering by Deformed Swollen Gels - Butterfly Isointensity Patterns," *Macromolecules*, vol. 23, pp. 1821-1825, 1990.

[32] M. Beltzung, C. Picot, and J. Herz, "Investigation of the Chain Conformation in Uniaxially Stretched Poly(Dimethylsiloxane) Networks by Small-Angle Neutron-Scattering," *Macromolecules*, vol. 17, pp. 663-669, 1984.

[33] M. Beltzung, C. Picot, P. Rempp, and J. Herz, "Investigation of the Conformation of Elastic Chains in Poly(Dimethylsiloxane) Networks by Small-Angle Neutron-Scattering," *Macromolecules*, vol. 15, pp. 1594-1600, 1982.

[34] K. Saalwachter, "Detection of heterogeneities in dry and swollen polymer networks by proton low-field NMR spectroscopy," *Journal of the American Chemical Society*, vol. 125, pp. 14684-14685, 2003.

[35] K. Saalwachter, F. Kleinschmidt, and J. U. Sommer, "Swelling heterogeneities in end-linked model networks: A combined proton multiple-quantum NMR and computer simulation study," *Macromolecules*, vol. 37, pp. 8556-8568, 2004.

[36] H. Aoki, S. Tanaka, S. Ito, and M. Yamamoto, "Nanometric inhomogeneity of polymer network investigated by scanning near-field optical microscopy," *Macromolecules*, vol. 33, pp. 9650-9656, 2000.

[37] J. Bastide and L. Leibler, "Large-Scale Heterogeneities in Randomly Cross-Linked Networks," *Macromolecules*, vol. 21, pp. 2647-2649, 1988.

[38] S. K. Sukumaran, G. Beaucage, J. E. Mark, and B. Viers, "Neutron scattering from equilibrium-swollen networks," *European Physical Journal E*, vol. 18, pp. 29-36, 2005.

[39] T. A. Vilgis, "Rubber Elasticity and Inhomogeneities in Cross-Link Density," *Macromolecules*, vol. 25, pp. 399-403, 1992.

[40] J. U. Sommer and S. Lay, "Topological structure and nonaffine swelling of bimodal polymer networks," *Macromolecules*, vol. 35, pp. 9832-9843, 2002.

[41] A. Hanyu and R. S. Stein, "Segmental Orientation and Infrared Dichroism of Model Bimodal Elastomeric Networks," *Makromolekulare Chemie-Macromolecular Symposia*, vol. 45, pp. 189-203, 1991.

[42] S. Besbes, I. Cermelli, L. Bokobza, L. Monnerie, I. Bahar, B. Erman, and J. Herz, "Segmental Orientation in Model Networks of Poly(Dimethylsiloxane) - Fourier-

Transform Infrared Dichroism Measurements and Theoretical Interpretation," *Macromolecules*, vol. 25, pp. 1949-1954, 1992.

[43] M. Tosaka, S. Murakami, S. Poompradub, S. Kohjiya, Y. Ikeda, S. Toki, I. Sics, and B. S. Hsiao, "Orientation and crystallization of natural rubber network as revealed by WAXD using synchrotron radiation," *Macromolecules*, vol. 37, pp. 3299-3309, 2004.

[44] S. Toki, I. Sics, S. F. Ran, L. Z. Liu, B. S. Hsiao, S. Murakami, M. Tosaka, S. Kohjiya, S. Poompradub, Y. Ikeda, and A. H. Tsou, "Strain-induced molecular orientation and crystallization in natural and synthetic rubbers under uniaxial deformation by in-situ synchrotron X-ray study," *Rubber Chemistry and Technology*, vol. 77, pp. 317-335, 2004.

[45] H. Menge, W. Pyckhout-Hintzen, G. Meier, and E. Straube, "Butadiene rubbers: topological constraints and microscopic deformation by mechanical and small angle neutron scattering investigation " *Polymer Bulletin*, vol. 48, pp. 183-190, 2002.

[46] A. K. Doolittle, "Studies in Newtonian Flow .1. The Dependence of the Viscosity of Liquids on Temperature," *Journal of Applied Physics*, vol. 22, pp. 1031-1035, 1951.

[47] A. K. Doolittle, *The Technology of Solvent and Plasticizers,*. New York: New York, Wiley, 1954.

[48] A. K. Doolittle, "Studies in Newtonian Flow .2. The Dependence of the Viscosity of Liquids on Free-Space," *Journal of Applied Physics*, vol. 22, pp. 1471-1475, 1951.

[49] A. K. Doolittle and D. B. Doolittle, "Studies in Newtonian Flow .5. Further Verification of the Free-Space Viscosity Equation," *Journal of Applied Physics*, vol. 28, pp. 901-905, 1957.

[50] K. Binder, J. Baschnagel, and W. Paul, "Glass transition of polymer melts: test of theoretical concepts by computer simulation," *Progress in Polymer Science*, vol. 28, pp. 115-172, 2003.

[51] R. E. Robertson, R. Simha, and J. G. Curro, "Free-Volume and the Kinetics of Aging of Polymer Glasses," *Macromolecules*, vol. 17, pp. 911-919, 1984.

[52] Y. Huang, X. Wang, and D. R. Paul, "Physical aging of thin glassy polymer films: Free volume interpretation," *Journal of Membrane Science*, vol. 277, pp. 219-229, 2006.

[53] S. Mondal, J. L. Hu, and Z. Yong, "Free volume and water vapor permeability of dense segmented polyurethane membrane," *Journal of Membrane Science*, vol. 280, pp. 427-432, 2006.

[54] A. Thran, G. Kroll, and F. Faupel, "Correlation between fractional free volume and diffusivity of gas molecules in classy polymers," *Journal of Polymer Science Part B-Polymer Physics*, vol. 37, pp. 3344-3358, 1999.

[55] J. F. Kincaid and H. Eyring, "Free volumes and free angle ratios of molecules in liquids," *Journal of Chemical Physics*, vol. 6, pp. 620-629, 1938.

[56] A. Bondi, "Free Volumes and Free Rotation in Simple Liquids and Liquid Saturated Hydrocarbons," *Journal of Physical Chemistry*, vol. 58, pp. 929-939, 1954.

[57] R. N. Haward, H. Breuer, and G. Rehage, "The free volume of polystyrene," *Journal of Polymer Science Part B: Polymer Letters*, vol. 4, pp. 375-378, 1966.

[58] A. Bondi, "Packing Density of Polymer Melts near Glass Transition Temperature," *Journal of Polymer Science Part a-General Papers*, vol. 2, pp. 3159-3165, 1964.

[59] R. N. Haward, "Occupied Volume of Liquids and Polymers," *Journal of Macromolecular Science-Reviews in Macromolecular Chemistry*, vol. C 4, pp. 191-242, 1970.

[60] Y. Kobayashi, "Quenching of Positronium Atoms by Nitrobenzene in Various Solutions," *Journal of the Chemical Society-Faraday Transactions*, vol. 87, pp. 3641-3645, 1991.

[61] Y. Kobayashi, K. Haraya, Y. Kamiya, and S. Hattori, "Correlation between the ortho-Positronium Pick-off Annihilation Lifetime and the Free Volume in Molecular Liquids and Polymers," *Bulletin of the Chemical Society of Japan*, vol. 65, pp. 160-162, 1992.

[62] Y. Kobayashi, W. Zheng, E. F. Meyer, J. D. Mcgervey, A. M. Jamieson, and R. Simha, "Free-Volume and Physical Aging of Polyvinyl Acetate) Studied by Positron-Annihilation," *Macromolecules*, vol. 22, pp. 2302-2306, 1989.

[63] H. Nakanishi, S. J. Wang, and Y. C. Jean, *International Symposium on Positron Annihilation Studies of Fluids*. Arlington, Texas: World Scientific, Singapore, 1987.

[64] R. A. Pethrick, "Positron annihilation--A probe for nanoscale voids and free volume?," *Progress in Polymer Science*, vol. 22, pp. 1-47, 1997.

[65] Y. C. Jean, "Free-Volume Mean Sizes of Polymers Probed by Positron-Annihilation Spectroscopy - a Correlation of Results Obtained by Pal and by Acar Methods," *Nuclear Instruments & Methods in Physics Research Section B-Beam Interactions with Materials and Atoms*, vol. 56-7, pp. 615-617, 1991.

[66] H. Nakanishi and Y. C. Jean, *Positron and Positronium Chemistry*. New York: Elsevier, 1988.

[67] M. Kryszewski, "Free volume from the view point of positron annihilation life time spectroscopy and small angle X-ray scattering," *Proceedings of SPIE*, vol. 4240, pp. 1-6, 2000.

[68] R. B. Gregory and Y. K. Zhu, "Analysis of Positron-Annihilation Lifetime Data by Numerical Laplace Inversion with the Program Contin," *Nuclear Instruments & Methods in Physics Research Section a-Accelerators Spectrometers Detectors and Associated Equipment*, vol. 290, pp. 172-182, 1990.

[69] P. C. Jain, Bhatnaga.S, and A. Gupta, "Positron-Annihilation in Some High Polymers," *Journal of Physics Part C Solid State Physics*, vol. 5, pp. 2156-&, 1972.

[70] E. E. Abdel-Hady, "Positron annihilation lifetime study of irradiated and deformed low density polyethylene," *Polymer Degradation and Stability*, vol. 80, pp. 363-368, 2003.

[71] G. Dlubek, T. Lupke, H. M. Fretwell, M. A. Alam, A. Wutzler, and H. J. Radusch, "The local free volume in deformed polyethylene: a positron lifetime study," *Acta Polymerica*, vol. 49, pp. 236-243, 1998.

[72] J. H. Lind, P. L. Jones, and G. W. Pearsall, "A Positron-Annihilation Lifetime Study of Isotactic Polypropylene," *Journal of Polymer Science Part a-Polymer Chemistry*, vol. 24, pp. 3033-3047, 1986.

[73] J. Liu, Q. Deng, and Y. C. Jean, "Free-Volume Distributions of Polystyrene Probed by Positron-Annihilation - Comparison with Free-Volume Theories," *Macromolecules*, vol. 26, pp. 7149-7155, 1993.

[74] R. M. Dammert, S. L. Maunu, F. H. J. Maurer, I. M. Neelov, S. Niemela, F. Sundholm, and C. Wastlund, "Free Volume and Tacticity in Polystyrenes," *Macromolecules*, vol. 32, pp. 1930-1938, 1999.

[75] D. Lin, B. Wang, X. H. Li, and S. J. Wang, *Mater. Sci. Forum*, vol. 105-110, pp. 1637-1640, 1992.

[76] B. D. Malhotra and R. A. Pethrick, "Positron-Annihilation Studies of the Glass Rubber Transition in Poly(Alkyl Methacrylates)," *Macromolecules*, vol. 16, pp. 1175-1179, 1983.

[77] R. M. Hodge, T. J. Bastow, G. H. Edward, G. P. Simon, and A. J. Hill, "Free volume and the mechanism of plasticization in water-swollen poly(vinyl alcohol)," *Macromolecules*, vol. 29, pp. 8137-8143, 1996.

[78] V. Ravindrachary, A. Chandrashekara, H. R. Sreepad, V. Sreeramalu, C. Ranganathaiah, and S. Gopal, "Positron Lifetime Study of the Free-Volume Properties in the Polymer Polyacrylonitrile," *Physics Letters A*, vol. 174, pp. 428-432, 1993.

[79] J. Borek and W. Osoba, "Influence of the plasticization on free volume in polyvinyl chloride," *Journal of Polymer Science Part B-Polymer Physics*, vol. 36, pp. 1839-1845, 1998.

[80] G. Dlubek, F. Redmann, and R. Krause-Rehberg, "Humidity-induced plasticization and antiplasticization of polyamide 6: A positron lifetime study of the local free volume," *Journal of Applied Polymer Science*, vol. 84, pp. 244-255, 2002.

[81] B. Wang, Z. F. Wang, M. Zhang, W. H. Liu, and S. J. Wang, "Effect of temperature on the free volume in glassy poly(ethylene terephthalate)," *Macromolecules*, vol. 35, pp. 3993-3996, 2002.

[82] H. S. Sodaye, P. K. Pujari, A. Goswami, and S. B. Manohar, "Measurement of free-volume hole size distribution in Nafion-117 using positron annihilation spectroscopy," *Journal of Polymer Science Part B-Polymer Physics*, vol. 36, pp. 983-989, 1998.

[83] B. D. Malhotra and R. A. Pethrick, "Positronium annihilation studies of polycarbonate, polyethersulphone and polysulphone," *European Polymer Journal*, vol. 19, pp. 457-459, 1983.

[84] M. Y. Ruan, H. Moaddel, A. M. Jamieson, R. Simha, and J. D. McGervey, "Positron-Annihilation Lifetime Studies of Free-Volume Changes in Polycarbonate under Static Tensile Deformation," *Macromolecules*, vol. 25, pp. 2407-2411, 1992.

[85] J. Barto, J. Kristiak, O. Sausa, P. Bandzuch, and J. Zrubcová, "Experimental free volume aspects of the polymer rheology as obtained by positron annihilation lifetime spectroscopy," *Macromolecular Symposia*, vol. 158, pp. 111-124, 2000.

[86] H. Nakanishi, Y. C. Jean, E. G. Smith, and T. C. Sandreczki, "Positronium formation at free-volume sites in the amorphous regions of semicrystalline PEEK," *Journal of Polymer Science Part B: Polymer Physics*, vol. 27, pp. 1419-1424, 1989.

[87] J. Kruse, J. Kanzow, K. Ratzke, F. Faupel, M. Heuchel, J. Frahn, and D. Hofmann, "Free volume in polyimides: Positron annihilation experiments and molecular modeling," *Macromolecules*, vol. 38, pp. 9638-9643, 2005.

[88] G. Dlubek, D. J. P. Udayan, N. Yu, A. M. Edelmann;, and R. Krause-Rehberg, "Temperature Dependence of Free Volume in Pure and Silica-Filled Poly(dimethyl siloxane) from Positron Lifetime and PVT Experiments," *Macromolecular Chemistry and Physics*, vol. 206, pp. 827-840, 2005.

[89] Q. Deng and Y. C. Jean, "Free-Volume Distributions of an Epoxy Polymer Probed by Positron-Annihilation - Pressure-Dependence," *Macromolecules*, vol. 26, pp. 30-34, 1993.

[90] V. P. Shantarovich, Y. P. Yampolskii, and I. B. Kevdina, "Free-Volume and Positronium Lifetime in Polymer Systems," *High Energy Chemistry*, vol. 28, pp. 41-46, 1994.

[91] V. P. Shantarovich, I. B. Kevdina, Y. P. Yampolskii, and A. Y. Alentiev, "Positron Annihilation Lifetime Study of High and Low Free Volume Glassy Polymers: Effects of Free Volume Sizes on the Permeability and Permselectivity," *Macromolecules*, vol. 33, pp. 7453-7466, 2000.

[92] Z. Yu, J. D. McGervey, A. M. Jamieson, and R. Simha, "Can Positron-Annihilation Lifetime Spectroscopy Measure the Free-Volume Hole Size Distribution in Amorphous Polymers," *Macromolecules*, vol. 28, pp. 6268-6272, 1995.

[93] J. J. Curro and R.-J. Roe, "Isothermal relaxation of specific volume and density fluctuation in poly(methyl methacrylate) and polycarbonate," *Polymer*, vol. 25, pp. 1424-1430, 1984.

[94] R. J. Roe and J. J. Curro, "Small-Angle X-Ray-Scattering Study of Density Fluctuation in Polystyrene Annealed Below the Glass-Transition Temperature," *Macromolecules*, vol. 16, pp. 428-434, 1983.

[95] R. J. Roe and H. H. Song, "Isothermal Relaxation of Volume and Density Fluctuation of Polystyrene Glass Prepared under Elevated Pressure," *Macromolecules*, vol. 18, pp. 1603-1609, 1985.

[96] H. H. Song and R. J. Roe, "Structural-Change Accompanying Volume Change in Amorphous Polystyrene as Studied by Small and Intermediate Angle X-Ray-Scattering," *Macromolecules*, vol. 20, pp. 2723-2732, 1987.

[97] Y. Tanabe, N. Muller, and E. W. Fischer, "Density Fluctuation in Amorphous Polymers by Small-Angle X-Ray-Scattering," *Polymer Journal*, vol. 16, pp. 445-452, 1984.

[98] H. Itagaki, K. Horie, and I. Mita, "Luminescent probe studies of the microstructure and mobility of solid polymers," *Progress in Polymer Science*, vol. 15, pp. 361-424, 1990.

[99] Z. G. Gardlund, "Effect of a polymer matrix on photochromism of some benzospirans," *Journal of Polymer Science Part B: Polymer Letters*, vol. 6, pp. 57-61, 1968.

[100] W. J. Priest and M. M. Sifain, "Photochemical and thermal isomerization in polymer matrices: Azo compounds in polystyrene," *Journal of Polymer Science Part A-1: Polymer Chemistry*, vol. 9, pp. 3161-3168, 1971.

[101] C. S. P. Sung, I. R. Gould, and N. J. Turro, "Pulsed Laser Spectroscopic Study of the Photoisomerization of Azo Labels at 3 Different Locations on a Polystyrene Chain," *Macromolecules*, vol. 17, pp. 1447-1451, 1984.

[102] C. S. P. Sung, L. Lamarre, and K. H. Chung, "Use of Azochromophoric Labels as a Molecular Probe of Physical Aging in Amorphous Polymers," *Macromolecules*, vol. 14, pp. 1839-1841, 1981.

[103] W. C. Yu and C. S. P. Sung, "Mobility and the Distribution of Free-Volume in Epoxy Network by Photochromic Labeling and Probe Studies," *Macromolecules*, vol. 21, pp. 365-371, 1988.

[104] W. C. Yu, C. S. P. Sung, and R. E. Robertson, "Site-Specific Labeling and the Distribution of Free-Volume in Glassy Polystyrene," *Macromolecules*, vol. 21, pp. 355-364, 1988.

[105] J. G. Victor and J. M. Torkelson, "On measuring the distribution of local free volume in glassy polymers by photochromic and fluorescence " *Macromolecules*, vol. 20, pp. 2241-2250, 1987.

[106] J. G. Victor and J. M. Torkelson, "Photochromic and fluorescent probe studies in glassy polymer matrices. 3. Effects of physical aging and molar weight on the size distribution of local free volume in polystyrene," *Macromolecules*, vol. 21, pp. 3490-3497, 1988.

[107] R. O. Loutfy, "Fluorescence Probes for Polymer Free-Volume," *Pure and Applied Chemistry*, vol. 58, pp. 1239-1248, 1986.

[108] T. Kondo, K. Yoshii, K. Horie, and M. Itoh, "Photoprobe Study of Siloxane Polymers. 3. Local Free Volume of Polymethylsilsesquioxane Probed by Photoisomerization of Azobenzene," *Macromolecules*, vol. 33, pp. 3650-3658, 2000.

[109] Y. P. Yampolskii, N. E. Kaliuzhnyi, and S. G. Durgarjan, "Thermodynamics of Sorption in Glassy Poly(vinyltrimethylsi1ane)," *Macromolecules*, vol. 19, pp. 846-850, 1986.

[110] A. Y. Alentiev, V. P. Shantarovich, T. C. Merkel, V. I. Bondar, B. D. Freeman, and Y. P. Yampolskii, "Gas and Vapor Sorption, Permeation, and Diffusion in Glassy Amorphous Teflon AF1600," *Macromolecules*, vol. 35, pp. 9513-9522, 2002.

[111] Y. P. Yampolskii, S. A. Soloviev, and M. L. Gringolts, "Thermodynamics of sorption in and free volume of poly (5,6-bis(trimethylsilyl)norbornene)," *Polymer*, vol. 45, pp. 6945-6952, 2004.

[112] T. L. Smith, A. H. Chan, W. Oppermann, and G. Levita, "Gas-Transport in a Glassy Polymer Subjected to Static Tensile Strains," *Abstracts of Papers of the American Chemical Society*, vol. 185, pp. 2-Poly, 1983.

[113] Y. P. Yampolskii, M. V. Motyakin, A. M. Wasserman, T. Masuda, M. Teraguchi, V. S. Khotimskii, and B. D. Freeman, "Study of high permeability polymers by means of the spin probe technique," *Polymer*, vol. 40, pp. 1745-1752, 1999.

[114] D. Rigby and R. J. Roe, "Molecular-Dynamics Simulation of Polymer Liquid and Glass .1. Glass-Transition," *Journal of Chemical Physics*, vol. 87, pp. 7285-7292, 1987.

[115] D. Rigby and R. J. Roe, "Molecular-Dynamics Simulation of Polymer Liquid and Glass .2. Short-Range Order and Orientation Correlation," *Journal of Chemical Physics*, vol. 89, pp. 5280-5290, 1988.

[116] D. Rigby and R. J. Roe, "Molecular-Dynamics Simulation of Polymer Liquid and Glass .3. Chain Conformation," *Macromolecules*, vol. 22, pp. 2259-2264, 1989.

[117] P. in't Veld, M. Stone, T. Truskett, and I. Sanchez, "Liquid Structure via Cavity Size Distributions," *J. Phys. Chem. B*, vol. 104, pp. 12028-12034, 2000.

[118] M. Rubinstein and R. H. Colby, *Polymer Physics*, 1 ed. New York: Oxford University Press, 2003.

[119] M. Vacatello, G. Avitabile, P. Corradini, and A. Tuzi, "A Computer-Model of Molecular Arrangement in a N-Paraffinic Luquid," *Journal of Chemical Physics*, vol. 73, pp. 548-552, 1980.

[120] D. N. Theodorou and U. W. Suter, "Detailed Molecular-Structure of a Vinyl Polymer Glass," *Macromolecules*, vol. 18, pp. 1467-1478, 1985.

[121] D. N. Theodorou and U. W. Suter, "Geometrical Considerations in Model Systems with Periodic Boundaries," *Journal of Chemical Physics*, vol. 82, pp. 955-966, 1985.

[122] V. M. Shah, S. A. Stern, and P. J. Ludovice, "Estimation of the free volume in polymers by means of a Monte Carlo technique," *Macromolecules*, vol. 22, pp. 4660-4662, 1989.

[123] S. Trohalaki, L. C. DeBolt, J. E. Mark, and H. L. Frisch, "Estimation of free volume for gaseous penetrants in elastomeric membranes by Monte Carlo simulations," *Macromolecules*, vol. 23, pp. 813 -816, 1990.

[124] T. S. Chow, "Free volume distributions in amorphous polymers," *Macromolecular Theory and Simulations*, vol. 4, pp. 397-404, 1995.

[125] S. Rane and P. D. Gujrati, "Importance of interactions for free-volume and end-group effects in polymers: An equilibrium lattice investigation," *Physical Review E*, vol. 64, pp. 011801, 2001.

[126] T. S. Chow, "Kinetics of free volume and physical aging in polymer glasses," *Macromolecules*, vol. 17, pp. 2336-2340, 1984.

[127] H. Meerwein, D. Delfs, and H. Morschel, "Polymerization of Tetrahydrofuran," *Angewandte Chemie-International Edition*, vol. 72, pp. 927-934, 1960.

[128] F. Dhaese, E. J. Goethals, Y. Tezuka, and K. Imai, "Synthesis and Reactions of Macromolecular Polytetrahydrofuran Azoinitiators," *Makromolekulare Chemie-Rapid Communications*, vol. 7, pp. 165-170, 1986.

[129] E. J. Goethals, "Telechelic Polymers by Cationic Ring-Opening Polymerization," *Makromolekulare Chemie-Macromolecular Symposia*, vol. 6, pp. 53-66, 1986.

[130] S. Siggia and J. G. Hanna, *Quantitative organic analysis via functional groups*. New York: Wiley, 1963.

[131] S. Boileau, B. Mazeaud-Henri, and R. Blackborow, "Reaction of functionalised thiols with oligoisobutenes via free-radical addition.: Some new routes to thermoplastic crosslinkable polymers," *European Polymer Journal*, vol. 39, pp. 1395-1404, 2003.

[132] N. B. Cramer, J. P. Scott, and C. N. Bowman, "Photopolymerizations of Thiol-Ene Polymers without Photoinitiators," *Macromolecules*, vol. 35, pp. 5361-5365, 2002.

[133] N. B. Cramer, T. Davies, A. K. O'Brien, and C. N. Bowman, "Mechanism and Modeling of a Thiol-Ene Photopolymerization," *Macromolecules*, vol. 36, pp. 4631-4636, 2003.

[134] J. P. Kennedy and J. Lackey, "Synthesis, Characterization, and Properties of Novel Polyisobutylene-Based Urethane Model Networks," *Journal of Applied Polymer Science*, vol. 33, pp. 2449-2465, 1987.

[135] J. M. Charlesworth, "The Glass-Transition Temperature for Non-Gaussian Network Polymers," *Journal of Macromolecular Science-Physics*, vol. B26, pp. 105-133, 1987.

[136] G. S. Trick and J. M. Ryan, "Crystallization of High Molecular Weight Poly(Tetramethylene Oxide) and Related Polymers," *Journal of Polymer Science Part C-Polymer Symposium*, pp. 93-&, 1967.

[137] L. Mandelkern, *Crystallization of Polymers*. New York: McGraw Hill, 1964.

[138] J. D. Hoffman and J. J. Weeks, "Melting Process and Equilibrium Melting Temperature of Polychlorotrifluoroethylene," *Journal of Research of the National Bureau of Standards Section a-Physics and Chemistry*, vol. 66, pp. 13-&, 1962.

[139] P. J. Flory, "Theory of Crystallization in Copolymers," *Transactions of the Faraday Society*, vol. 51, pp. 848-857, 1955.

[140] C. M. Roland and G. S. Buckley, "Thermal Crystallization of Polytetrahydrofuran Networks," *Rubber Chemistry and Technology*, vol. 64, pp. 74-82, 1991.

[141] J. Brandrup and E. H. Immergut, *Polymer Handbook*, 3rd ed. New York: Wiley, 1989.

[142] W. Kuhn and H. Majer, "Normal and Anomalous Freezingpoint Lowering," *Angewandte Chemie-International Edition*, vol. 68, pp. 345-349, 1956.

[143] S. Katayama and S. Fujiwara, "NMR-Study of the Spatial Effect of Polyacrylamide-Gel Upon the Water-Molecules Confined in It," *Journal of the American Chemical Society*, vol. 101, pp. 4485-4488, 1979.

[144] S. Katayama and S. Fujiwara, "NMR-Study of the Freezing-Thawing Mechanism of Water in Polyacrylamide-Gel," *Journal of Physical Chemistry*, vol. 84, pp. 2320-2325, 1980.

[145] B. B. Boonstra, F. A. Heckman, and G. L. Taylor, "Anomalous Freezing Point Depression of Swollen Gels," *Journal of Applied Polymer Science*, vol. 12, pp. 223-&, 1968.

[146] H. Oikawa and K. Murakami, "Studies of the Network Structure of Rubber Vulcanizates by a Cryoscopic Method .1.," *Polymer*, vol. 25, pp. 225-229, 1984.

[147] H. Oikawa and K. Murakami, "Studies of the Network Structure of Rubber Vulcanizates by Cryoscopic Methods .2.," *Polymer*, vol. 25, pp. 1117-1121, 1984.

[148] J. H. A. Grobler and W. J. Mcgill, "Anomalous Freezing-Point Depression of Solvents in a Swollen Homogeneous Rubber Network," *Journal of Polymer Science Part B-Polymer Physics*, vol. 31, pp. 575-577, 1993.

[149] D. Honiball, M. G. Huson, and W. J. Mcgill, "A Nucleation Theory for the Anomalous Freezing-Point Depression of Solvents in Swollen Rubber Gels," *Journal of Polymer Science Part B-Polymer Physics*, vol. 26, pp. 2413-2431, 1988.

[150] M. Baba, J. M. Nedelec, J. Lacoste, J. L. Gardette, and M. Morel, "Crosslinking of elastomers resulting from ageing: use of thermoporosimetry to characterise the polymeric network with n-heptane as condensate," *Polymer Degradation and Stability*, vol. 80, pp. 305-313, 2003.

[151] W. L. Wu and B. J. Bauer, "Epoxy Network Structure .3. Neutron-Scattering Study of Epoxies Containing Monomers of Different Molecular-Weight," *Macromolecules*, vol. 19, pp. 1613-1618, 1986.

[152] A. F. Guinier, Gerard., *Small-Angle Scattering of X-rays.* New York: John Wiley & Sons, 1955.

[153] F. Boué, J. Bastide, M. Buzier, C. Collette, A. Lapp, and J. Herz, "Dynamics of permanent and temporary networks: Small angle neutron scattering measurements and related remarks on the classical models of rubber deformation," in *Permanent and Transient Networks*, 1987, pp. 152-170.

[154] H. M. James and E. Guth, "Theory of the Increase in Rigidity of Rubber during Cure," *The Journal of Chemical Physics*, vol. 15, pp. 669-683, 1947.

[155] H. M. James and E. Guth, "Statistical Thermodynamics of Rubber Elasticity," *The Journal of Chemical Physics*, vol. 21, pp. 1039-1049, 1953.

[156] D. S. Pearson, "Scattered Intensity from a Chain in a Rubber Network," *Macromolecules*, vol. 10, pp. 696-701, 1977.

[157] M. H. Wagner, "Analysis of Small-Angle Neutron Scattering Data on Poly(dimethylsiloxane) Network Unfolding," *Macromolecules*, vol. 27, pp. 5223-5226, 1994.

[158] E. Mendes, R. Oeser, C. Hayes, F. Boue, and J. Bastide, "Small-Angle Neutron Scattering Study of Swollen Elongated Gels: Butterfly Patterns," *Macromolecules*, vol. 29, pp. 5574-5584, 1996.

[159] C. Rouf, J. Bastide, J. M. Pujol, F. Schosseler, and J. P. Munch, "Strain Effect on Quasistatic Fluctuations in a Polymer Gel," *Physical Review Letters*, vol. 73, pp. 830, 1994.

[160] A. Onuki, "Scattering from deformed swollen gels with heterogeneities," *Journal de Physique II*, vol. 2, pp. 45, 1992.

[161] A. Onuki, "Theory of phase transition in polymer gels," *Advances in Polymer Science*, vol. 109, pp. 63-121, 1993.

[162] R. Ullman, "Small-angle neutron scattering from elastomeric networks. Junction fluctuations and network unfolding," *Macromolecules*, vol. 15, pp. 582-588, 1982.

[163] R. Ullman, "Small-angle neutron scattering from elastomeric networks. Application to labeled chains containing several crosslinks," *Macromolecules*, vol. 15, pp. 1395-1402, 1982.

[164] D. Brown and J. H. R. Clarke, "Molecular-Dynamics Simulation of an Amorphous Polymer under Tension .1. Phenomenology," *Macromolecules*, vol. 24, pp. 2075-2082, 1991.

[165] H. J. C. Berendsen, J. P. M. Postma, W. F. Vangunsteren, A. Dinola, and J. R. Haak, "Molecular-Dynamics with Coupling to an External Bath," *Journal of Chemical Physics*, vol. 81, pp. 3684-3690, 1984.

[166] D. Brown, J. H. R. Clarke, M. Okuda, and T. Yamazaki, "The Preparation of Polymer Melt Samples for Computer-Simulation Studies," *Journal of Chemical Physics*, vol. 100, pp. 6011-6018, 1994.

[167] S. Misra and W. L. Mattice, "Atomistic Models of Amorphous Polybutadienes .3. Static Free-Volume," *Macromolecules*, vol. 26, pp. 7274-7281, 1993.

[168] E. G. Kim, S. Misra, and W. L. Mattice, "Atomistic Models of Amorphous Polybutadienes .2. Poly(1,4-Trans-Butadiene), Poly(1,2-Butadiene), and a Random Copolymer of 1,4-Trans-Butadiene, 1,4-Cis-Butadiene, and 1,2-Butadiene," *Macromolecules*, vol. 26, pp. 3424-3431, 1993.

[169] W. K. Kim and W. L. Mattice, "A fully atomistic model of an amorphous polybenzoxazine at bulk density," *Computational and Theoretical Polymer Science*, vol. 8, pp. 353-361, 1998.

[170] H. Dong and K. I. Jacob, "Effect of molecular orientation on polymer free volume distribution: An atomistic approach," *Macromolecules*, vol. 36, pp. 8881-8885, 2003.

[171] G. Voronoi, "New parametric applications concerning the theory of quadratic forms - Second announcement," *Journal Fur Die Reine Und Angewandte Mathematik*, vol. 134, pp. 198-287, 1908.

[172] M. Tanemura, T. Ogawa, and N. Ogita, "A New Algorithm for 3-Dimensional Voronoi Tessellation," *Journal of Computational Physics*, vol. 51, pp. 191-207, 1983.

[173] M. Gerstein, J. Tsai, and M. Levitt, "The Volume of Atoms on the Protein Surface - Calculated from Simulation, Using Voronoi Polyhedra," *Journal of Molecular Biology*, vol. 249, pp. 955-966, 1995.

[174] S. Arizzi, P. H. Mott, and U. W. Suter, "Space Available to Small Diffusants in Polymeric Glasses - Analysis of Unoccupied Space and Its Connectivity," *Journal of Polymer Science Part B-Polymer Physics*, vol. 30, pp. 415-426, 1992.

[175] M. D. Shelby and G. L. Wilkes, "The effect of molecular orientation on the physical ageing of amorphous polymers - dilatometric and mechanical creep behaviour," *Polymer*, vol. 39, pp. 6767-6779, 1998.

[176] E. Baer, Y. S. Hu, R. Y. F. Liu, D. A. Schiraldi, and A. Hiltner, "Barrier properties of polyesters - Relationship between diffusion and solid state structure.," *Abstracts of Papers of the American Chemical Society*, vol. 226, pp. U460-U460, 2003.

[177] A. Boersma, D. Cangialosi, and S. J. Picken, "Mobility and solubility of antioxidants and oxygen in glassy polymers. III. Influence of deformation and orientation on oxygen permeability," *Polymer*, vol. 44, pp. 2463-2471, 2003.

[178] M. D. Frogley, Q. Zhao, and H. D. Wagner, "Polarized resonance Raman spectroscopy of single-wall carbon nanotubes within a polymer under strain," *Physical Review B*, vol. 65, pp. 113413, 2002.

[179] Q. Zhao, M. D. Frogley, and H. D. Wagner, "Direction-sensitive stress measurements with carbon nanotube sensors," *Polymers for Advanced Technologies*, vol. 13, pp. 759-764, 2002.

[180] Q. Zhao, R. Tannenbaum, and K. I. Jacob, "Carbon nanotubes as Raman sensors of vulcanization in natural rubber," *Carbon*, vol. 44, pp. 1740-1745, 2006.

[181] C.-C. Hu, K.-R. Lee, R.-C. Ruaan, Y. C. Jean, and J.-Y. Lai, "Gas separation properties in cyclic olefin copolymer membrane studied by positron annihilation, sorption, and gas permeation," *Journal of Membrane Science*, vol. 274, pp. 192-199, 2006.

[182] V. B. Gupta and C. Brahatheeswaran, "Molecular Packing and Free-Volume in Cross-Linked Epoxy Networks," *Polymer*, vol. 32, pp. 1875-1884, 1991.